UNIVERSITY COLLEGE LONDON

Faculty of Mathematics and Physical Sciences

Department of Physics & Astronomy

The early stages of massive star formation: tracing the physical and chemical conditions in hot cores

Thesis submitted for the Degree of Doctor of Philosophy at University College London

by

Hannah Calcutt

Supervisors:

Professor Serena Viti

Professor Michael J. Barlow

Examiners:

Professor Ian D. Howarth

Dr Antonio Chrysostomou

April 7, 2015

Non est ad astra mollis e terris via.

I, Hannah Calcutt, confirm that the work presented in this thesis is my own. Where information has been derived from other sources, I confirm that this has been indicated in the thesis.

Abstract

Molecules are essential to the formation of stars, by allowing radiation to escape the cloud and cooling to occur. Over 180 molecules have been detected in interstellar environments, ranging from comets to interstellar clouds. Their spectra are useful probes of the conditions in which these molecules form. Comparison of rest frequencies to observed frequencies can provide information about the velocity of gas and indicate physical structures. The density, temperature, and excitation conditions of gas can be determined directly from the spectra of molecules. Furthermore, by taking a chemical inventory of a particular object, one can gain an understanding of the chemical processes occurring within a cloud. The class of molecules known as complex molecules (>6 atoms), are of particular interest when probing the conditions in massive starforming environments, as they are observed to trace a more compact region than smaller molecules.

This thesis details the work of my PhD, to explore how complex molecules can be used to trace the physical and chemical conditions in hot cores (HCs), one of the earliest stages of massive star formation. This work combines both the observations and chemical modelling of several different massive star-forming regions. We identify molecular transitions observed in the spectra of these regions, and calculate column densities and rotation temperatures of these molecules (Chapters 2 and 3). In Chapter 4, we chemically model the HCs, and perform a comparison between observational column densities and chemical modelling column densities. In Chapter 5, we look at the abundance ratio of three isomers, acetic acid, glycolaldehyde, and methyl formate, to ascertain whether this ratio can be used as an indicator of HC evolution. Finally, we explore the chemistry of the HC IRAS 17233–3606, to identify emission features in the spectra, and determine column densities and rotation temperatures of the detected molecules.

Acknowledgements

I want to thank my Supervisor, Serena, whose knowledge, wisdom and advice has got me through this PhD. When I thought things had all gone wrong, our meetings contained the solutions I needed.

Also, I wish to thank the members of my group, both past and present, who have always provided help with my work and great company at conferences. In particular, to Paul and Rebeca, whose knowledge saved me on many occasion. I wish to thank my second supervisor, Mike, whose knowledge has taught me how much more I have to learn. Thanks to Alex, whose technical support and advice has really got me through in times of despair. Thanks to Roger, whose skills at fantasy football and feelings towards Hawaii have provided me with hours of entertainment. Thank you to everyone at UCL, particularly those who have always been there for hugs. Thanks to my friends and family who have always been there for me, especially those who fetched everything for me whilst my ankle was broken. Finally, to the reader, hopefully this thesis will be of some interest to you.

Look at the stars,
Look how they shine for you,
And everything you do,
Yeah, they were all yellow.

Yellow, Coldplay

Contents

List of Figures

List of Tables

Chapter 1

Introduction

Long you live and high you fly
And smiles you'll give and tears you'll cry
And all you touch and all you see
Is all your life will ever be.

Breathe, Pink Floyd

The environments in which massive young stellar objects (YSOs) form are observationally complex. Figure 1.1 shows an example of a massive star–forming region. These regions are characterised by dense clouds of gas and dust, with prominent HII regions, where newly formed O and B stars ionize the gas. Within these regions, the earliest stages of massive star formation can be observed. Massive stars form in dense regions which are highly obscured, making the study of their formation difficult (Churchwell et al. 1990; Cesaroni et al. 1991; Plume et al. 1992). High mass stars evolve quickly compared to low mass stars. The core contracts from a low to a very high density (10^7 cm^{-3}), in $\sim 10^4$ – 10^5 yr, reaching the zero–age main sequence while still embedded (Palla & Stahler 1993). These conditions make observationally probing how massive stars form a challenge. However, with the development over the last 50 years of millimetre and sub–millimetre interferometric and single–dish telescopes, it has been possible to probe these environments with the spectra of molecules.

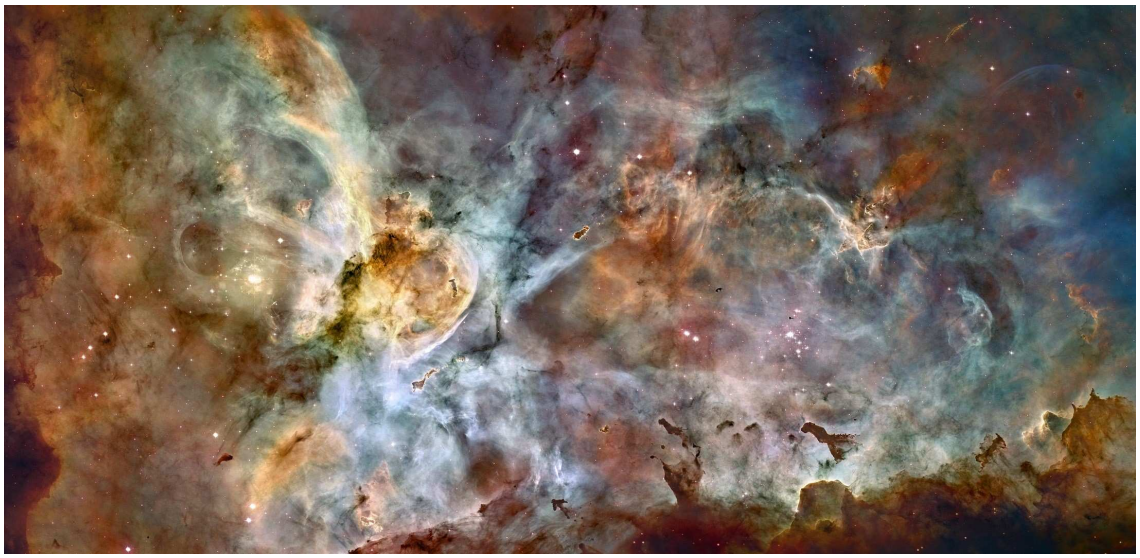

Figure 1.1: An example of a massive star–forming region in the Carina Nebula. Image credit: NASA, ESA, N. Smith (U.C. Berkeley), and the Hubble Heritage Team (STScI/AURA).

Molecules play an important role in star formation, by providing the low opacity required for radiation to escape the cloud and cooling to occur. For example, without the presence of CO the core would heat up, thereby increasing the thermal pressure at an earlier stage, limiting the radius to which the core collapses. This is expected to be important in Population III stars, where owing to the metal free environments in the early universe, H_2 was the main coolant, and stars were more massive and short–lived than present–day stars (Dalgarno & van der Loo 2006).

Over 180 molecules have been detected in astronomical environments, ranging from comets to interstellar clouds. Their spectra are useful probes of the conditions in which these molecules form. Comparison of rest frequencies to observed frequencies can provide information about the velocity of gas and indicate physical structures such as rotating disks and outflows. The density, temperature, and excitation conditions of gas can be determined directly from the spectra of molecules. Furthermore, by taking a chemical inventory of a particular object, one can gain an understanding of the chemical processes occurring within a cloud. By using high spatial resolution observations, one can probe the spatial chemical differentiation within star–forming regions, and by comparing multiple objects at different evolutionary stages, one can gain an insight into the time dependent nature of the chemistry in these regions.

In particular, the detection of complex molecules (>6 atoms) has allowed the conditions closer to where the star is forming to be studied, as complex molecules have been observed to trace a more compact region than simpler molecules (Beltrán et al. 2009). The added complexity of the chemistry required to create such molecules, and their significance in the development of life, means that they are a prominent area of research. Increasingly, complex molecules are being detected in new and diverse environments (Herbst & van Dishoeck 2009), and are seen to trace higher densities and temperatures in massive star formation that have not been traced before. This makes them the ideal molecules to search for in order to probe the most compact regions closest to where the star is forming.

This thesis details the work of my PhD, to explore how complex molecules can be used to trace the earliest stages of massive star formation. The following chapters describe both the observations, and chemical–modelling of several different massive star–forming regions, concluding with the significance this new work brings to the field, and a discussion of the future work that is needed to understand massive star–forming environments.

In particular, the work looks to answer the following questions in relation to complex organic molecules:

- What are the best chemical tracers of the hottest, densest regions, close to where the star is forming?
- Can molecules be used to trace the mass of the final star in a star–forming region?
- What are the best tracers of the evolution of massive star formation?
- How does the chemistry of the local Galactic environment differ from that of Galactic Centre chemistry?

In the following section we discuss the scientific background of massive star formation, and the observational techniques that have been used in this thesis.

1.1 Mechanisms for the formation of massive stars

Determining the specific mechanisms of massive star formation is an area of active research. A full theoretical understanding of the processes involved as well as the observational signatures of these mechanisms is needed. Currently, the most prominent proposed mechanisms are core accretion, and competitive accretion. The core accretion model is an extension of low–mass star formation models (Shu et al. 1987), whereby a massive core fragmented from a large molecular cloud undergoes gravitational collapse. The pre–stellar core mass function has a shape similar to the stellar initial mass function (McKee & Tan 2002, 2003). In competitive accretion, a central massive star is formed when low–mass cores compete to accrete mass from the surrounding molecular cloud (Bonnell 2007). Through this model a significant number of binary systems are formed, which in extreme cases merge to form very high–mass stars. This process has been observed in simulations by Bonnell & Bate (2002), of accretion onto a large stellar cluster.

Both mechanisms predict the presence of accretion disks around massive YSOs, and the presence of molecular outflows (Leurini et al. 2011). The properties of both disks and outflows, however, differ significantly between the two mechanisms:

In competitive accretion, the average accretion rates are much lower than in core accretion, and therefore in order to accrete enough material to form massive stars, they must form in regions of global gravitational collapse with negligible random motions (Tan et al. 2014). Simulations by Wang et al. (2010) explored the effects of protostellar outflows and moderately strong magnetic fields on competitive accretion. They found that the massive stars were fed at high rates by transient dense filaments produced by large–scale turbulent compression at early times in the simulations, with the bulk of mass in the star drawn from the wider clump. The outflows disrupt the accretion process by breaking up the filamentary structures that fed the massive star. This feedback process leads to relatively slow timescales for massive star formation (1 Myr), however, this is heavily dependent on the initial conditions in the clump such as the degree of magnetisation, and the level of turbulence in the clump.

A key result of competitive accretion is that material from the surrounding clump is

funnelled towards the protocluster centre, leading to high gas densities. Observationally this would translate to detections of massive stars in the centre of protoclusters. Observational evidence for this mechanism can also be seen in the size of accretion disks, as simulations indicate that disks would be smaller in competitive accretion compared to those in the core accretion, and exhibit randomly varying orientations. This would also be reflected in the orientation of the protostellar outflows (Tan et al. 2014).

In core accretion it is assumed that the internal pressure is mostly due to turbulence and magnetic fields. Additionally, pressure equilibrium with the surrounding clump is assumed. Collapse occurs in a semi–stable Bonnor–Ebert sphere, with an accretion rate that is initially very large but then falls to the Shu rate of accretion seen in low–mass stars (Shu et al. 1987). The angular momentum of the accretion disk is transferred outwards via disk turbulence and large scale spiral density waves (Tan et al. 2014). Magnetic fields may slow the accretion if a strong stellar B–field is present, but the field strength required would be >kG (Rosen et al. 2012). This magnetic breaking is important in truncating the size of the disk, otherwise the disk may extend to the protostellar surface, which would lead to rotation rates close to values that would disrupt the disk.

A key prediction of core accretion is starless cores, as observed in low–mass star formation. These objects would be <0.1 pc in size and go on to form single stars or small multiple systems. Observations of starless cores have proved elusive, however, Cyganowski et al. (2014) recently reported the detection of a possible massive starless core, G11.92–0.61-MM2. More examples of massive starless core are needed, however, to support the core accretion mechanism.

The rapid evolution of massive stars from low to high densities, reaching the zero–age main sequence while still embedded in their natal clouds, is a problem for any proposed mechanism of massive star formation. They must overcome the limits that radiative feedback place upon mass accretion. Wolfire & Cassinelli (1987) suggested that strong ram pressures produced by a high–mass accretion rate ($\sim 10^{-3}$ $M_{\odot} yr^{-1}$) could be enough to overcome radiation feedback, and produce the most massive stars. This criteria, however, was derived assuming spherical accretion, and if disk–like accretion occurs as is suggested in the competitive and core accretion mechanisms, ram pressures must be even larger in

order to overcome the effects of radiative feedback. Tanaka & Nakamoto (2010) suggest an alternative mechanism for overcoming the radiation pressure, the "OMOSHI" effect. The "OMOSHI" is an acronym for "One Mechanism for Overcoming Stellar High radiation pressure by weIght". It is when the weight of the accumulated accretion flow can overcome the direct radiation pressure from the protostar, and stars can form with steady mass accretion flows with a low accretion rate. Dust particles close to the star sublimate, leading to a dust–free region, with very small gas opacity. This prevents the efficient absorption of stellar radiation by the accreting gas, resulting in the large outward momentum of the radiation being transferred to the accretion flow, and mass accretion being disrupted. If the accretion rates are not high enough to overcome this (i.e. a high ram pressure), this problem can be overcome if the surface density of the flow is sufficient. This effect dramatically reduces the requirement for high accretion rates in order to form massive stars. Further details and a derivation of the condition required to overcome radiation pressure are beyond the scope of this thesis, but can be found in Tanaka & Nakamoto (2010) .

Currently, there is no enough observational evidence to clearly support any of these mechanisms. Determining accretion disk sizes and accretion rates, however, will clearly distinguish between them. High resolution observations are needed of molecules that trace only the most compact regions surrounding the forming protostar, if accretion disks are to be detected.

1.2 The earliest stages of massive star formation

The earliest stages of massive star formation can be split into three distinct phases, the cold core phase, the warm–up phase, and the hot core phase. Observationally we detect the cold core phase by observations of infrared dark clouds (IRDCs) (Figure 1.2). These cold (10 K) and dense (10^4 – 10^5 cm^{-3}) objects are seen as extinction features against the bright mid–infrared Galactic background. They may contain numerous cold cores at different stages of collapse. Within these objects hydrogen is mostly bound as H_2, and gas phase species accrete onto the dust grains, where a surface chemistry can proceed and ices can form (Hasegawa et al. 1992; Pickles & Williams 1977; Ruffle & Herbst 2001; Tielens & Hagen 1982). These 'icy grain mantles' are key for the formation of both H_2

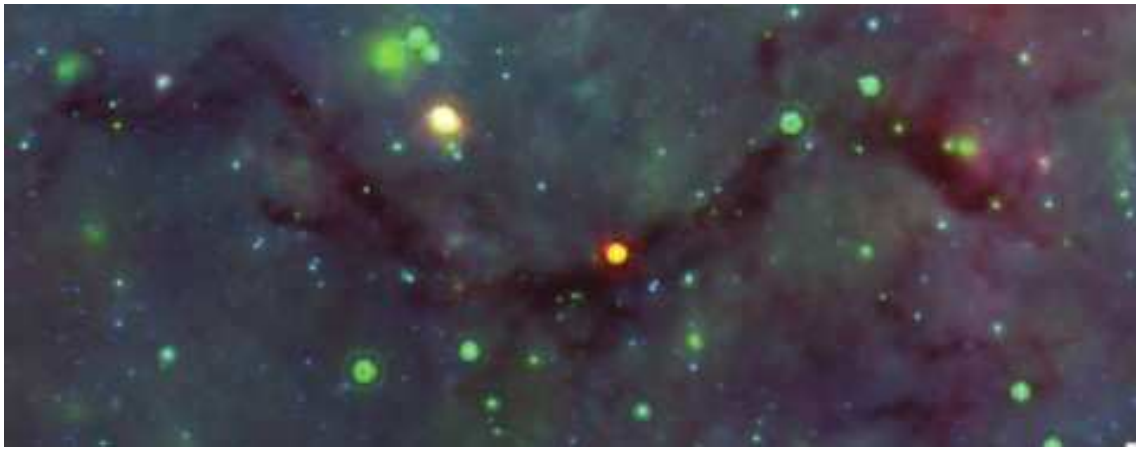

Figure 1.2: The IRDC G11.11–0.11, taken from Carey et al. (2009). This is a three colour composite (8, 24, and 70 μm) from the MIPSGAL survey.

(Hollenbach & Salpeter 1970, 1971; Hollenbach et al. 1971) and most complex molecules, as they provide a catalytic surface, where molecules formed in the gas phase can 'stick' to and undergo surface reactions .

As the forming protostar heats up the gas and dust, the cores enter the warm–up phase. At this stage molecules on the surface of the grains begin to sublimate back in to the gas phase. When the temperatures reach $100-300$ K all grain–surface species sublimate (Herbst & van Dishoeck 2009), and gas–phase chemistry dominates the production and destruction of molecules. This stage is known as the hot core phase. Hot cores, or as they are often known hot molecular cores (HMCs), are typically much larger than their low–mass analogues (~ 0.18 pc). A rich chemistry is observed in these objects, where the most complex molecules are detected. Figure 1.3 shows the spectra of the Orion nebula hot core, taken with the HIFI instrument on the Herschel space observatory (ESO, HEXOS and the HIFI consortium, E. Bergin). This Figure highlights the crowded spectra that can be seen in hot cores in a small frequency range. This high spectral density can make identifying molecules a difficult task.

1.3 Molecular tracers

It is important to determine the best tracers of the different stages of massive star formation, in order to best map the physical and chemical conditions found around forming

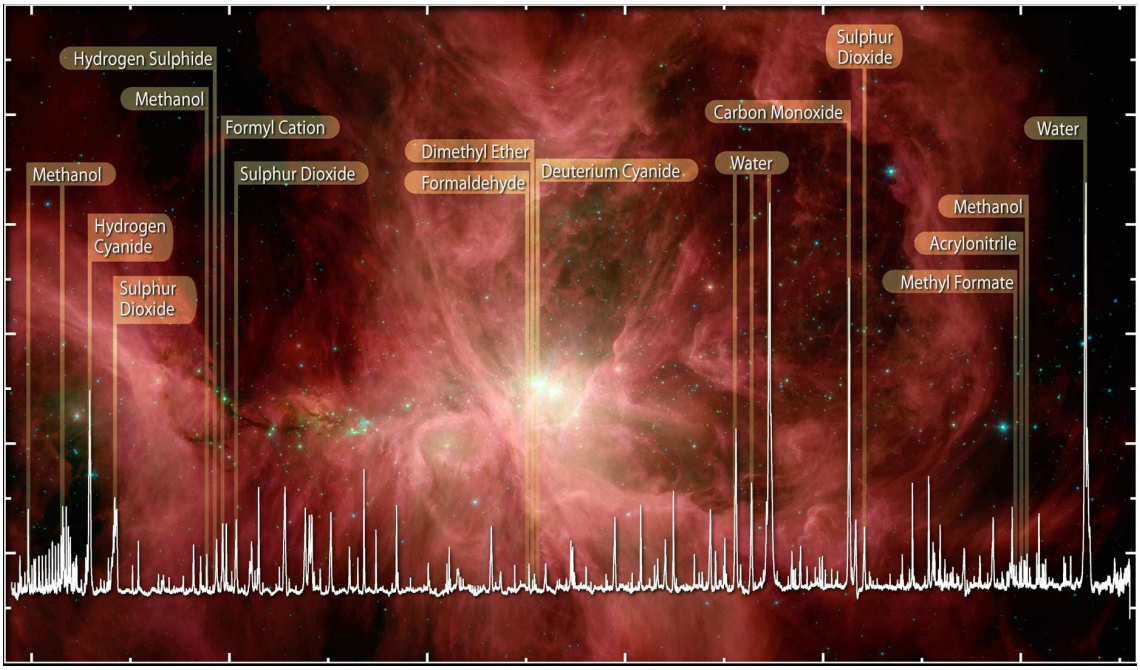

Figure 1.3: An example spectra of the Orion nebula hot core, taken with the HIFI instrument on the Herschel space observatory in the frequency range 520 – 635 GHz. Image credit: ESO, HEXOS and the HIFI consortium, E. Bergin.

stars. One of the most common tracers of interstellar gas is CO. CO and its isotopologues are easily excited at 10 K, making transitions such as CO (1 – 0) excellent tracers of IRDCs. As well as tracing gas, CO also traces the fraction of species that are frozen on to the grain–surface, otherwise known as the depletion factor. Within the cloud, the different density structures that arise during the star formation process can be traced by observations of HCO^+ (1 – 0) and N_2H^+ (1 – 0) (Zhu et al. 2007), which also provide constraints on the cosmic ray ionisation rate (Williams & Viti 2013). The ratio of N_2H^+ to HCO^+ can be used as an indicator of CO depletion, as the abundance of N_2H^+ increases with CO freeze–out. The line profiles of HCO^+ (3 – 2) and CS (2 – 1) (Lehtinen 1997) can be used to search for the signatures of gravitational collapse. The profiles of HCN transitions can also be used to indicate gravitational collapse in a cloud. These infall motions are determined through the observation of P–Cygni profiles. They result from optically thick emission in a collapsing cloud, where the gas moving towards the observer on the far side of the cloud is blue–shifted, and the gas on the near side of the cloud is red shifted resulting in self absorption in the line profile. To confirm an infall signature is present observations of an optically thin transition are also needed, to ensure there aren't multiple velocity components present (Tan et al. 2014).

As star formation proceeds in the cloud, and the protostar 'switches on', typical signposts of massive star formation, such as jets, shocks, outflows, and masers are observed. SiO is an excellent tracer of the shocks inside jets, and suffers minimal contamination from infalling envelopes, tracing regions close to the protostar (Codella et al. 2013). Detection of high–velocity wings on the line profiles of CO and H_2S transitions are characteristic of molecular outflows (Gibb et al. 2004). Masers are often seen in CH_3OH, H_2O, and OH, and CH_3OH masers with weak radio continuum flux have been found to be associated with massive ($\sim$50 $M_\odot$), luminous ($\sim10^4$ $L_\odot$), and deeply embedded cores, in protoclusters of young massive protostars (Minier et al. 2005).

The best molecular tracers of compact structures within hot cores are not clear. Ideally, they should be optically thin, and trace only the hot gas around the central protostar and not its envelope (Leurini et al. 2011). A variety of complex molecules have been suggested as the best tracers of these regions, and as the most suitable molecules to detect accretion disks around forming massive stars. Evidence of rotating structures have been observed by several authors (e.g. Cesaroni 2002; Beltrán et al. 2005), and observations have focused on the CH_3CN and $CH_3{}^{13}CN$ (12 – 11) K ladder. CH_3CN transitions have a wide range of upper energy levels from 69 – 1605 K, and it is also a low abundance molecule which is excited in very dense regions, making it an excellent tracer of disks (Beltrán et al. 2005). It has been found to trace compact regions in hot cores, but increasingly other complex molecules have been found to trace more compact regions, closer to where the star is forming (Beltrán et al. 2009).

To date, more than 50 complex molecules have been detected in space. Table 1.1 lists the hydrocarbons, N–containing species, O–containing species, and S containing species that have been detected in star–forming environments, as well as the locations in which they have been found (based on the table in Herbst & van Dishoeck 2009). These detections have provided an insight into the complex chemistry that can occur around forming stars, and have led to the study of the wide range of chemical processes needed to form these molecules. In particular, the observed abundances of many of these species was found to be much higher than expected from pure gas phase reactions alone, indicating additional mechanisms of formation.

Table 1.1: Complex molecules that have been detected in star–forming environments, including the location that they have been detected in. 'cc' stands for cold core, 'hc' stands for hot core/corino, 'lc' stands for lukewarm corino, 'gc' stands for Galactic Centre cloud, 'circ' stands for circumstellar envelope around evolved a star/protoplanetary nebula, and 'of' stands for outflow. This table is based on the table in Herbst & van Dishoeck (2009).

Species	Name	Source	Species	Name	Source
Hydrocarbons			**N–Containing**		
C2H4	Ethene	circ	CH3CN	Methyl cyanide	cc, hc, of
HC4H	Butadiyne	circ	CH3NC	Methyl isocyanide	hc
H2C4	Butatrienylidene	circ, cc, lc	CH2CNH	Keteneimine	hc
C5H	Pentadiynyl	circ, cc	HC3NH+	Prot. cyanoacetylene	cc
CH3C2H	Propyne	cc, lc	C5N	Cyanobutadiynyl	circ, cc
C6H	Hexatriynyl	circ, cc, lc	HC4N	Cyanopropynylidene	circ
C6H–	Hexatriynyl ion	circ, cc, lc	CH3NH2	Methylamine	hc, gc
H_2C_6	Hexapentaenylidene	circ, cc, lc	C_2H_3CN	Vinyl cyanide	cc, hc
HC_6H	Triacetylene	circ	HC_5N	Cyanodiacetylene	circ, cc
C_7H	Heptatriynyl	circ, cc	CH_3C_3N	Methylcyanoacetylene	cc
CH_3C_4H	Methyl diacetylene	cc	CH_2CCHCN	Cyanoallene	cc
CH_3CHCH_2	Propylene	cc	NH_2CH_2CN	Aminoacetonitrile	hc
C_8H	Octatetraynyl	circ, cc	HC_7N	Cyanotriacetylene	circ, cc
C8H–	Octatetraynyl ion	circ, cc	C_2H_5CN	Ethyl cyanide	hc
CH_3C_6H	Methyltriacetylene	cc	CH_3C_5N	Methyl cyanodiacetylene	cc
C_6H_6	Benzene	circ	HC_9N	Cyanotetraacetylene	circ, cc
O–Containing			C_3H_7CN	N–propyl cyanide	hc
CH_3OH	Methanol	cc, hc, gc, of	$HC^{11}N$	Cyanopentaacetylene	circ, cc
HC_2CHO	Propynal	hc, gc			
CH_3CHO	Acetaldehyde	cc, hc, gc			
c–CH_2OCH_2	Ethylene oxide	hc, gc			
CH_3COOH	Acetic acid	hc, gc			
C_2H_3CHO	Propenal	hc, gc			
CH_3OCH_3	Methyl ether	hc, gc			
$HOCH_2CH_2OH$	Ethylene glycol	hc, gc			
$HCOOC_2H_5$	Ethyl formate	hc	**S–Containing**		
c–C_3H_2O	Cyclopropenone	gc	CH_3SH	Methyl mercaptan	hc
C_2H_3OH	Vinyl alcohol	hc	**N and O–Containing**		
$HCOOCH_3$	Methyl formate	hc, gc, of	NH_2CHO	Formamide	hc
$CH_2(OH)CHO$	Glycolaldehyde	hc, gc	CH_3CONH_2	Acetamide	hc, gc
C_2H_5OH	Ethanol	hc, of			
C_2H_5CHO	Propanal	hc, gc			
CH_3COCH_3	Acetone	hc			

1.4 Chemical processes

1.4.1 Gas–phase chemistry

In the low temperatures of IRDCs, the dominant chemistry that occurs is through exothermic reactions which have no activation energy (Herbst & van Dishoeck 2009). Ion–neutral reactions are common as they obey this constraint (Herbst & Klemperer 1973; Watson 1973), however, some exothermic neutral–neutral reactions do occur. The high opacities ($\tau \sim 5$) seen in IRDCs means that UV photons from surrounding protostars can not penetrate the cloud. Cosmic rays, however, have significant energy to penetrate the cloud, and have an important influence on the chemistry by forming many ions. The secondary

electrons from this process then cause a significant fraction of the ionisation in the cloud (Cravens & Dalgarno 1978). Cosmic rays also lead to a non–negligible UV flux inside the cloud from the excitation of H_2 by secondary electrons, which then reradiate back to the ground state (Gredel et al. 1989; Prasad & Tarafdar 1983).

1.4.2 Grain–surface chemistry

Molecules accrete on to the surface of dust grains via either van der Waals forces (physisorption) or by chemical valence forces (chemisorption) (Watson & Salpeter 1972). Due to the potential barrier in chemisorption accretion, most molecules accrete on to the dust grains through physisorption in IRDCs. The grain–surface acts as a catalytic surface, allowing a more complex chemistry to arise in the cloud. There are three main mechanisms for surface reactions which are illustrated in Figure 1.4:

The Langmuir–Hinshelwood mechanism: Molecules are formed on the surface of the grain when one species diffuses to the binding site of another species, by tunnelling or thermal hopping over the energy barrier E_b between binding sites. Once reactants are in the same energy minima they can react forming a new species.

The Eley–Rideal mechanism: When a gas phase species lands on to another grain–surface species they can react and form a new species.

The hot atom mechanism: A gas phase species has sufficient energy to land on the grain–surface, and collide with a grain–surface species before thermalisation.

These mechanisms have been found to be the most significant formation routes for many complex molecules (e.g. $CH_2(OH)CHO$, $HCOOCH_3$; Woods et al. 2012; Occhiogrosso et al. 2011.

An important factor in determining grain–surface formation and destruction pathways, as well as reaction rates for any species, is the modelling of the icy grain mantles in laboratory conditions. Laboratory studies typically model the dust surface in a high pressure vacuum ($10^{-10} - 10^{-11}$ mbar), at low temperatures ($12 - 15$ K), using a mass spectrometer to determine the species formed on the grain–surface. An example of such

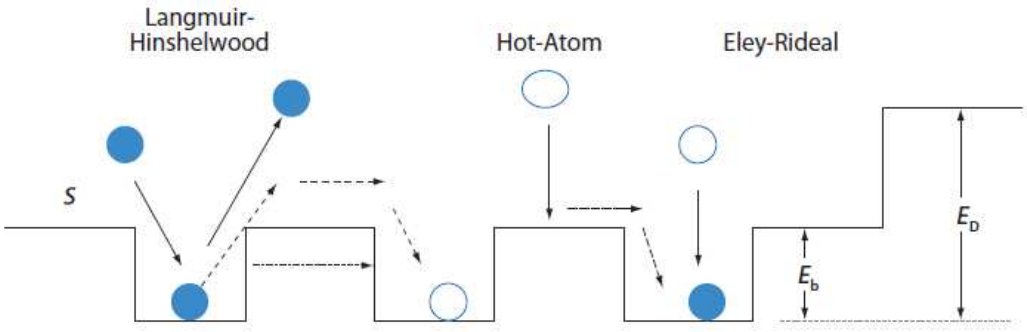

Figure 1.4: The Langmuir–Hinshelwood, hot atom, and Eley–Rideal mechanisms for grain–surface reactions, where S is the sticking coefficient, E_D is the desorption energy for a species, and E_b is the energy barrier for a species to 'jump' to another location on the grain–surface. Image taken from Herbst & van Dishoeck (2009).

experiments, of significance to this thesis, is the sublimation and irradiation studies of the molecule glycolaldehyde by Burke et al. (2012). This work helps to determine the reaction rates for the formation and destruction of glycolaldehyde, as well as the kinetic parameters for the desorption of the species. These physical parameters are needed in order to accurately model the chemistry observed in massive star–forming regions.

1.5 Molecular spectroscopy

In order to determine the physical and chemical conditions within hot cores, it is essential to be able to detect the large number of energy level transitions available in molecular emission. In addition to the electronic states seen in atoms, each electronic state of a molecule will have additional transitions associated with it, due to the degrees of freedom associated with the vibration and the rotation of the molecule. Each electronic state has a ladder of vibrational transitions, which each have a ladder of rotational transitions. Transitions between rotational and vibrational states are called ro–vibrational transitions, and can be detected in the infrared. Pure rotational transitions between rotational states of the same vibrational level occur in the far–infrared, millimetre and sub–millimetre range. Most molecules are detected through their rotational transitions, meaning that it is essential that reliable laboratory rotational spectra are obtained of molecules wishing to be detected in interstellar environments. Microwave spectroscopists have been studying the rotational spectra of large numbers of molecules since the 1930s (Townes & Schawlow 1955). Initially, most studies focused on frequency ranges from $1-40$ GHz, but eventu-

ally studies moved on to the millimetre (30 – 300 GHz), and sub–millimetre range (300 – 1000 GHz) (Herbst & van Dishoeck 2009), with select groups now working beyond 1 THz (Xu et al. 2008). These experiments typically involve irradiating a solid–state source of molecules, and then recording the millimetre and sub–millimetre spectrum using a spectrometer (Haykal et al. 2012). These methods can achieve an experimental error of < 1 kHz on the rest frequencies of molecular transitions.

1.5.1 Observational techniques

In order to investigate the chemistry of star–forming regions, one must be able to observe the spectra of molecules. A detailed discussion on how to identify molecules in space from these spectra can be found in Chapter 2; here we discuss the observing techniques used to find them.

1.5.2 Single–dish observations vs interferometric observations

The increasing capability of both single–dish and interferometric telescopes has led to the detection of a growing complexity of molecules in star–forming regions. Depending on the nature of what is to be observed, either a single–dish telescope or an interferometer may be best suited to carry out the observations.

A single–dish telescope consists of a single antenna, and can range in size from ∼1 m diameter dishes up to the 305 m Arecibo observatory, however, for steerable dishes the largest practical size a dish can be is 100 m. An astronomical interferometer is an array of antennas which can be used to have a larger collecting area than any one antenna within the array. An example of a single–dish telescope, the James Clerk Maxwell Telescope (JCMT), can be found in Figures 1.5 and 1.6. The JCMT is a 15 m single–dish telescope, located near the summit of Mauna Kea in Hawaii. It is an important facility for studies of star–forming regions, as it is the largest astronomical telescope in the world designed specifically to operate in the sub–millimetre wavelength range[1]. An example of an interferometer, the Plateau de Bure Interferometer (PdBI), can be found in Figure 1.7. The PdBI is a six–antenna interferometer located in the French Alps, on the Plateau de Bure at 2550 m. Each antenna has a diameter of 15 m, and the interferometer can operate in the 3, 2, 1.8

[1] http://www.jach.hawaii.edu/JCMT/

Figure 1.5: The outside of the JCMT single–dish telescope. Image credit: Joint Astronomy Centre.

and 0.8 millimetre bands[2].

Advantages of single–dish telescopes

It can be more advantageous to use a single–dish telescope if the observations require a high sensitivity. The sensitivity of a telescope is dependent on the collecting area of each antenna, so a large single–dish telescope will have a better sensitivity than an array of smaller antenna, despite the array having an overall larger collecting area. Some specialised instrumentation is also only available on single–dish telescopes, as it would be

[2]http://www.iram.fr/IRAMFR/

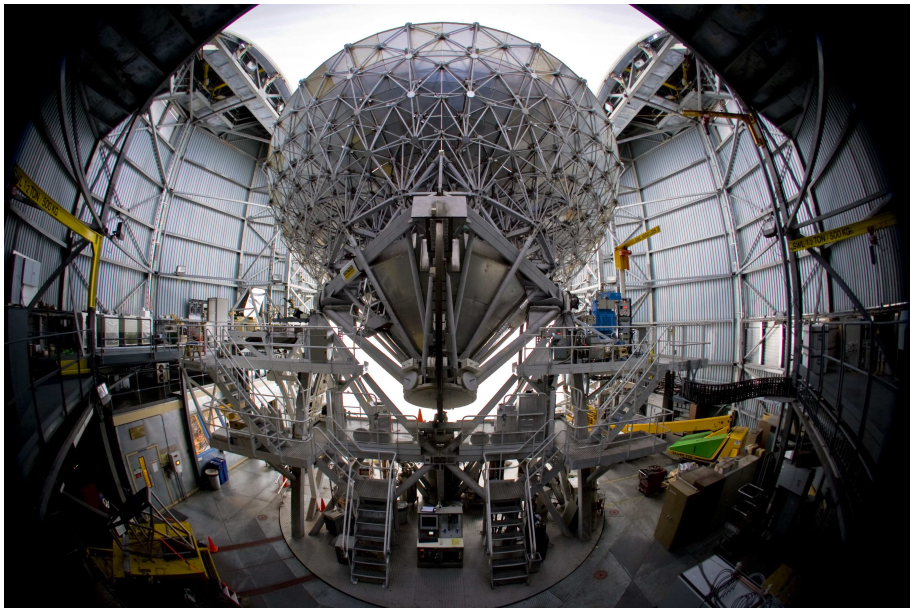

Figure 1.6: The back of the antenna at the JCMT. Image credit: Joint Astronomy Centre

Figure 1.7: The Plateau de Bure Interferometer. Image credit: IRAM

too expensive to put this equipment on every dish in an array (Wright 2004). Another advantage is that there are more single–dish telescopes available to observers in the world. This means that competition for time on interferometers is greater than on single–dish telescopes. Single–dish telescopes are also very good at mapping emission in very extended objects, and large areas of the sky; however, if the size of the source is smaller than the beam size of the telescope, weak signals can be lost due to beam dilution.

Advantages of interferometers

Interferometers can offer some advantages over single–dish telescopes. By using an array of antennas, an interferometer can have a large collecting area for a smaller cost than the equivalent collecting area of a single–dish telescope. This is of particular significance when requiring high spatial resolution observations, as is needed for sources with detailed structures. Instantaneous imaging is also possible with interferometers, by performing a fourier transform of the visibilities (Andernach 1999). The main disadvantage of using an interferometer, is that for structures which would be measured by antenna separations smaller than the shortest antenna separation on the interferometer, information is lost, i.e. the largest spatial scales. This problem is often referred to as 'missing flux'.

The problems associated with both single–dish and interferometric observations are often overcome by combining the techniques to observe the same source. Detection studies in massive star–forming regions can be performed with single–dish facilities, and then followed up with detailed mapping using interferometric facilities.

1.5.3 Heterodyne detectors

The commonest detectors used in both single–dish and interferometric observations are heterodyne detectors. Here we briefly describe how they work and allow spectral lines to be detected.

When a radio signal from an astronomical source impinges on an antenna, it causes a fluctuating voltage which varies at the same frequency as the source radiation, namely the radio frequency (RF). This voltage is first amplified by the front end of the detector and then passed on to the mixer. Front ends are typically cooled with liquid helium, to ensure as little noise as possible is passed onto the astronomical signal. At the mixer,

the incoming signal is mixed with a local oscillator (LO), to create the intermediate frequency (IF). This process is known as heterodyning. This process is the most economical way to handle the wide range of radio frequencies that most radio telescopes operate at, by converting all incoming radio frequencies to a standard IF, so one can use the same back–end equipment for all radio frequencies (Chengalur 2003). This method also has the added bonus of allowing an IF frequency to be chosen that can minimise transmission loss across long distances. After the signal is converted to the IF, it is amplified again and then mixed to the base band frequency range before being sent to the backend. For spectral line observations, the signal is then passed on to a spectrometer.

There are several observing techniques that are important when using heterodyne receivers and which are important for the work in this thesis. We outline them in the following sections.

1.5.4 Observing techniques with heterodyne detectors

With all ground–based observations, noise from local sources and the atmosphere has to be accounted for. Here we discuss two of the techniques used to reduce the effects of noise in molecular spectra.

Position–switching

When using this technique, the telescope observes the source and a position away from the source free from emission at the main frequency, thereby obtaining a spectrum containing only instrumentation and atmospheric effects. This effect can then be removed from the source spectra. One must complete a position switch within the timescale that the conditions change, which is typically 30 seconds or less (Matthews et al. 2004).

Beam–switching

In this technique, the secondary mirror is chopped with the source in one beam. Typically every 10 – 30 seconds, the telescope nods between the beam switched positions, to bring the source into the other beam (Matthews et al. 2004). A negative beam is then obtained when the source is in the reference beam, and a positive one when it is in the signal beam. There is a limitation with this method to how far from the source position the beam can be chopped, typically $180''$, at the JCMT. This technique is therefore best used for sources

with small angular size.

1.6 Chemical–modelling

Observations of star–forming regions only allow a snapshot of the chemistry to be taken. In order to probe the chemistry as a function of key physical parameters, it is necessary to develop models which can simulate the entire star–forming process. Chemical models compute the evolution of chemical abundances as a function of key physical parameters such as time, temperature or depth. Chemical models solve a set of ordinary differential equations of the order:

$$\frac{dn_i}{dt} = \sum production - \sum destruction \tag{1.1}$$

where n_i is the number density of species i. The production and destruction terms refer to all chemical and physical processes that produce and destroy atomic and molecular species (Wakelam et al. 2013).

Most models assume an initial atomic gas composition, with abundances of carbon, oxygen, helium, nitrogen, and sulphur, set to solar elemental abundances or set to scale with solar metallicity. However, observed ratios of C/O can vary significantly, and N production is thought to be suppressed at early cosmological epochs (Williams & Viti 2013), therefore a value better suited to the local environment may be required. For some chemical models the initial elemental abundances are considered uncertain, and are therefore taken as a free parameter.

At least four types of chemical models exist and are best suited to different astronomical regions (e.g. see van Dishoeck & Blake 1998; Williams & Viti 2013):

- Steady–state, single–point chemical models which are typically used to predict equilibrium abundances in homogeneous media. Typically the gas number density is fixed in this type of modelling.

- Steady–state, depth–dependent models, which are used to determine abundances in photon–dominated regions. Initial and final gas densities are set and then functions for how the density evolves with space are included in the model. Typically the

thermal balance is computed self–consistently by solving the level populations for the main coolants whose abundances are determined in the model.

- Time–dependent, single–point models, which are used to model how the chemistry of dense regions changes with time. This type of modelling is important to understand the evolution of massive star formation, as the temperature and density conditions change significantly from infrared dark clouds to hot cores. Typically, an initial gas density and a final gas density are set, and then functions for how the density evolves with time are included in the model.

- Time–dependent, depth–dependent models allow the chemistry to be modelled as a function of space and time. With the increasing spatial resolution of interferometric telescopes, these types of models are important to understand the spatial distribution of molecules already observed in many objects. The larger computing power available to modern–day chemical models means that a large number of chemical reactions can be modelled at multiple time steps, and multiple spatial points. As with time–dependent models initial gas densities and final gas densities are set, and then functions for how the density evolves with time and space are included in the model.

For every type of model discussed above, gas and dust temperatures must be considered. Depending on the astronomical regions, it may be necessary to compute the change in gas and dust temperature as a function of both time and space. Cosmic–ray ionisation rates must also be considered to accurately model the chemistry. For most models a cosmic ray ionisation rate for hydrogen of typical Milky Way values is sufficient ($\sim 10^{-17}$ s^{-1}), however, in some regions such as the Galactic Centre, a higher value must be adopted.

1.7 Gas–phase and grain–surface reactions

As discussed in Section 1.4, a large variety of chemical reactions and processes occur in astronomical environments. For some species, such as H_2, grain–surface formation routes are essential in order to account for observed abundances. For other species, dominant formation and destruction routes may only occur in the gas–phase. Large chemical networks are used to model a large number of species, and reaction types in chemical–modelling codes. Typically, chemical model reaction networks consist of either gas–phase reactions only or

both gas–phase and grain–surface reactions. The main databases of gas–phase reactions are UMIST[3], KIDA[4] and the Ohio State University database[5], which contain formation and destruction routes, as well as rates of reaction for a large number of species, and contain both experimental and theoretical reactions. For gas–grain reactions some species have been studied in ISM conditions in laboratories and rates of reactions determined. There are also reactions which have been determined theoretically, either through quantum calculations, or by 'constructing' reactions based on similar reactions involving an isomer of a species. For both gas–phase and grain–surface reactions, which have not been studied in ISM conditions, their reaction rates can be considered to be quite uncertain. These uncertainties, combined with the uncertainties in formation and destruction routes for certain species, means that the abundances determined through chemical–modelling can, for some species, be inaccurate. In these circumstances a sensitivity study is often undertaken, to explore the propagation of errors through the modelling process, and to determine the significance on the abundance of the species. This approach can also be used to test which of the formation and destruction routes are most efficient for a species.

1.7.1 Freeze-out

There are several different approaches to treating the chemistry of both gas–phase and grain–surface reactions in chemical–modelling codes. Different methods may be adopted to determine the rate of reactions within the code.

One method is the rate equation approach which assumes averaged number densities and a large volume of gas. The rate per unit volume at which species 'freeze-out' onto the grain–surface can be approximated by:

$$\frac{dn(i)}{dt} \propto d_g a^2 n_H S_i T^{1/2} m_i^{1/2}, \tag{1.2}$$

where d_g is the ratio of the number densities of grains to H nuclei, a is the grain radius, T is the temperature of the dust, m_i is the mass of species i, n_i is the number density of species i, and S_i is the sticking coefficient. S_i is often considered to be a free parameter but

[3] www.udfa.net
[4] http://kida.obs.u-bordeaux1.fr
[5] http://www.physics.ohio.state.edu/∼eric/research.htm

for weakly bound species, such as CO, experiments indicate that it is close to 1 (Williams & Viti 2013).

Several codes also include the effects of thermal and non-thermal desorption induced by H_2 formation, cosmic rays and photons.

Alternative techniques to the treatment of both gas–phase and grain–surface chemistry include the master equation method (Biham et al. 2001; Green et al. 2001; Stantcheva et al. 2002) and macroscopic Monte Carlo simulations (Charnley 1998, 2001; Stantcheva et al. 2002). For the purposes of the chemical–modelling in this thesis, however, we use the rate equation approach, as detailed by Rawlings et al. (1992).

1.8 Outline of thesis

In this thesis, we use a combination of observations and chemical–modelling to investigate the physical and chemical properties in the hot core phase of massive–star formation. In Chapter 2, we look at the process of molecular line identification, and determine the identity of several previously unknown lines in the spectra of six different hot cores. In Chapter 3, we determine the column densities of the molecular content of these cores, to provide a quantitive analysis and comparison of the complex chemistry that is occurring. We chemically model these hot cores in Chapter 4, and perform a comparison between modelling column densities and the observational column densities determined in Chapter 3. In Chapter 5, we look at the abundance ratios of acetic acid, and its isomers glycolaldehyde and methyl formate. This work follows on from several of the detections in Chapter 2, with new observations to compare the chemistry of hot cores outside the Galactic Centre, to those in the Galactic Centre. In Chapter 6, we use observations and spectral–modelling to explore the chemistry of the hot core in IRAS 17233–3606. Finally, in Chapter 7 we present the conclusions drawn from this body of work, and the future steps needed to advance this research.

This page was intentionally left almost blank.

Chapter 2

A Chemical Inventory of Hot Cores

Space is big. You just won't believe how vastly, hugely, mind-bogglingly big it is. I mean, you may think it's a long way down the road to the chemist's, but that's just peanuts to space.

Douglas Adams, The Hitchhiker's Guide to the Galaxy

The work presented in this Chapter and Chapters 3 and 4 is based on the paper by Calcutt et al. (2014) in collaboration with S. Viti, C. Codella, M. T. Beltrán, F. Fontani, and P. M. Woods.

2.1 Identifying spectral lines

To really understand the earliest stages of massive star formation, one must compare the physical and chemical environments in a number of hot cores. Ideally a chemical inventory should be taken in order to qualitatively characterise each core and its evolutionary stage. Essential to this task is the ability to accurately identify the lines present in the spectra. Massive star forming regions are, however, complex regions, making line identification

difficult in the spectra of hot cores. High spectral line densities can easily lead to line contamination and confusion becoming a serious problem when confirming the presence of new molecules. The identification of spectral features is also limited by the transitional information available in spectroscopic line databases, where many lines remain unidentified. There are seven main spectroscopic line databases: The JPL catalog is a catalogue of submillimetre, millimetre, and microwave spectral lines in the frequency range of 0 – 10,000 GHz (Pickett et al. 1998). It contains spectral information on 331 atomic and molecular species and includes a total of 1,845,866 transitions. The Cologne Database for Molecular Spectroscopy (CDMS) is a catalogue of radio, microwave, and far-infrared spectral lines of atomic and molecular species that may occur in the interstellar or circumstellar medium or in planetary atmospheres (Müller et al. 2005), it includes 111 species. The Lovas/NIST database is a list of millimetre and microwave transitions compiled from laboratory spectral data obtained from the literature (Lovas 2004). The Toyama Microwave Atlas for spectroscopists and astronomers (ToyaMA) is a database of microwave spectroscopy of molecules with internal rotors. The TopModel database is a list of spectroscopic information for the ^{13}C isotopologue of methyl formate ($HCOOCH_3$). SLAIM is the spectral line atlas of interstellar molecules which is only available through the Splatalogue database for astronomical spectroscopy (www.splatalogue.net). Splatalogue also contains spectral information for the ∼3000 strongest lines of ethyl cyanide (C_2H_5CN) from the Ohio State University (OSU) (Medvedev & De Lucia 2007; Fortman et al. 2010). The Splatalogue database combines all of the above databases into an open access platform, with a query form allowing the selection of all transitions from a particular species, or a subset of transitions based on a user specified frequency range. Currently, Splatalogue contains over 5.8 million transitions and 1038 species. It is worth noting, however, that the most up to date versions of both the JPL and CDMS catalogues can only be found on their respective websites (http://spec.jpl.nasa.gov and http://www.astro.uni-koeln.de/cdms/catalog). The spectral information listed in each of these databases includes the species name, frequency, frequency error, intensity, energy level, upper state degeneracy, and quantum number assignment for each transition.

In order to confirm the presence of a new molecule in space, a rigorous method must be applied to ensure the correct line assignment is made. At least three transitions of a molecule must be identified in the same object in order to confirm its presence, although

ideally more transitions should be detected to ensure a correct identification and accurate determination of column densities and excitation temperatures.

The following criteria, taken from Snyder et al. (2005), demonstrate the steps necessary to ensure the correct identification of a spectral line:

1. Rest frequencies of the candidate spectral line must be accurate. Ideally they should be measured directly in a laboratory, however, if direct measurements are unavailable, interpolation fitting of laboratory data from other frequencies can be used to create a Hamiltonian model. This can then be used to predict frequencies with uncertainties <0.0001 GHz.

2. Transitions with upper energy levels exceeding the highest upper energy level of a transition previously detected in the object, can be excluded from candidate line lists.

3. All the expected transitions of a molecule must have frequency agreement. The rest frequency of the assigned transitions must be in reasonable agreement (within the frequency error) with the frequency corresponding to the LSR velocity of the source. Variations in the LSR velocity of a molecular species may be seen in regions where a range of kinematics contribute to the emission or absorption spectrum. Regions with no large kinematic variation should have a well defined velocity field. If there is a source velocity gradient observed in the transitions of known molecules, it will not be a random function of transition frequency or energy level.

4. In the case of line blending two lines should at least be resolved by the Rayleigh criterion, to ensure the correct line identification. The Rayleigh criterion states that the minimum distance between two spectral lines in frequency space must be such that the maximum intensity of one line falls on the first null of the other. This can be approximated by requiring that blended lines are separated by their frequency width half maximum (FWHM) intensity (assuming identical line profiles). Snyder et al. (2005) also remark that a more stringent criterion may be used, whereby two overlapping lines can be considered to be resolved if they are at least separated at the half-maximum intensity of the weakest line.

5. If other transitions from the same molecule are present in the observed frequency range, have line strengths at detectable levels, and there are no mitigating circum-

stances such as maser activity or line self-absorption as to why they should not be observed, they should be present in the spectra. Their relative intensity must also correspond to the predicted one under LTE.

6. Transitions from molecules already observed in similar objects and, if not, in the interstellar medium (ISM), should be favoured over new molecules not yet detected in space.

In order to build up a complete picture of the chemistry in the massive star formation environment, it is essential to correctly identify all of the emission observed in hot cores, at different evolutionary stages. Only then can a comparison of how the chemistry evolves around forming massive stars be complete. The following chapter details the results of an identification study in six star forming regions and a chemical comparison between the cores.

2.2 Observations

This work is based on observations taken with the PdBI and reported by Beltrán et al. (2005), for the hot cores G31.41+0.31 (G31) and A1 and A2 in G24.78+0.08 (G24A1 and G24A2), and by Beltrán et al. (2011) for the hot cores G29.96–0.02 (G29), G19.61–0.23 (G19), and G10.62–0.38 (G10). Details of the phase centre used for each source can be found in Table 2.1.
The PdBI offers four antenna configurations which can be combined to produce maps with different angular resolution (Winters & Neri 2011). The A configuration is the most extended configuration and is therefore well suited to mapping compact, strong sources. The B configuration is the second most compact configuration and is well suited for strong sources. The C configuration provides a fairly complete coverage of the uv-plane and can be combined with the D configuration to be used for low angular resolution studies. The D configuration is the most compact and provides the lowest phase noise and the highest sensitivity.

For G31 and G24 the observations were carried out on the 16th March 2003 in the most extended (A) configuration. The correlator was centred at 220.520 GHz in the upper

sideband at 1.4 mm. The bandpass of the receivers was calibrated by observations of the quasar 3C 273. Amplitude and phase calibrations were achieved by monitoring quasar (PKS)1741–038, whose flux density of 2.99 Jy at 1.4 mm was determined relative to MWC 349. Interferometric observations of G29, G19 and G10 were carried out on 28th February and 16th March 2004, and on the 26th February and the 21st March 2005. G29 was observed in the most extended (A) and compact (C) configurations, while cores G19 and G10 were observed in the extended (B) and compact (C) ones. Owing to technical problems during the observations, the only usable configuration for G19 was the compact one, while for G10 it was the extended one. The bandpass of the receivers was calibrated by observations of the quasar 3C 273 for all the hot cores in the sample. Amplitude and phase calibrations were achieved by monitoring 1730–130 and 1741–038, whose flux densities were determined relative to MWC 349 or 1749+096. The flux densities estimated for 1730–130 are in the range 0.78–1.71 Jy at 1.4 mm, while those for 1741–038 are in the range 2.18–2.77 Jy at 1.4 mm. Flux calibration uncertainties are estimated to be ∼20 %. The synthesized CLEANed beams for maps made using natural weighting can be found in Table 2.1. The V_{LSR} for each hot core listed in Table 2.1 has been determined from high spatial resolution observations of the $12_K - 11_K$ K-components of $CH_3{}^{13}CN$.

These observations range from 220.210 to 220.760 GHz for all the hot cores and were analysed using the GILDAS software package.[1]

2.3 The sample of hot cores

The sample comprises of six luminous ($L_{bol} > 10^4\,L_\odot$) objects with typical signposts of massive star formation such as water masers and ultracompact (UC) HII regions.

Six hot cores were observed towards five star-forming regions on the basis of being bright in the sub-millimetre, and having previously given indications of being chemically rich:

G31.41+0.31: Figure 2.1 shows G31 mapped in 3.3 mm (left panel) and 1.4 mm (right panel) continuum emission using the PdBI, taken from Beltrán et al. (2005). This is a well-studied hot core located at 7.9 kpc (Cesaroni et al. 1994, 1998), with evidence of a rotating massive molecular toroid, suggested by OH maser emission and confirmed using CH_3CN emission (Gaume & Mutel 1987; Beltrán et al. 2004, 2005; Cesaroni et al. 2011). It

[1] http://www.iram.fr/IRAMFR/GILDAS

Table 2.1: Parameters of the IRAM PdBI observations

Source	α(J2000)† (h m s)	δ(J2000) (°′″)	V_{LSR} (kms^{-1})	Distance kpc	Luminosity $L_\odot$
G31.41+0.31	18 47 34.330	-01 12 46.50	96.8[a]	7.9	6.0×10^6
G29.96-0.02	18 46 03.955	-02 39 21.87	98.9[b]	3.5	3.2×10^5
G19.61-0.23	18 27 38.145	-11 56 38.49	41.6[b]	12.6	2.2×10^6
G10.62-0.38	18 10 28.650	-19 55 49.50	-2.0[b]	3.4	0.4×10^6
G24.78+0.08	18 36 12.660	-07 12 10.15	110.8[a]	7.7	7.0×10^4
Source	Synthesized Beam †† (″)	P.A. (°)	Resolution (kms^{-1})	Config.	Hot core mass $M_\odot$
G31.41+0.31	1.1 × 0.5	-170	3.4	A	490
G29.96-0.02	1.4 × 0.7	168	3.4	A, C	28
G19.61-0.23	2.6 × 1.0	161	3.4	B, C	415
G10.62-0.38	2.4 × 0.7	169	3.4	B, C	82
G24.78+0.08	1.2 × 0.5	-174	3.4	A	A1:130 A2:80

† Coordinates of the phase centre of the observations as used by Beltrán et al. (2005) and Beltrán et al. (2011).
†† The synthesized CLEANed beams for maps made using natural weighting as derived by Beltrán et al. (2005) and Beltrán et al. (2011).
[a]Beltrán et al. (2005)
[b]Beltrán et al. (2011)

has been mapped in several different molecules including SiO, HCO^+ and NH_3, as well as several complex molecules like CH_3CN, C_2H_5CN and $CH_2(OH)CHO$ (Cesaroni et al. 1994; Maxia et al. 2001; Beltrán et al. 2005). Interferometric observations of molecular lines with high excitation energies have revealed the presence of deeply-embedded YSOs, which in all likelihood explains the temperature increase toward the core centre (Beltrán et al. 2004, 2005; Cesaroni et al. 2010). The Spitzer/GLIMPSE images by Benjamin (2003) show that the G31 hot core lies in a complex parsec-scale region where both extended emission and multiple stellar sources are detected.

G29.96–0.02: Figure 2.2 shows G29 mapped in 2.7 mm (left panel) and the 1.4 mm (right panel) continuum emission (contours) on the CH_3CN (6–5) emission (grayscale) averaged under the K = 0, 1, 2, 3, and 4 components (left panel) and CH_3CN (12–11) emission (grayscale) averaged under the K = 0, 1, 2, and 3 components (right panel), taken from Beltrán et al. (2011). G29 is located at a distance of 3.5 kpc (Beltrán et al. 2011) and associated with the infrared source IRAS 18434-0242. It contains a cometary UCHII region with a hot core located in front of the cometary arc (Wood & Churchwell 1989;

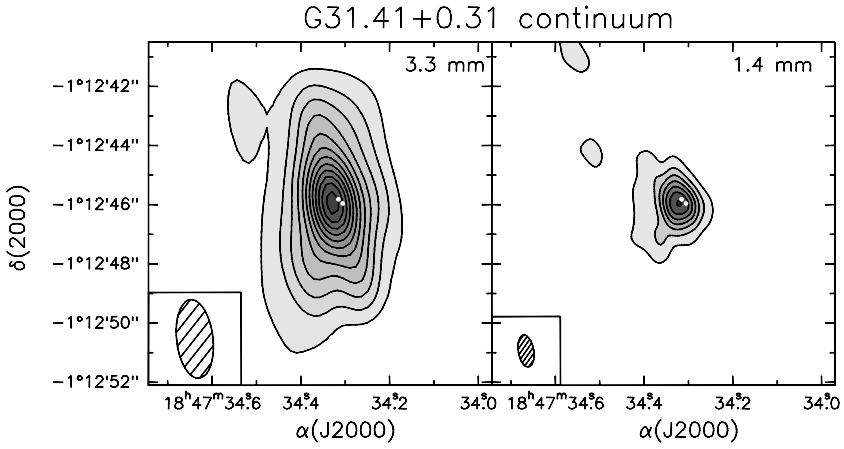

Figure 2.1: G31.41+0.31 mapped in 3.3 mm (left panel) and 1.4 mm (right panel) continuum emission by Beltrán et al. (2005) using the PdBI. The contour levels range from 20 to 240 mJy beam^{-1} in steps of 20 mJy beam^{-1} for the 3.3 mm map, and from 100 to 1300 mJy beam^{-1} in steps of 200 mJy beam^{-1} for the 1.4 mm map. This figure is taken from Beltrán et al. (2005).

Cesaroni et al. 1994). It has been mapped in several molecules including NH_3, HCO^+, CS, CH_3CN, HNCO and $HCOOCH_3$ (Cesaroni et al. 1998; Pratap et al. 1999; Maxia et al. 2001; Olmi et al. 2003; Beuther et al. 2007). A velocity gradient along the east-west direction has been measured in NH_3, CH_3CN, and $HN^{13}C$ emission which is interpreted as rotation (Cesaroni et al. 1998; Olmi et al. 2003; Beuther et al. 2007). On the other hand, an outflow directed along the southeast-northwest direction has been mapped in H_2S and SiO by Gibb et al. (2004) and Beuther et al. (2007). Beltrán et al. (2001) confirmed the existence of a rotating molecular toroid around the outflow axis. Masers of H_2O, CH_3OH and H_2CO have also been detected around this hot core (Hofner & Churchwell 1996; Walsh et al. 1998; Hoffman et al. 2003).

G19.61–0.23: Figure 2.2 shows G19 mapped in 2.7 mm (left panel) and the 1.4 mm (right panel) continuum emission (contours) on the CH_3CN (6–5) emission (grayscale) averaged under the K = 0, 1, 2, 3, and 4 components (left panel) and CH_3CN (12–11) emission (grayscale) averaged under the K = 0, 1, 2, and 3 components (right panel), taken from Beltrán et al. (2011). G19 is located at a distance of 12.6 kpc (Kolpak et al. 2003), and associated with the infrared source IRAS 18248–1158. It contains several embedded UCHII regions, detected by Garay et al. (1985), and more recently mapped by Furuya et al. (2005). Several molecular tracers, such as CS, NH_3, CH_3CH_2CN, $HCOOCH_3$, and CH_3CN

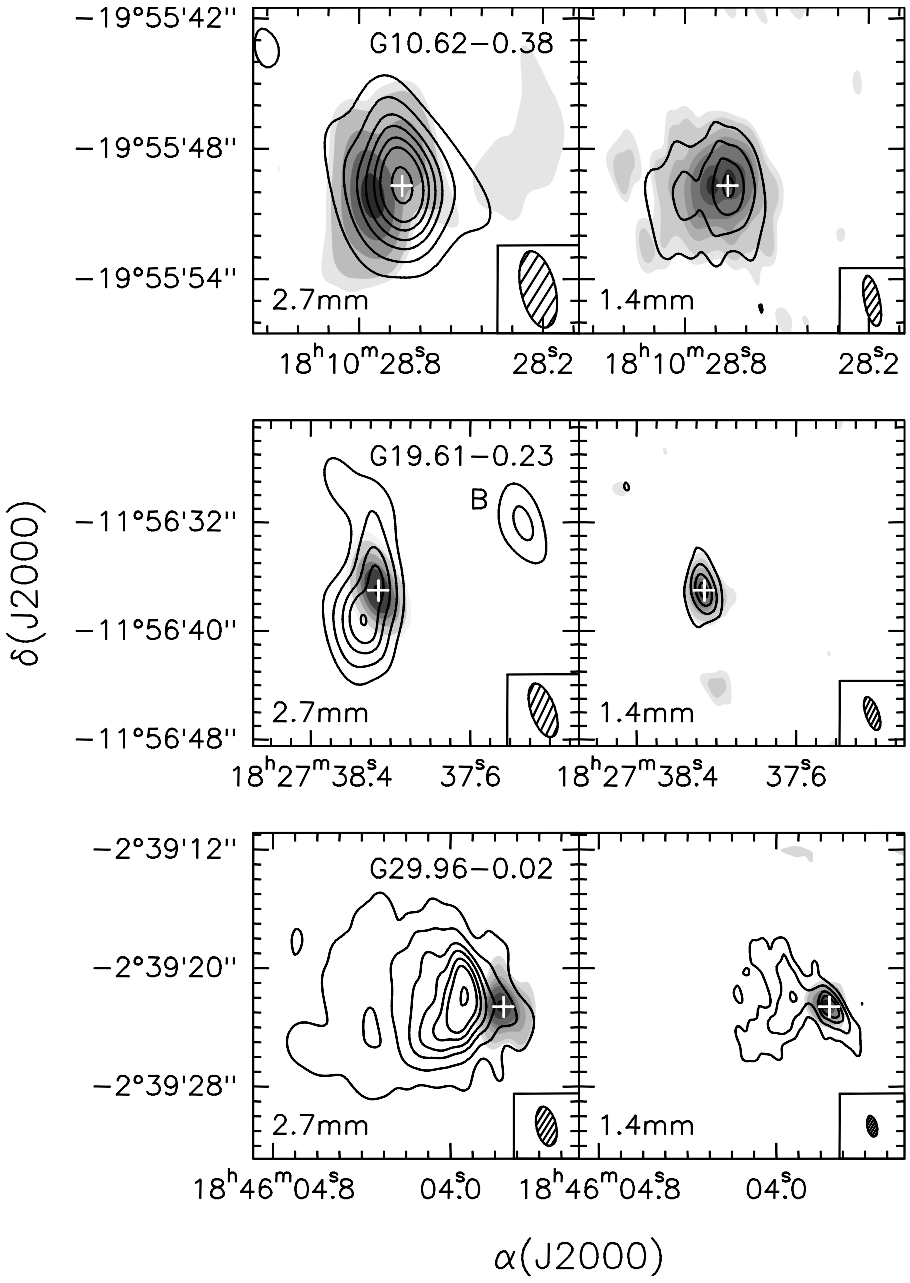

Figure 2.2: G29.96–0.02, G19.61–0.23, and G10.62–0.38 mapped with the PdBI in the 2.7 mm (left panel) and the 1.4 mm (right panel) continuum emission (contours) on the CH_3CN (6–5) emission (grayscale) averaged under the K = 0, 1, 2, 3, and 4 components (left panel) and CH_3CN (12–11) emission (grayscale) averaged under the K = 0, 1, 2, and 3 components (right panel), taken from Beltrán et al. (2011). The contour levels are 3, 9, 18, 27, 39, 51, and 75 times σ, where 1σ is 3 mJy beam^{-1} at 2.7 mm and 6.7 mJy beam^{-1} at 1.4 mm for G29, 3, 9, 18, 27, 39, 51, and 75 times σ, where 1σ is 6 mJy beam^{-1} at 2.7 mm and 33.3 mJy beam^{-1} at 1.4 mm for G19, and 3, 9, 18, 27, 39, 51, and 75 times σ, where 1σ is 17 mJy beam^{-1} at 2.7 mm and 26.7 mJy beam^{-1} at 1.4 mm for G10. The Grayscale contour levels are 3, 5, 10, 15, 20, 30, and 40 times σ, where 1σ is 6 mJy beam^{-1} at 2.7 mm and 65 mJy beam^{-1} at 1.4 mm for G29, 3, 5, 10, 15, 20, 30, and 40 times σ, where 1σ is 30 mJy beam^{-1} at 2.7 mm and 50 mJy beam^{-1} at 1.4 mm for G19, and 3, 5, 10, 15, 20, 30, and 36 times σ, where 1σ is 15 mJy beam^{-1} at 2.7 mm and 15 mJy beam^{-1} at 1.4 mm for G10.

have been mapped in this hot core (Plume et al. 1992; Garay et al. 1998; Remijan et al. 2004; Furuya et al. 2005). ^{13}CO and C^{18}O emission show inverse P Cygni profiles indicating infalling gas towards the core (Wu et al. 2009; Furuya et al. 2011). López-Sepulcre et al. (2009) mapped a ^{13}CO outflow without a well-defined morphology. H_2O, OH, and CH_3OH masers have been detected by Forster & Caswell (1989), Hofner & Churchwell (1996) and Walsh et al. (1998). Beltrán et al. (2011) reported velocity gradients, observed in CH_3CN, oriented perpendicular to the direction of a molecular outflow.

G10.62–0.38: Figure 2.2 shows G10 mapped in 2.7 mm (left panel) and the 1.4 mm (right panel) continuum emission (contours) on the CH_3CN (6–5) emission (grayscale) averaged under the K = 0, 1, 2, 3, and 4 components (left panel) and CH_3CN (12–11) emission (grayscale) averaged under the K = 0, 1, 2, and 3 components (right panel), taken from Beltrán et al. (2011). G10 is located at a distance of 3.4 kpc (Blum et al. 2001) and contains a well-studied UCHII region (e.g. Wood & Churchwell 1989) associated with the infrared source IRAS 18075–1956. The hot core in this star forming region has been mapped in NH_3 (Ho & Haschick 1986; Keto et al. 1987, 1988; Sollins & Ho 2005) and in SO_2 and OCS (Klaassen et al. 2009). Infall and bulk rotation in the molecular gas surrounding the UCHII region have been detected. H66α emission shows the occurrence of inward motions in the ionized gas (Keto 2002). CH_3OH and H_2O masers have been mapped towards the core and are distributed linearly in the plane of the rotation (Hofner & Churchwell 1996; Walsh et al. 1998), while OH masers appear to lie along the axis of rotation (Argon et al. 2000). Outflow activity has been detected by Keto & Wood (2006), López-Sepulcre et al. (2009) and by Beltrán et al. (2011), who reported a CH_3CN toroid rotating around the main axis of the outflow.

G24.78+0.08A1 and G24.78+0.08A2: Figure 2.3 shows a combined BIMA and PdBI map of the 3.3 mm continuum emission (left panel) and a PdBI map of the 1.4 mm continuum emission (right panel) toward G24, taken from Beltrán et al. (2005). G24 is a high-mass star-forming region located at 7.7 kpc from the Sun, and associated with several YSOs in different evolutionary phases embedded in their parental cores (Furuya et al. 2002). The G24 region has been extensively studied in various molecules like CO, NH_3 and CS, as well as in complex molecules and in the continuum (Codella et al. 1997; Cesaroni et al. 2003; Beltrán et al. 2005, 2011). Two main groups of YSOs, called A1 and A2, are separated by $\sim$1$''$.5 (Beltrán et al. 2011 and references therein). *G24.78+0.08A1:* G24A1 is one of the three massive cores with a rotating toroid detected in G24 (Beltrán et al.

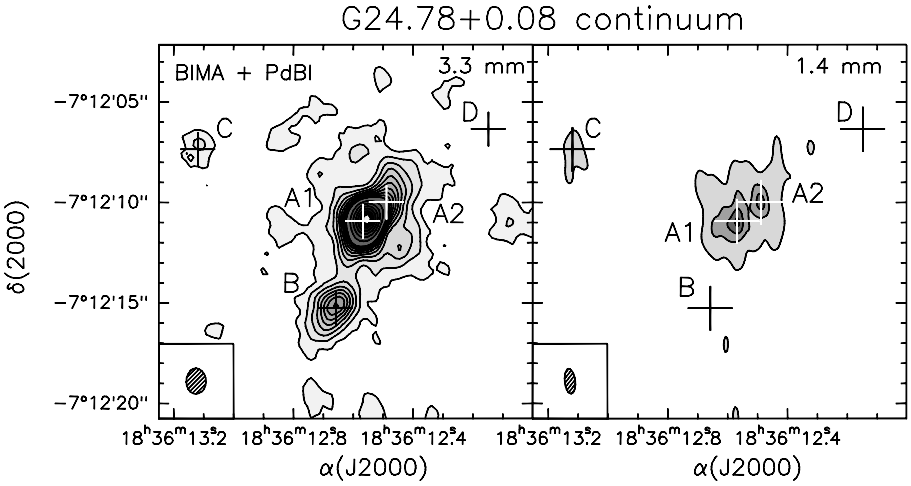

Figure 2.3: A combined BIMA and PdBI map of the 3.3 mm continuum emission (left panel) and a PdBI map of the 1.4 mm continuum emission (right panel) toward G24, taken from Beltrán et al. (2005). The contour levels range from 2 to 20 mJy beam^{-1} in steps of 2 mJy beam^{-1} and from 20 to 80 mJy beam^{-1} in steps of 10 mJy beam^{-1} for the 3.3 mm map, and from 20 to 200 mJy beam^{-1} in steps of 60 mJy beam^{-1} for the 1.4 mm map.

2011). At the centre of G24A1, an unresolved hypercompact (HC) HII region is created by a YSO with a spectral type of at least O9.5 (Codella et al. 1997; Beltrán et al. 2007). NH_3 (2,2) observations have revealed that the gas in the toroid is undergoing infall towards the HC HII region (Beltrán et al. 2006), suggesting that accretion on to the star might still be occurring, even through the ionized region (for a potential mechanism, see Keto & Wood 2006). On the other hand, Very Long Baseline Array proper motion measurements of H_2O masers associated with the HC HII region (Moscadelli et al. 2007) indicate that the ionized region might be expanding, thus questioning the possibility of accretion on to the star. *G24.78+0.08A2:* G24A2 is also associated with a massive CH_3CN toroid, rotating around the main axis of a bipolar outflow observed in the CO isotopologues (Furuya et al. 2002; Beltrán et al. 2005, 2011; Codella et al. 2013). The mid-infrared and radio continuum measurements show a compact (1000–2000 au) source which could be due to an ionized jet (Vig et al. 2008). Emission from several complex molecules clearly indicate the presence of a molecular hot core (Beltrán et al. 2005, 2011; Codella et al. 2013).

2.4 Molecular content

Figure 2.4 shows the reduced spectrum for each hot core, including labels for the identified lines (Beltrán et al. 2005) as well as the seven unidentified lines in G31, A to G in ascending frequency in the top panel. As can be seen from the figure, not all lines are present in all cores. Lines C, D, F and G were too blended with other lines to be clearly identified. Table 2.4 lists the previously unidentified lines which could be identified (A, B and E), with their frequencies and observational parameters, and which cores they are detected in. These will be discussed in Sect. 2.4.4. Several of the molecular lines identified in G31, G24A1 and G24A2 by Beltrán et al. (2005) are also seen in other members of the sample of hot cores. These new detections are discussed in Sect. 2.4.3.

In order to determine the identity of all the spectral lines in the sample of hot cores, the method described in Section 2.1 was used. The Splatalogue database was used to determine a list of candidate line identities, in order for a multitude of catalogues to be searched simultaneously. Any line with a measured laboratory frequency uncertainty larger than 0.05 GHz was excluded from consideration. Since the spectral resolution of the observations is 0.0025 GHz, the search for lines was limited to within the linewidths of the unidentified lines. The list of potential lines has been reduced by excluding transitions with an upper energy level over 1000 K, as typically excitation temperatures of the present hot core sample do not exceed ∼300 K (e.g. Beltrán et al. 2005; Beltràn et al. 2010 and references therein) and to date, the highest upper energy level of a transition previously detected in the hot core sample is 931 K.

2.4.1 Fitting procedure

Every line described in this chapter is fitted using the method Gauss command in the class software package, which allows the user to input an initial T_{peak}, FWHM, and line centre from a visual inspection of the data. These parameters can either be fixed or set to vary as the program iterates to find the best fit. For very complex blends it can be necessary to fix one or more of these parameters in order to generate a sensible fit for all blended lines. In the following chapter all Gaussian fits have been derived with free parameters unless otherwise stated.

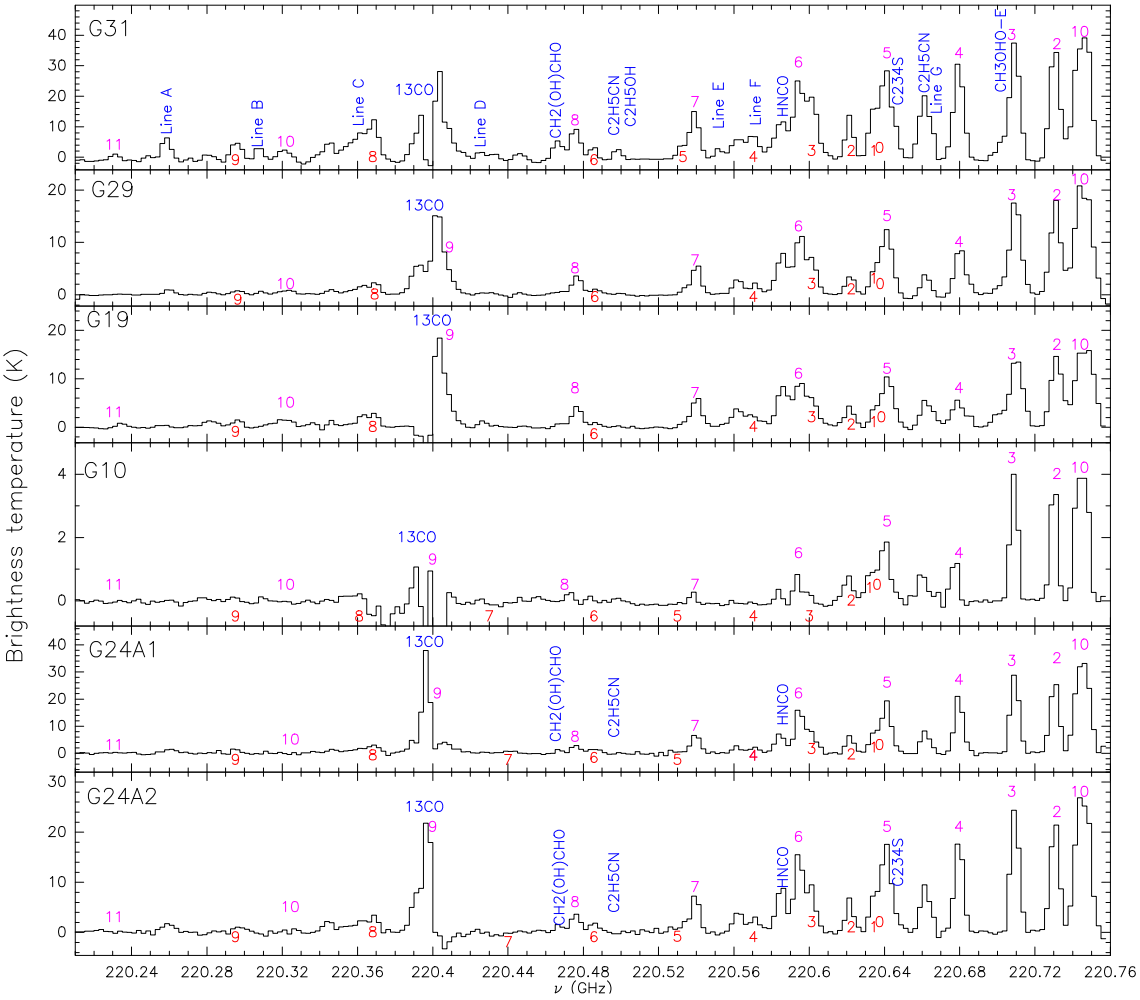

Figure 2.4: Spectra of the hot cores G31, G29, G19, G10, G24A1 and G24A2 observed with the PdBI (Beltrán et al. 2005, 2011), integrated over the 3σ contour level area. The species labelled are those that have already been identified in Beltrán et al. (2005) and Beltrán et al. (2011) as well as the seven lines in G31 that were found but not identified by Beltrán et al. (2005). The numbers indicate the position of the CH_3CN $(12_K - 11_K)$ K-components in the upper part (in pink) of each spectra and of the $CH_3\ ^{13}CN$ $(12_K - 11_K)$ K-components in the lower part (in red).

2.4.2 Error calculations

We compute the integrated intensity error ($\delta(\int T\,\mathrm{d}v)$) as in Isokoski et al. (2013), whereby:

$$\delta(\int Tdv) = c^{st}[\Delta V\delta(T_{peak}) + T_{peak}\delta(\Delta V)], \tag{2.1}$$

where $c^{st} = (\sqrt{\pi/ln2)}/2)$, T_{peak} is the peak temperature and ΔV is the FWHM of the line.

The peak temperature error can be determined using:

$$\delta(T_{peak}) = \sqrt{rms^2 + (cal \times T_{peak})^2 + \sigma^2_{Tpeak}} \tag{2.2}$$

The FWHM error can be determined using:

$$\delta(\Delta V) = \sigma_{\Delta V}, \tag{2.3}$$

where rms is the root mean square amplitude of the noise, cal is the flux calibration uncertainty of the telescope, and σ_{Tpeak} and $\sigma_{\Delta V}$ are the statistical errors on T_{peak} and ΔV from the Gaussian fits.

2.4.3 New detections

In this subsection, we identify lines in the G10, G19 and G29 hot cores, which have already been detected in G31, and in most cases already detected in G24A1 and G24A2 as well. Table 2.2 shows the derived frequency, velocity, integrated intensity, FWHM, peak temperature and rms of the baseline for these newly detected lines in each hot core and the transitional information can be found in Table 2.3.

The $9_{4,5}$ – $10_{3,8}$ transition of vinyl cyanide (C_2H_3CN), a common hot core molecule (Gibb et al. 2000; Wirström et al. 2007), was identified at 220.34476 GHz in G31 by Beltrán et al. (2005). In the observations presented in this chapter, a line at a similar frequency is seen in a further three hot cores, G19, G24A1 and G24A2 (Fig. 2.5). This line is blended with line C and the K=8 component of $^{13}CH_3CN(12 - 11)$ in all the hot cores, but separated by more than the Rayleigh criterion. The line seen in G19 has a FWHM

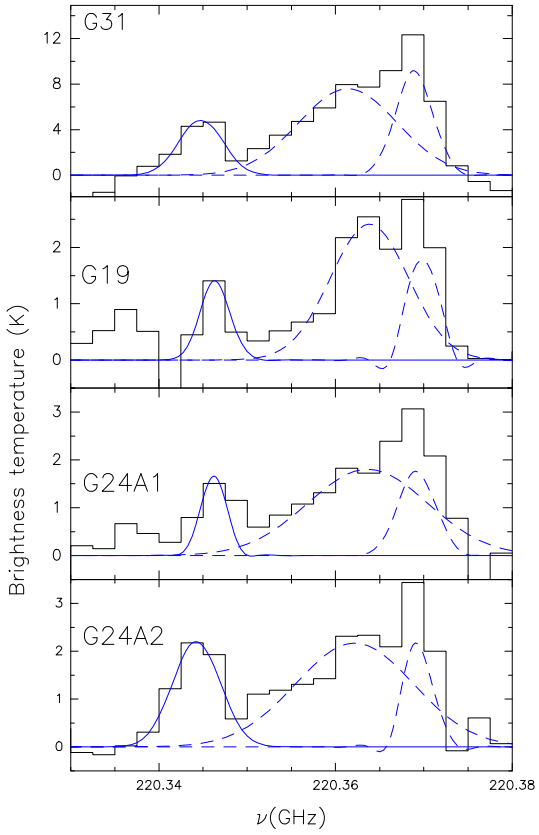

Figure 2.5: C_2H_3CN spectra with Gaussian fits, integrated over the 3σ contour level area toward G31, G19, G24A1 and G24A2 as seen with the PdBI. This transition was previously detected in G31 and G24 in (Beltrán et al. 2005) and is detected in G19 in this work.

of $5.3\,\mathrm{km s^{-1}}$, which is larger than the spectral resolution of the observations ($3.4\,\mathrm{km s^{-1}}$), however, it is affected by some missing flux at 220.341 GHz. We therefore postulate that our fits derived for vinyl cyanide in G19 may underestimate the flux of this line.

In these observations the $10_{6,4}$ – $9_{6,3}$ transition of DCO_2H is also detected in G29 and G19 (Fig. 2.6). From the Gaussian fit of these lines, however, we find that in G19 the blend of DCO_2H and the $CH_3{}^{13}CN$ (12–11) K=4 transition do not pass the rayleigh criterion, as described in Section 2.1. Whilst DCO_2H is clearly present in G19, the value of its line flux determined from the Gaussian fit is uncertain due to this severe blend. The percentage error of the $\int T\,\mathrm{d}v$ fit for this molecule ranges from 16 – 35 %, where the worst fit is for G24A2.

The $10_{1,9}$ – $9_{1,8}$ transition of HNCO is detected in a further two hot cores, G19 and G29 (see Fig. 2.7), although it is blended with two lines of methyl cyanide in all cores. In G19 and G29 HNCO is separated by the rayleigh criterion from methyl cyanide, however, in the detection reported by Beltrán et al. (2005) in G31, G24A1, and G24A2, HNCO

Table 2.2: The observed frequency, velocity, area of Gaussian fit, FWHM, peak brightness temperature and the rms of the baseline for molecules previously detected in Beltrán et al. (2005) and confirmed in new cores in this work. Spectra are integrated over the 3σ contour level.

Molecule	Frequency† (GHz)	V_{LSR} (kms^{-1})	V_{peak}† (kms^{-1})	$\int T\,dv$ (Err††) ($Kkms^{-1}$)	FWHM (Err††) (kms^{-1})	T_B (Err††) (K)	rms (K)
			G31.41+0.31				
C_2H_3CN	220.34476	96.8	96.6	41.0 (25.0)	7.9 (3.0)	4.9 (1.1)	0.3
CH_2OHCHO	220.46635	96.8	93.6	40.5 (9.1)	6.8 (0.1)	5.6 (1.2)	0.3
DCO_2H	220.56215	96.8	95.9	78.3 (35.9)	13.2 (2.3)	5.6 (1.5)	0.9
HNCO	220.58558	96.8	96.5	174.9 (68.9)	14.9 (2.4)	11.1 (2.6)	0.9
C_2H_5CN	220.66145	96.8	96.3	203.5 (84.6)	9.7 (2.0)	19.7 (4.1)	0.3
			G29.96–0.02				
CH_2OHCHO	220.46753	98.9	93.9	6.5 (4.3)	10.9 (2.1)	0.6 (0.3)	0.2
DCO_2H	220.56200	98.9	98.0	25.2 (10.2)	8.1 (1.2)	3.0 (0.7)	0.3
HNCO	220.58586	98.9	98.0	85.2 (21.0)	10.4 (0.4)	7.8 (1.6)	0.3
C_2H_5CN	220.66196	98.9	97.5	29.3 (19.0)	6.9 (2.5)	4.0 (1.1)	0.8
			G19.61–0.23				
C_2H_3CN	220.34636	41.6	39.0	8.0 (4.8)	5.3 (1.8)	1.4 (0.5)	0.2
CH_2OHCHO	220.46767	41.6	36.4	5.8 (3.6)	6.9 (1.9)	0.8 (0.3)	0.2
DCO_2H	220.56143	41.6	41.5	20.1 (8.3)	7.5 (0.7)	2.5 (0.8)	0.6
HNCO	220.58625	41.6	40.2	95.4 (21.3)	10.8 (0.2)	8.3 (1.7)	0.2
C_2H_5CN	220.66277	41.6	39.1	61.0 (22.1)	10.8 (0.9)	5.3 (1.5)	0.9
			G24.78+0.08 A1				
C_2H_3CN	220.34619	110.8	108.6	8.1 (5.9)	4.6 (1.8)	1.7 (0.5)	0.2
CH_2OHCHO	220.46702	110.8	106.7	5.0 (2.0)	4.6 (0.5)	1.0 (0.3)	0.2
HNCO	220.58453	110.8	111.9	67.9 (34.8)	9.0 (2.5)	7.1 (1.7)	0.8
C_2H_5CN	220.66167	110.8	110.0	68.5 (27.0)	7.8 (1.2)	8.2 (2.0)	1.1
			G24.78+0.08 A2				
C_2H_3CN	220.34426	110.8	111.3	20.3 (9.0)	8.6 (1.5)	2.2 (0.6)	0.3
CH_2OHCHO	220.46694	110.8	106.8	10.3 (5.0)	5.8 (1.2)	1.7 (0.5)	0.3
DCO_2H	220.56208	110.8	110.0	25.1 (17.8)	7.0 (2.2)	3.4 (1.3)	0.8
HNCO	220.58465	110.8	111.8	59.2 (54.5)	6.4 (4.1)	8.7 (2.4)	0.8
C_2H_5CN	220.66167	110.8	110.0	83.0 (35.5)	8.4 (1.6)	9.3 (2.2)	1.0

† The small spread in frequency between the rest frequency of the line and the observed frequency for each molecule in each hot core, is due to the difference between the V_{LSR} and the V_{peak} in each hot core.

†† The error for $\int T\,dv$ given in brackets is determined from the fitting error and the calibration uncertainty in the flux measurement of the telescope, as in Section 2.4.2. The error for T_B is also determined as described in Section 2.4.2. The error for the FWHM is the fitting error.

Table 2.3: Transitional information for the molecules previously detected in Beltrán et al. (2005) and confirmed in new cores in this work. All this transitional information was taken from the JPL spectral line catalog.

Molecule	Transition	Frequency (GHz)	E_u (K)	$S\mu^2$ (D^2)	Hot core detected in
C_2H_3CN	9(4,5) – 10(3,8)E	220.34445	55.10	2.52	G31, G19, G24A1, G24A2
CH_2OHCHO	20(2,18) – 19(3,17)	220.46388	120.05	89.74	G31, G29, G19, G24A1, G24A2
DCO_2H	10(6,4) – 9(6,3)	220.56136	138.81	12.47	G31, G29, G19, G24A2
HNCO	10(1,9) – 9(1,8)	220.58520	101.50	27.83	G31, G29, G19, G24A1, G24A2
C_2H_5CN	25(2,24) – 24(2,23)	220.66092	143.02	367.60	G31, G29, G19, G24A1, G24A2

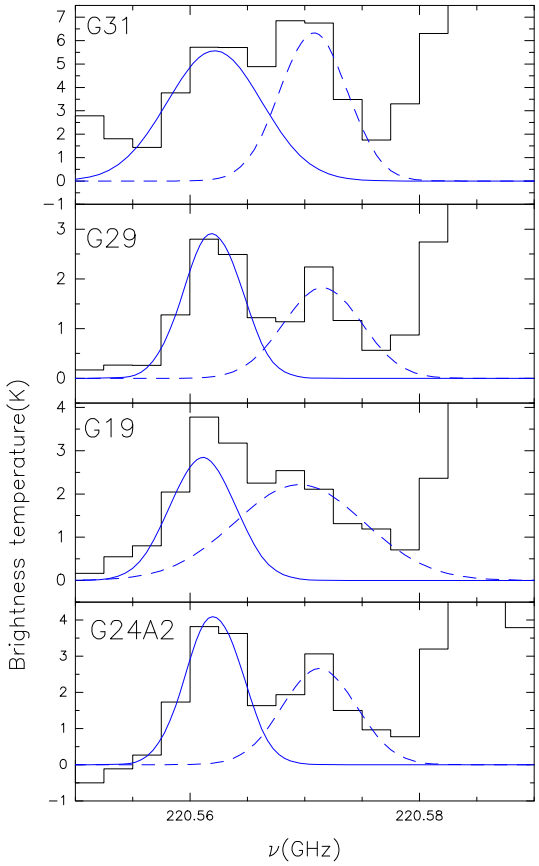

Figure 2.6: DCO_2H spectra with Gaussian fits, integrated over the 3σ contour level area toward G31, G29, G19 and G24A2 as seen with the PdBI. This transition was previously detected in G31 and G24A2 (Beltrán et al. 2005) and is detected in G19 and G29 in this work.

and methyl cyanide are not separated by the rayleigh criterion. The percentage error of the $\int T\,\mathrm{d}v$ fit is highest in G24A2 (60 %), and lowest in G19 (2 %). This indicates the fit in G24A2 is poor and additional transitions should be detected, in order to determine accurate column densities for HNCO in G24A2.

The $25_{2,24} - 24_{2,23}$ transition of C_2H_5CN was also detected in G31, G24A1 and G24A2 in Beltrán et al. (2005). In this work, it has been found in a further two hot cores: G19 and G29 (Fig. 2.8). This line is very bright in G31 at 19.7 K, but is as weak as 4.0 K in G29. The FWHM is similar in all the hot cores, ranging from 6.9 kms^{-1} in G29 to 10.8 kms^{-1} in G19. It is not detected in G10. The percentage error of the $\int T\,\mathrm{d}v$ fit ranges from 7 % – 31 %, where the fit is poorest in G29. All of these lines are brightest in G31.

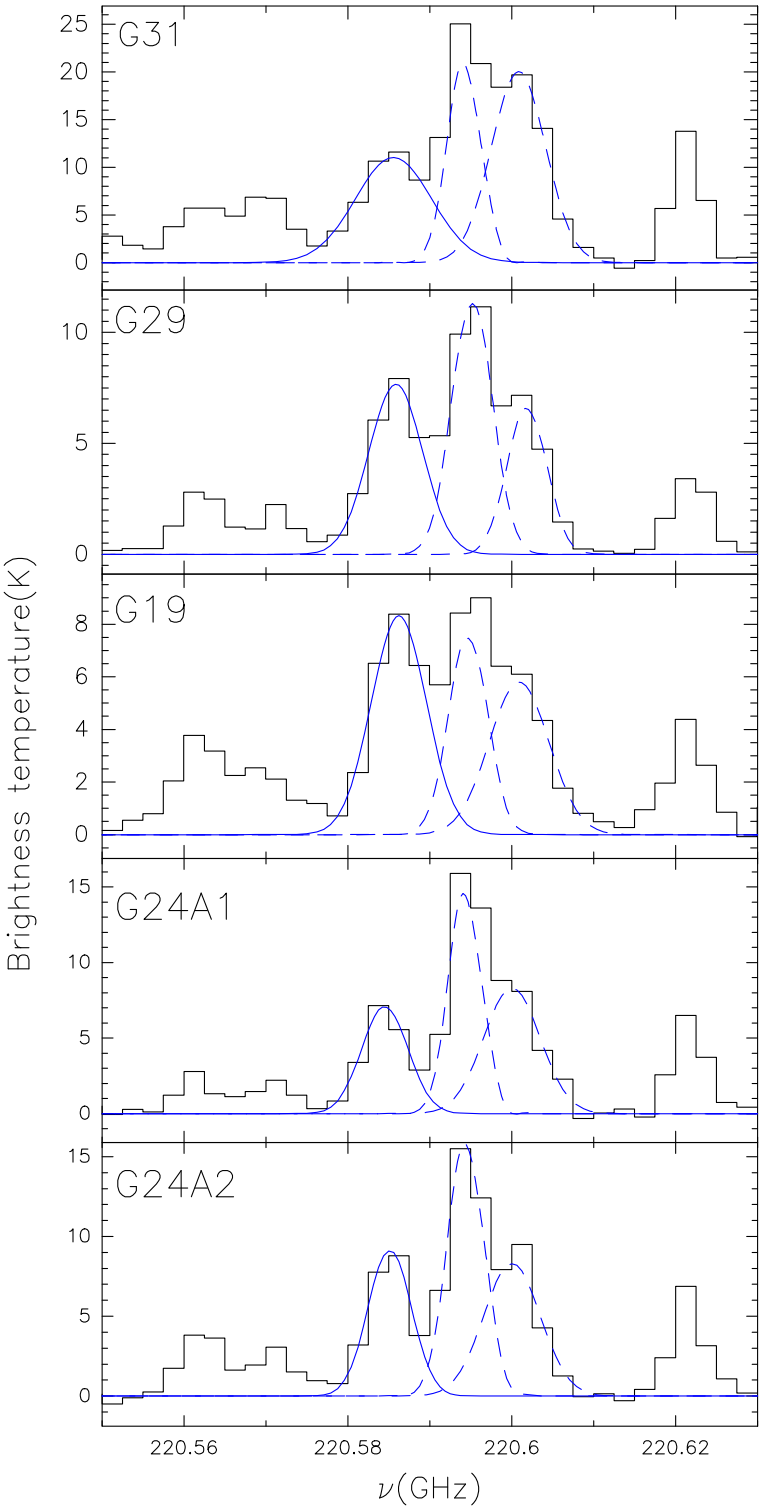

Figure 2.7: HNCO spectra with Gaussian fits, integrated over the 3σ contour level area towards G31, G29, G19, G24A1 and G24A2 as seen with the PdBI. This transition was previously detected in G31, G24A1 and G24A2 (Beltrán et al. 2005) and is detected in G19 and G29 in this work.

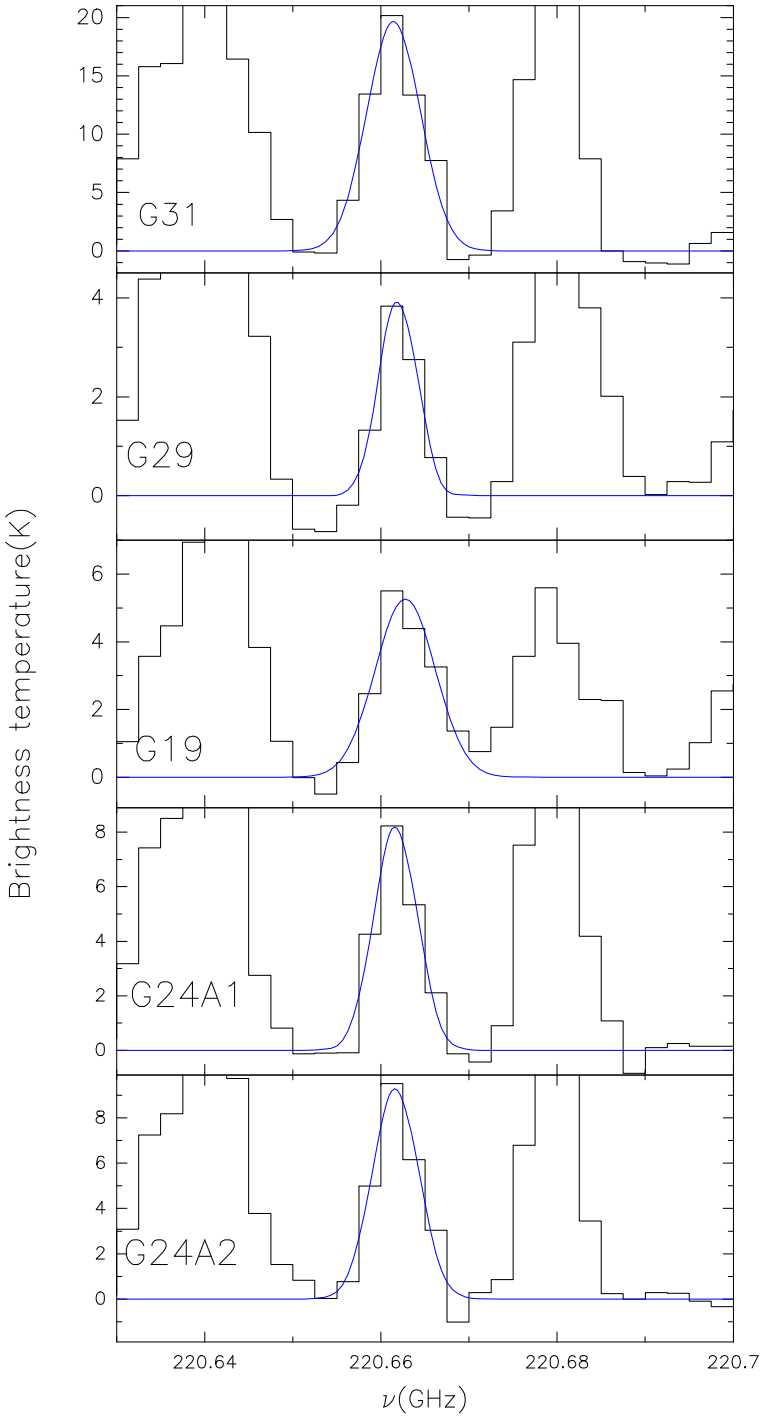

Figure 2.8: C_2H_5CN spectra with Gaussian fits, integrated over the 3σ contour level area towards G31, G29, G19, G24A1 and G24A2 as seen with the PdBI. This transition was previously detected in G31, G24A1 and G24A2 in Beltrán et al. (2005) and is detected in G19 and G29 in this work.

Glycolaldehyde ($CH_2(OH)CHO$)

The complex organic molecule (COM) glycolaldehyde (CH_2OHCHO), which is an isomer of both methyl formate ($HCOOCH_3$) and acetic acid (CH_3COOH), is the simplest of the monosaccharide sugars. This important organic molecule was detected for the first time in the Galactic Centre cloud, Sgr B2(N) (Hollis et al. 2000), and detected tentatively at 1.4 mm for the first time outside the Galactic Centre towards three massive hot cores (G31, G24A1, and G24A2) by Beltrán et al. (2005). Later on, Beltrán et al. (2009) confirmed the detection by observing two additional Glycolaldehyde transitions towards G31 at 2.1 and 2.9 mm with the PdBI. Recently, Jørgensen et al. (2012) have detected thirteen transitions towards the Class 0 object IRAS 16293–2422 at 0.4 and 1.4 mm, using the ALMA array towards the hot–corino surrounding the solar–type protostar.

In this work, a new detection of a line is seen at ∼220.466 GHz in two hot cores (Fig. 2.9), G29 (3σ detection) and G19 (5σ detection). This is likely to be the $20_{2,18}$ – $19_{3,17}$ transition of glycolaldehyde, as was detected by Beltrán et al. (2005) in G31, G24A1 and G24A2. A shift is observed in the velocity of 3 – 4 kms^{-1} in this transition compared to the V_{LSR} of each hot core. This is consistent with the glycolaldehyde observations of both Beltrán et al. (2009), Halfen et al. (2006), and Hollis et al. (2000). Whilst further transitions of this molecule are needed to confirm its presence within G29 and G19, if confirmed, it would suggest that glycolaldehyde is a common hot core tracer. In both hot cores this line is blended with two methyl cyanide lines, as it is in G31, G24A1 and G24A2. The $46_{20,26} - 46_{19,27}$ EE transition (E_u = 816 K, $S\mu^2$ = 2843 D^2) of acetone may also be contributing to the emission seen at this frequency. This is consistent with the observations by Fuente et al. (2014), where they detect the $20_{2,18} - 19_{3,17}$ transition of glycolaldehyde at 220.466 GHz, blended with acetone. In Chapter 3, both glycolaldehyde and acetone emission are modelled to explore this possibility.

Figure 2.10 shows a map of the $18_{8,10} - 17_{8,9}$E methyl formate emission (blue contours; line A, see Section 2.4.4), the $20_{2,18} - 19_{3,17}$ glycolaldehyde emission (white contours) and the averaged emission of the K=0, 1, 2 (12 – 11) transitions of methyl cyanide emission (colour scale) in G31, G24A1, G24A2 and G29 (i.e. the four hot cores for which the three molecular species have been detected). Methyl cyanide is a typical hot core tracer. For G24A1, G24A2, and G29 the three species seem to be tracing the same material and peak at roughly the same position towards the dust emission peak. On the other

hand, in G31 glycolaldehyde peaks towards the centre of the core where the continuum source(s) is(are) embedded, whilst methyl formate and methyl cyanide show a different morphology. In particular, as reported by Beltrán et al. (2005), the methyl cyanide traces a toroidal structure with the strongest emission eastwards of the millimetre continuum emission peak, which is located towards the central dip. Beltrán et al. (2005) explained these apparent toroidal morphology as caused by the high optical depth and the existence of a temperature gradient in the core. On the other hand, methyl formate does not show a toroidal morphology but peaks towards the eastern side of the core, at a position barely coincident with that of the methyl cyanide. In this scenario, glycolaldehyde appears to be less affected by excitation conditions, and a better tracer of the inner conditions of the hot core closer to the embedded protostar(s). Methyl formate emission extends to 0.13 pc ($3\farcs5$) in G31 where the glycolaldehyde extends to 0.08 pc ($2''$). In G24, both methyl formate emission and glycolaldehyde emission extend to 0.11 pc ($3''$). In G29, both methyl formate emission and glycolaldehyde emission extend to 0.05 pc ($3''$).

2.4.4 New identifications

In this Section, the identification of some of the lines that were previously unidentified (see Fig. 2.4) is discussed, namely A, B and E , for each source, and the frequency, area of the Gaussian fitted, FWHM and peak brightness temperature are compared in each hot core for each of the lines (see Table 2.4). It is clear from Fig. 2.4 that the spectra do vary among hot cores and that G31, the brightest hot core with $L_{\rm bol} > 10^4 L_{\odot}$ (Beltrán et al. 2005) is the most chemically–rich hot core in the sample. Lines C, D, F and G labelled in this figure could not be identified.

Line A is seen in four of the hot cores in the sample: G31, G29, G24A1 and G24A2 (Fig. 2.12). A Gaussian profile has been fitted to this line in each of the hot cores to determine their rest frequency, integrated intensity, FWHM, and brightness temperature (see Table 2.4). There is only a small spread in the observed rest frequency of this line from 220.258240 to 220.260657 GHz, suggesting it is the same line in each hot core. Line A is the brightest in G31, as expected. The FWHM range from 7.6 $\rm kms^{-1}$ in G29 to 11.1 $\rm kms^{-1}$ in G24A1.

The potential identities of line A consist of three lines of methyl formate ($HCOOCH_3$): $18_{8,10}$ – $17_{8,9}$E, $24_{2,23}$ – $24_{1,24}$E, and $24_{2,23}$ – $24_{0,24}$E; one line of methylene amidogen (H_2CN): $3_{2,1}$ – $2_{2,0}$,F=11/2-9/2, (n=0 – 0); and one line of vinyl alcohol (C_2H_3OH): $11_{2,10}$

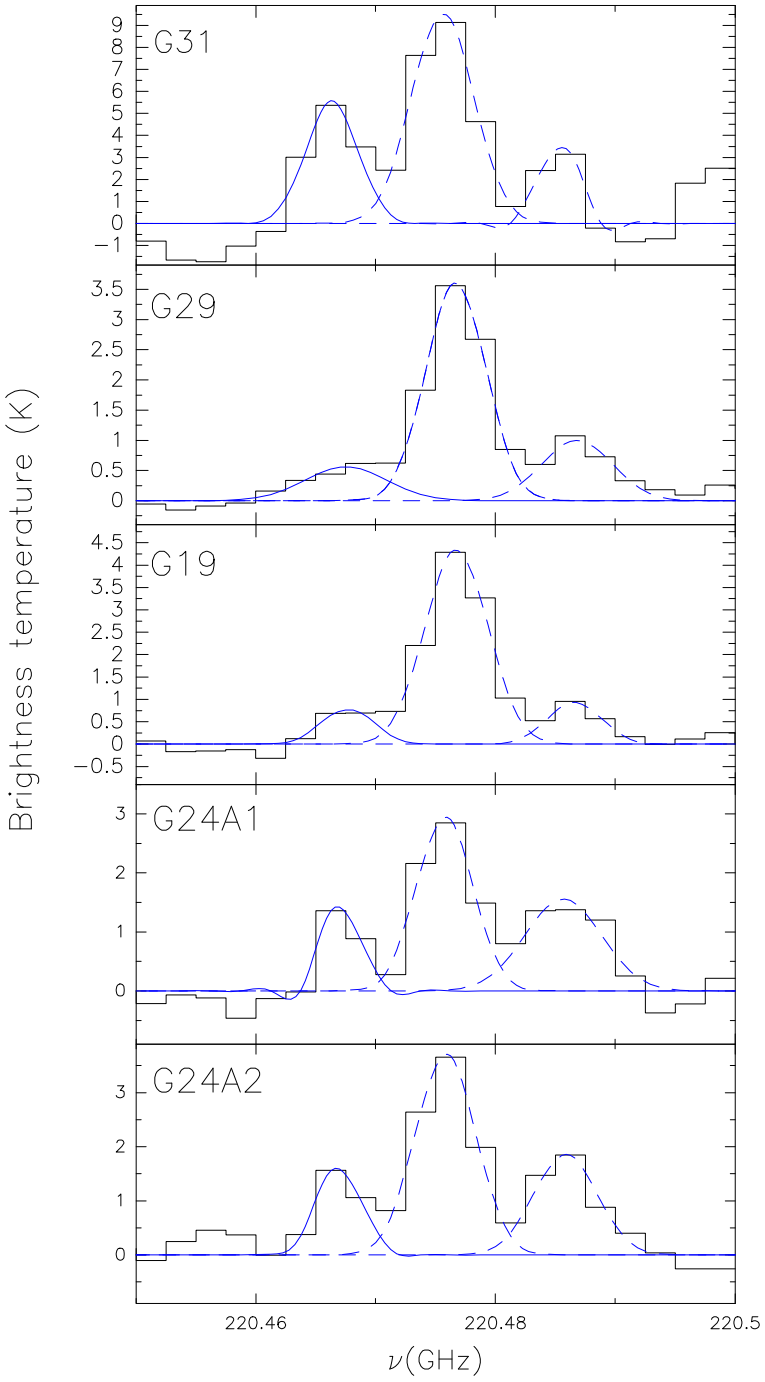

Figure 2.9: $CH_2(OH)CHO$ spectra with Gaussian fits, integrated over the 3σ contour level area towards G31, G29, G19, G24A1 and G24A2 as seen with the PdBI. This transition was previously detected in G31, G24A1 and G24A2 in Beltrán et al. (2005) and is detected in G19 and G29 in this work. In G29 it is only detected at a 3σ level.

Table 2.4: The observed frequency, velocity, area of Gaussian fit, FWHM, peak brightness temperature and the rms of the baseline for lines A, B and E in each of the hot cores in the sample. Spectra are integrated over the 3σ contour level.

Object	Frequency† (GHz)	V_{LSR} (kms^{-1})	V_{peak} (kms^{-1})	$\int T\,dv$ (Err††) (K.kms^{-1})	FWHM (Err††) (kms^{-1})	$T_{B,peak}$ (Err††) (K)	rms (K)
				Line A			
G31	220.25826	96.8	96.8	72.0 (16.5)	8.2 (0.3)	7.8 (1.6)	0.3
G29	220.26005	98.9	96.2	8.3 (2.6)	7.6 (0.3)	1.0 (0.3)	0.2
G19				No detection rms = 0.2			
G10				No detection rms = 0.1			
G24A1	220.26065	110.8	107.5	17.4 (8.4)	11.1 (2.2)	1.5 (0.4)	0.2
G24A2	220.25928	110.8	109.2	19.4 (7.9)	10.3 (1.2)	1.8 (0.5)	0.3
				Line B			
G31	220.30769	96.8	96.8	37.4 (10.9)	7.1 (0.5)	5.0 (1.1)	0.3
G29				No detection rms = 0.2			
G19				No detection rms = 0.2			
G24A1				No detection rms = 0.2			
G24A2				No detection rms = 0.3			
G10				No detection rms = 0.1			
				Line E			
G31	220.55216	96.8	95.8	19.0 (22.2)	6.4 (4.4)	2.8 (1.3)	0.9
G29				No detection rms = 0.3			
G19				No detection rms = 0.6			
G10				No detection rms = 0.2			
G24A1				No detection rms = 0.8			
G2A2				No detection rms = 0.8			

† The small spread in frequency (0.0002 – 0.002 GHz) between the rest frequency of the line and the observed frequency for each molecule in each hot core, is due to the difference between the V_{LSR} and the V_{peak} in each hot core. This difference is within the spectral resolution and V_{peak} error of the observations. †† The error for $\int T\,dv$ given in brackets is determined from the fitting error and the calibration uncertainty in the flux measurement of the telescope, as in Section 2.4.2. The error for T_B is also determined as described in Section 2.4.2. The error for the FWHM is the fitting error.

Table 2.5: The observed lines transitions, E_u, $S\mu^2$, and line list used for lines A, B and E.

Line	Molecule	Transition	Frequency (GHz)	E_u (K)	$S\mu^2$ D^2	Hot core detected in
Line A	$HCOOCH_3$ vt=1	18(8,10) – 17(8,9)E	220.25809	331	38.5	G31, G29, G24A1, G24A2
Line B	$HCOOCH_3$ vt=1	18(10,9) – 17(10,8)E	220.30738	354	33.2	G31
Line E	$H^{13}COOCH_3$	18(6,12) – 17(6,11)	220.55130	313	43.9	G31

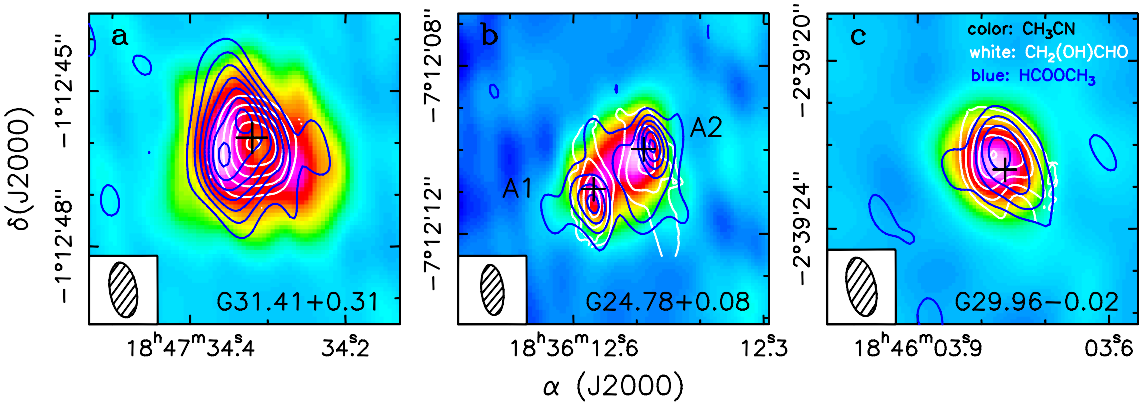

Figure 2.10: Spectral line map of the $18_{8,10} - 17_{8,9}$E transition of methyl formate (blue contours), the $20_{2,18} - 19_{3,17}$ transition of glycolaldehyde (white contours) and the averaged emission of the K=0, 1, 2 (12 – 11) transitions of methyl cyanide emission (colour scale) in G31, G29, G24A1 and G31. For the methyl formate in G31, the channels averaged were 91.7 – 101.9 kms^{-1}, with contour levels of 0.04 – 0.28 Jy beam^{-1}, in steps of 0.04 Jy beam^{-1}. In G24, the channels averaged for methyl formate were 102.4 – 112.6 kms^{-1}, with contour levels of 0.02 – 0.12 Jy beam^{-1}, in steps of 0.02 Jy beam^{-1}. In G29, the channels averaged for methyl formate were 91.1 – 101.3 kms^{-1}, with contour levels of 0.015 – 0.06 Jy beam^{-1}, in steps of 0.015 Jy beam^{-1}. For glycolaldehyde in G31, the channels averaged were 91.9 – 95.3 kms^{-1} with contour levels of 0.10 – 0.46 Jy beam^{-1}, in steps of 0.12 Jy beam^{-1}. In G24, the channels averaged for glycolaldehyde were 104.8 – 108.2 kms^{-1}, with contour levels of 0.04 – 0.12 Jy beam^{-1}, in steps of 0.04 Jy beam^{-1}. In G29, the channels averaged for glycolaldehyde were 92.2 – 95.6 kms^{-1}, with contour levels of 0.016 – 0.08 Jy beam^{-1}, in steps of 0.016 Jy beam^{-1}. For methyl cyanide the contour levels in G31 are 0.1 – 0.94 Jy beam^{-1} in steps of 0.12, in G24, they are 0.1 – 1.0 Jy beam^{-1} in steps of 0.18 Jy beam^{-1}, and in G29, they are 0.09 – 1.14 Jy beam^{-1} in steps of 0.15 Jy beam^{-1}.

– $11_{0,11}$. Methylene amidogen has previously been found in the cold core TMC–1 (Ohishi et al. 1994) and methyl formate and vinyl alcohol have previously been detected in hot cores (Fontani et al. 2007; Turner & Apponi 2001). Using criterion (v) from Section 2.1, methylene amidogen can be ruled out as there are several expected transitions in the frequency range of the observations that are not seen. Vinyl alcohol can also be ruled out because the $11_{2,10}$ – $11_{0,11}$ transition has a low line intensity ($S\mu^2 = 0.03$), which leads to a column density of 2.7×10^{20} cm^{-2}, six orders of magnitude higher than the vinyl alcohol column density in Sagittarius B2(N) (Turner & Apponi 2001) and much larger than those of more commonly–observed molecules. Line A can therefore be identified as the $18_{8,10}$ – $17_{8,9}$E transition of methyl formate, but the $24_{2,23}$ – $24_{1,24}$E, and $24_{2,23}$ – $24_{0,24}$E transitions also contribute to the line A emission. The $18_{8,10}$ – $17_{8,9}$E transition of methyl formate is a high energy transition therefore it was not identified previously.

One notes however that, while all the expected transitions of methyl formate in the

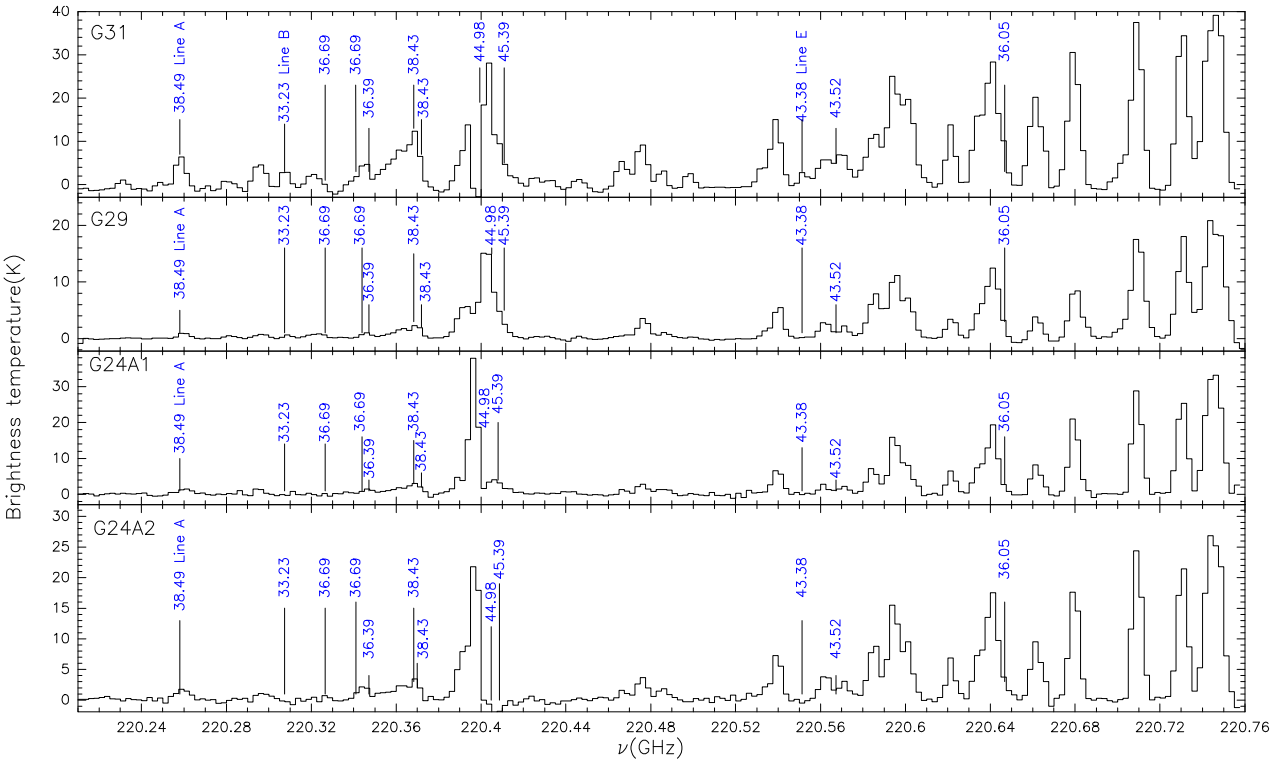

Figure 2.11: The expected bright emission of methyl formate transitions, that occur in the frequency range of the observations, plotted on the spectra of hot cores G31, G29, G24A1 and G24A2. The numbers on the plot represent the intensity ($S\mu^2$) of methyl formate transitions as determined by laboratory studies, in units of Debye^2.

observations frequency range are detected in G31, this is not the case for the other hot cores (see Fig. 2.11). For example, the 220.55131 GHz $18_{6,12}$ – $17_{6,11}$, vt=1 (virbationally-torsionally excited state) transition of methyl formate falls in a region of no detectable emission in the hot cores G29, G24A1 and G24A2. This may be an indication of temperature differences among hot cores as the intensity of methyl formate transitions is significantly temperature dependent.

Line B is only detected in G31 (see Fig. 2.13). Its potential line identities are three transitions of methylene amidogen (H_2CN) and one line of methyl formate ($18_{10,9}$ – $17_{10,8}$E). Methylene amidogen can, again, be ruled out according to (iii) criterion of Section 2.1, so the methyl formate $18_{10,9}$ – $17_{10,8}$E transition is the best candidate for line B.

Line E is only detected in G31 (see Fig. 2.14). The quality of the Gaussian fit was poor and therefore has large errors associated with it. In order to generate a sensible fit

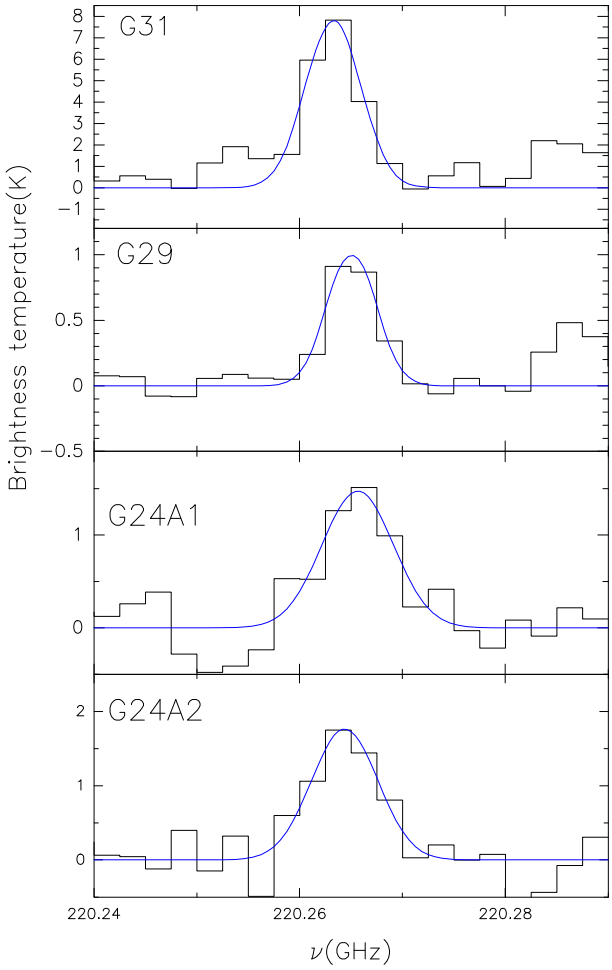

Figure 2.12: Spectra of Line A with Gaussian fits, integrated over the 3σ contour level area towards G31, G29, G24A1 and G24A2 as seen with the PdBI. This transition was previously detected in G31 but was not identified, in Beltrán et al. (2005), and is also detected in G24A1, G24A2 and G29 in this work.

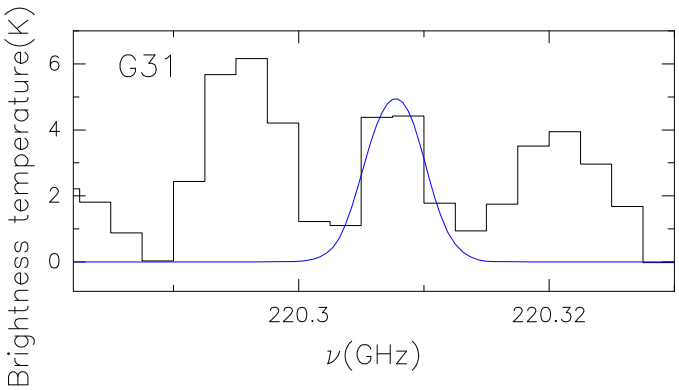

Figure 2.13: Spectra of Line B with a Gaussian fit, integrated over the 3σ contour level area towards G31 as seen with the PdBI. This transition was previously detected in G31 but was not identified in Beltrán et al. (2005).

to the line it was necessary to fix T_{peak} and the line centre for the two molecules (DCO_2H and CH_3CN) blended with this line. The fitting parameters for line E, however, were free.

There are two potential line identities for line E, one line of a carbon–13 isotopologue of methyl formate ($H^{13}COOCH_3$), $18_{6,12}$ – $17_{6,11}$, vt=1 and one line of propanal (CH_3CH_2CHO), $9_{4,5}$ – $8_{2,6}$. There is only one bright line of propanal in the frequency range of these observations. This line falls in an area of little emission in the spectrum of G31 thereby ruling out propanal as a candidate. The $18_{6,12}$ – $17_{6,11}$, vt=1 transition of methyl formate is therefore the best candidate for line E. The transitional information for these newly identified lines can be found in Table 2.5.

2.5 Evolutionary indicators

It is difficult to disentangle the effects of luminosity, mass, and evolutionary stage from the spectra of hot cores alone. As a YSO evolves, the luminosity increases leading to an increase in temperature in the associated hot core and a richer spectra (Beuther et al. 2009). Differences in luminosity and mass between objects at the same stage of evolution, however, will also produce spectral differences. The richness of specific molecules in the spectra may offer a better metric for measuring evolutionary stage. The non–detection of molecules in early High-Mass Protostellar Objects (HMPOs) suggests the formation and excitation of nitrogen-bearing species, such as C_2H_3CN, and C_2H_5CN, take place in an evolutionary more evolved stage (Doty et al. 2002).

Comparing these indicators with our hot core sample we note that G31 has the most chemically rich spectra indicating that it is more evolved than the other cores, however, the luminosity of this core is higher than the other cores (see Table 2.1), and therefore it is difficult to disentangle this effect. G10 has chemically poor spectra despite having the third highest luminosity in our sample, which suggests it is relatively young. Its early–stage is again indicated by the absence of C_2H_3CN, and C_2H_5CN transitions in its spectra, which are observed in the other cores. G24A1 and G24A2 have similar masses but G24A1 is associated with an UCHII region suggesting that it is the more evolved YSO (Beltrán et al. 2005). It is difficult to comment further on the evolution of these objects without

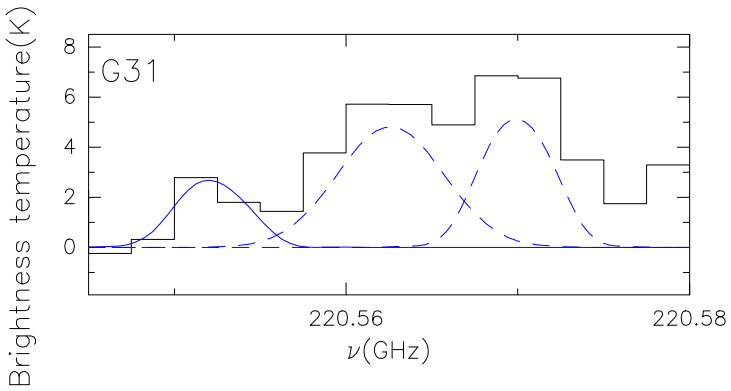

Figure 2.14: Spectra of Line E with a Gaussian fit, integrated over the 3σ contour level area towards G31 as seen with the PdBI. This transition was previously detected in G31 but was not identified in Beltrán et al. (2005).

using a chemical model to understand their chemical history. Such a model is discussed in Chapter 4.

2.6 Conclusions

IRAM PdBI data has been analysed, in the frequency range 220.210 GHz to 220.760 GHz, towards six hot cores: G31.41+0.31, G29.96–0.02, G19.61–0.23, G10.62–0.38, G24.78+0.08A1 and G24.78+0.08A2. The aim was to identify seven lines that were unidentified by Beltrán et al. (2005) in G31 and look for their presence in the other five hot cores, as well as identify other complex molecules that were identified by Beltrán et al. (2005) in G31 and G24 but not in G29, G19 and G10.

New identifications are made of three new transitions of methyl formate ($HCOOCH_3$) in G31, two of which are vibrationally excited lines. The spatial distribution of methyl formate does indicate that it traces the dense and compact parts of hot cores. Comparatively methyl formate traces a region slightly more compact than that of methyl cyanide but glycolaldehyde emission still remains the most compact to date. At this stage it is not clear whether the fact that methyl formate is more extended than glycolaldehyde is a question of excitation or chemistry. In G29, however, methyl formate and glycolaldehyde are tracing an emission region of 0.05 pc which is comparable to the compact emission of glycolaldehyde in G31 (0.08 pc). In G24 methyl formate and glycolaldehyde both trace a

region comparable in size to the region traced by methyl formate in G31.

In this work, a detection of the $20_{2,18} - 19_{3,17}$ transition of glycolaldehyde is postulated in two more hot cores bringing the total number of detections in high mass star forming regions, outside the Galactic Centre, to five hot cores. This emission whilst being far more compact in G31, is of comparable compactness to methyl formate in G24A1, G24A2 and G29. More observations are needed to confirm the presence of glycolaldehyde in these hot cores. The other complex molecule detections in the sample highlight chemical homogeneity among G29, G19, G24A1 and G24A2, not only in terms of presence or absence of certain transitions but also when comparing column densities. G31, however, is the most chemically rich object and the variety of transitions seen may suggest that it represents a different evolutionary stage to the other hot cores in the sample, or it may surround a star with a higher mass. G10 is the most chemically poor hot core in the sample, and combined with the non-detection of C_2H_3CN, and C_2H_5CN transitions seen in the other cores, it indicates that it is at an early–stage of evolution.

In the next chapter the column densities and rotation diagrams are derived, assuming Local Thermodynamic Equilibrium (LTE), for each of the molecules detected in the hot core sample and a qualitative comparison is undertaken.

Chapter 3

Spectral line analysis

By the end of my PhD I could swing a sledgehammer.

Jocelyn Bell Burnell

In order to relate the observationally derived quantities from molecular emission to the physical parameters of hot cores, an understanding of the excitation conditions within the cloud are needed. There are several techniques to interpret the antenna temperature measured by the telescope, and convert this information into column densities and temperatures inside the cloud. The most comprehensive of these is to generate a complete physical model of the cloud and then compute the non-LTE excitation of a molecule, calculate the emerging radiation from the source using non-linear radiative transfer, and then convolve this emission with the telescope beam, to produce a simulated spectrum to compare with observations. This requires collisional rate coefficients, which are not available for most complex molecules. These limitations mean that for the molecules discussed in this thesis, an alternative approach is needed to determine the physical parameters from within the cloud. The alternative is to assume LTE and then compute column densities and temperatures through either the rotation diagram method, or an LTE spectral model comparison with the observations.

The rotation diagram method relates the column density per statistical weight of several molecular energy levels (N_u/g_u), to their energy above the ground state (E_u). If LTE

is assumed and the molecular transitions are optically thin, the column density of the upper level N_u can be related to the integrated intensity by

$$N_u/g_u = \frac{N_{tot}}{Q(T_{rot})} e^{-E_u/T_{rot}} = \left(\frac{8\pi\nu^2 k \int T dv}{hc^3 A g_u} \right), \tag{3.1}$$

where g_u is the statistical weight of the level u, N_{tot} is the total column density of the molecule, $Q(T_{rot})$ is the rotational partition function, E_u is the energy of the upper energy level, T_{rot} is the excitation temperature of the molecular transitions, k is the Boltzmann constant, ν is the frequency of the line transition, A is the Einstein coefficient of the transition, and $\int T dv$ is the integrated line intensity.

In cases where the source does not fill the beam, the column density must be corrected for beam dilution by dividing the integrated line intensity by the beam dilution factor:

$$\eta_{BD} = \frac{\theta_S^2}{\theta_S^2 + \theta_B^2}, \tag{3.2}$$

where θ_S is the source size and θ_B is the beam size.

Equation 3.1 can be used to compute the column density of a molecule using only a single transition, however, a more accurate value is determined if multiple transitions are used. A plot of $\ln(N_u/g_u)$ versus E_u will then be a straight line, with gradient of $-1/T_{rot}$, and y-intercept of $\ln(N_{tot}/Q(T_{rot}))$. If all energy levels are thermalised the excitation or "rotation" temperature is equal to the kinetic temperature of the gas. In cases where the assumption of optical thinness fails it is possible to calculate an optical depth correction factor for linear molecules (Goldsmith & Langer 1999). In the case of non-linear molecules, molecular emission of isotopologues can be used to determine column densities and gas temperatures, however one must account for the ratio of isomers to non isomers (e.g. $^{13}C/^{12}C$) in particular regions, to derive accurate column densities. A full derivation of Equation 3.1, as described by Goldsmith & Langer (1999), can be found in Appendix A.

Alternatively, a comparison between the observational spectra and a spectral model can be performed, to determine the column densities and excitation temperatures. A spectral model simulates how the intensity of a source with intensity I_ν changes with

absorption and emission within a cloud using the equation of radiative transfer:

$$\frac{dI_\nu}{ds} = -\alpha_\nu I_\nu + j_\nu, \tag{3.3}$$

where $\frac{dI_\nu}{ds}$ is the change in intensity at frequency ν, through a slab of material of thickness s, with absorption coefficient α_ν and emissivity j_ν.

The emission from this cloud is then combined with the emission from the cosmic microwave background and its detection at a telescope is simulated, to produce an artificial spectrum. The physical parameters of the cloud (e.g. temperature, column density, cloud size, molecular content) can be varied to produce an artificial spectrum which best fits the observed spectrum, and therefore a column density and excitation temperature which best fits the observed spectra.

In this chapter we analysis the molecular transitions detected in Chapter 2 with both the rotation diagram method and spectral modelling. In Sections 3.1 and 3.2 we use the rotation diagram method to compare column densities and rotation temperatures across the hot cores G31, G29, G19, G24A1, and G24A2. In Section 3.3 we use spectral modelling to confirm the presence of the molecules identified in Chapter 2, and derive column densities and excitation temperatures for the molecular emission, which we compare to the values determined from the rotation diagram method.

3.1 Estimates of excitation temperature

Methyl formate in G31 has been extensively studied and, aside from three newly–identified transitions, twenty–six transitions have been previously detected (Fontani et al. 2007) using the IRAM–30m. We therefore use the twenty–nine lines of methyl formate in G31 to derive column densities and temperature estimates using a rotational diagram. We have accounted for the beam dilution of the IRAM–30 m data using a source size of $3\farcs5$ as measured from the spectral line map of methyl formate (Fig. 2.10). For the newly identified transitions we assume their emission fills the beam. The results can be seen from Fig. 3.1 and Table 3.1. The linear fits to the data in Fig. 3.1 have been calculated using a weighted regression line. The derived column density (Table 3.1) is in good agreement with the results of Isokoski et al. (2013 , $1.7 \times 10^{17}\,\mathrm{cm}^{-2}$) when assuming a source size of $3\farcs5$.

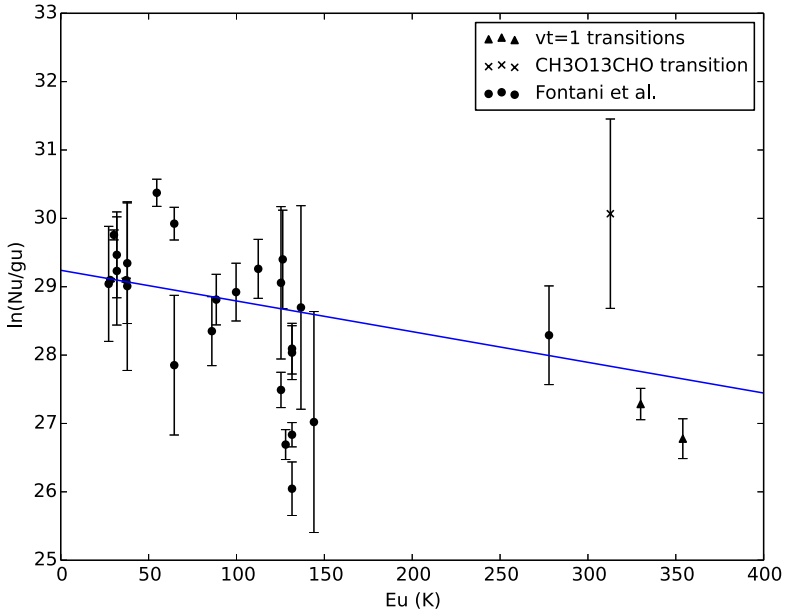

Figure 3.1: A rotation diagram of methyl formate transitions in G31, extending the work of Fontani et al. (2007) to higher excitation temperatures. A $^{12}C/^{13}C$ ratio of 41 was calculated according to Wilson & Rood (1994) using the Galactic Coordinates of G31 and a source size of 3.″5 was assumed based on the observed distribution seen in Fig. 2.10. Errors for the v=1 excited transitions are so small (<0.02) that they do not appear on this diagram.

Table 3.1: Estimated rotational temperature and column density of methyl formate calculated using the rotation diagram method, using a source size which has been measured in Chapter 2.

Object	Source size (″)	$T_{\rm rot}$ (K)	Column density ($\rm cm^{-2}$)
G31	3.5	223±25	$6.06\pm0.03\times10^{17}$

From the rotational diagram we find that, surprisingly, a single gas component with a temperature of ∼223 K can fit all twenty nine transitions. Note that line A and line B are vibrationally excited transitions of methyl formate and we would have expected them to trace a hotter region of gas. The large scatter of data points may indicate that this single component does not characterise the kinetic temperature of the gas. Such a scatter could be seen if the assumptions of LTE and optical thinness fail. Once a transition has become optically thick, N_u/g_u, from equation 3.1, does not increase when the fractional abundance of a species increases (Goldsmith & Langer 1999). If a mixture of optically thin and thick transitions are included on the rotation diagram, a large scatter of data points is seen. Additionally, such a scatter may indicate different degrees of sub–thermal excitation, i.e. non–LTE excitation (Goldsmith & Langer 1999). Finally, multiple temperature components could be present which would make any linear fit to the data very poor. In this instance, however, one would expect to observe a curve in the rotation diagram, rather than a large scatter of data. Considering the large errors seen on several of the Fontani et al. (2007) data points, and the lack of data points in the 150 – 270 K upper energy level range, it is difficult to characterise this scatter further, and more observations are required.

3.2 Column density estimates

Table 3.2 lists calculated column densities for all identified molecules across our sample, derived using Equation 3.1, by assuming LTE and optically thin emission (see Section 3.1 for a detailed discussion of the temperature of our hot cores). For CH_3CN, and $HCOOCH_3$ in G31, column densities have been derived from the rotation diagram method and are therefore computed at their rotation temperature, given in brackets. For CH_2OHCHO in G31 the column density was derived by Beltrán et al. (2009), but they were unable to determine a rotation temperature, and a kinetic temperature of 300 K is assumed. For molecules where only a single transition has been detected, and therefore no rotation temperature can be derived, the column densities are computed at 300, 225, and 150 K.

For the IRAM–30m observations of G31 we use a beam size ranging from $10'' - 24\farcs4$. For the PdBI observations we assume the source fills the beam.

Table 3.2 shows that all our species peak in their density in G31. However, it is surprising that there is relatively little variation across the sample for HNCO, DCO_2H, C_2H_3CN

Table 3.2: Column densities (cm^{-2}) of the organic molecules in our sample, assuming LTE and optical thinness. The associated error for each column density is in brackets. For molecules where only a single transition has been detected the column densities are computed at 300, 225, and 150 K. For molecules where a rotation temperature is known, the column densities are computed at that temperature.

Object	C_2H_3CN	DCO_2H	HNCO	C_2H_5CN
		300 K		
G31	1.47 (0.61)×10^{18}	5.00 (0.46)×10^{16}	3.69 (0.39)×10^{16}	1.56 (0.42)×10^{16}
G29	...	1.61 (0.40)×10^{16}	1.80 (0.25)×10^{16}	2.25 (0.65)×10^{15}
G19	2.87 (0.60)×10^{17}	1.28 (0.41)×10^{16}	2.02 (0.22)×10^{16}	4.69 (0.36)×10^{15}
G24A1	2.90 (0.73)×10^{17}	...	1.43 (0.51)×10^{16}	5.26 (0.39)×10^{15}
G24A2	7.27 (0.44)×10^{17}	1.60 (0.71)×10^{16}	1.75 (0.43)×10^{16}	6.38 (0.43)×10^{15}
		225 K		
G31	8.38 (0.61)×10^{17}	3.25 (0.46)×10^{16}	2.43 (0.39)×10^{16}	1.01 (0.42)×10^{16}
G29	...	1.05 (0.40)×10^{16}	1.18 (0.25)×10^{16}	1.46 (0.65)×10^{15}
G19	1.64 (0.60)×10^{17}	8.34 (0.41)×10^{15}	1.33 (0.22)×10^{16}	3.04 (0.36)×10^{15}
G24A1	1.66 (0.73)×10^{17}	...	9.44 (0.51)×10^{15}	3.42 (0.39)×10^{15}
G24A2	4.15 (0.44)×10^{17}	1.04 (0.71)×10^{16}	1.15 (0.43)×10^{16}	4.14 (0.43)×10^{15}
		150 K		
G31	3.90 (0.61)×10^{17}	1.77 (0.46)×10^{16}	1.33 (0.39)×10^{16}	5.52 (0.42)×10^{15}
G29	...	5.69 (0.06)×10^{15}	6.48 (0.25)×10^{15}	7.95 (0.65)×10^{14}
G19	7.62 (0.60)×10^{16}	4.54 (0.41)×10^{15}	7.25 (0.22)×10^{15}	1.65 (0.36)×10^{15}
G24A1	7.71 (0.73)×10^{16}	...	5.16 (0.51)×10^{15}	1.86 (0.39)×10^{15}
G24A2	1.93 (0.44)×10^{17}	5.67 (0.71)×10^{15}	6.31 (0.43)×10^{15}	2.25 (0.43)×10^{15}

Object	CH_3CN[a]	$CH_2(OH)CHO$	$HCOOCH_3$
G31	8×10^{16} (164 K)	1×10^{17}[††] (300 K)	6.06 (0.03)×10^{17}[†††] (223 K)
G29	1×10^{16} (158 K)	5.14 (0.66)×10^{15} (300 K)	1.62 (0.32)×10^{16} (300 K)
G19	2×10^{16} (244 K)	4.59 (0.62)×10^{15} (300 K)	...
G24A1	2×10^{16} (132 K)	3.95 (0.40)×10^{15} (300 K)	3.42 (0.48)×10^{16} (300 K)
G24A2	2×10^{16} (132 K)	8.14 (0.49)×10^{15} (300 K)	3.80 (0.41)×10^{16} (300 K)
G31	...	...	...
G29	...	2.83 (0.66)×10^{15} (225 K)	9.84 (0.32)×10^{15} (225 K)
G19	...	2.52 (0.62)×10^{15} (225 K)	...
G24A1	...	2.17 (0.40)×10^{15} (225 K)	2.07 (0.48)×10^{16} (225 K)
G24A2	...	4.48 (0.49)×10^{15} (225 K)	2.31 (0.41)×10^{16} (225 K)
G31	...	...	...
G29	...	1.23 (0.66)×10^{15} (150 K)	4.80 (0.32)×10^{15} (150 K)
G19	...	1.09 (0.62)×10^{15} (150 K)	...
G24A1	...	9.43 (0.40)×10^{14} (150 K)	1.01 (0.48)×10^{16} (150 K)
G24A2	...	1.94 (0.49)×10^{15} (150 K)	1.13 (0.41)×10^{16} (150 K)

[a] CH_3CN has been observed to be optically thick in all these objects so the column densities are those derived by (Beltrán et al. 2005, 2011) using observations of $CH_3{}^{13}CN$. Column density errors for this molecule are not given in these papers.

[††] The column density of glycolaldehyde for G31 has been obtained by Beltrán et al. (2009) using the rotation diagram method, assuming a kinetic temperature of 300 K.

[†††] The column density for this object was determined using the rotation diagram method assuming a source size of 3.″5, see Section 3.1.

and C_2H_5CN, all of which differ by a factor of 5 or less from source to source, especially when considering the variation in luminosity in the sample (see Table 2.1). HNCO densities are remarkably consistent throughout the sample. CH_3CN and $CH_2(OH)CHO$ show more variation, but if we exclude G31, then calculated column densities for the remaining objects in the sample again agree very well, to within a factor of $\sim$2. It is difficult to disentangle the effects of luminosity and chemical evolution, to explain the large column densities observed in G31. The differences between the luminosity of G31 and the other hot cores, however, is not sufficient to explain the chemical variations observed suggesting the cores are not all at the same stage of evolution.

3.3 Spectral Modelling

We have also analysed the observations using the spectral modelling software CASSIS and using the JPL Catalog. CASSIS has been developed by IRAP-UPS/CNRS [1]. We use the LTE analysis tool to determine the column densities and excitation temperatures, T_{ex}, required to reproduce the emission. The brightness temperature, T_b, of a given species is calculated by CASSIS according to:

$$T_b = T_C e^{-\tau} + (1 - e^{-\tau})(J_\nu(T_{ex}) - J_\nu(CMB)), \tag{3.4}$$

where T_C is the temperature of the continuum, τ is the optical depth, CMB is the cosmic microwave background at 2.7 K, and $J_\nu(T) = (h\nu/k)/(1-e^{h\nu/kT}-1)$ is the radiation temperature. A derivation of this formula using the equation of radiative transfer (Equation 3.3) can be found in Vastel (2014).

The input parameters for CASSIS are the column density, excitation temperature, source size, FWHM, and V_{LSR} for each species we observe. Values for the source size, FWHM, and V_{LSR} are taken from our observations. We vary the column densities and excitation temperatures for each species until a best fit is achieved. Further details of the CASSIS software and LTE analysis tool can found in the CASSIS documentation[2].

In particular, the spectral modelling focuses on the emission of CH_3CN, $HCOOCH_3$

[1] http://cassis.irap.omp.eu
[2] http://cassis.irap.omp.eu/docs/RadiativeTransfer.pdf

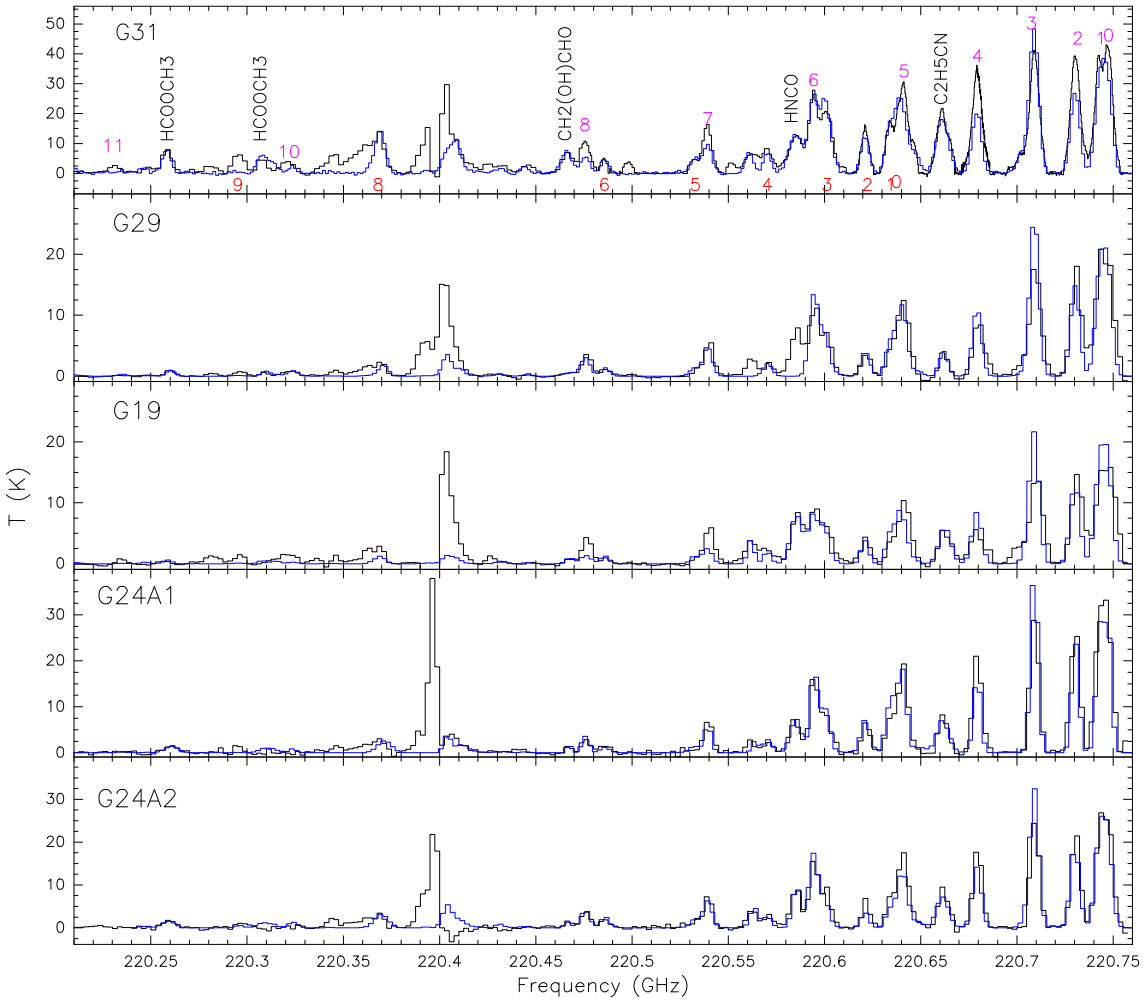

Figure 3.2: CASSIS modelling (blue line) of methyl formate ($HCOOCH_3$), glycolaldehyde ($CH_2(OH)CHO$), methyl cyanide (CH_3CN), isocyanic acid (HNCO), and ethyl cyanide (C_2H_5CN) overlaid on the PdBI observations (black line). We label the molecules detected in this work in the G31 panel. The numbers indicate the position of the CH_3CN (12_K – 11_K) K-components in the upper part (in pink) of each spectra and of the CH_3 ^{13}CN (12_K – 11_K) K-components in the lower part (in red). We exclude the ^{13}CO line from these models as several of the line profiles exhibit missing flux from the centre, mostly likely due to extended emission being filtered out by the interferometer citepbeltran2005.

and a possible contamination of the $CH_2(OH)CHO$ emission with $(CH_3)_2CO$, to test the validity of our line assignments. In this model, we assume that the gas is in LTE conditions at a temperature T_{ex}. We exclude the ^{13}CO line from these models as several of the line profiles exhibit missing flux from the centre, mostly likely due to extended emission being filtered out by the interferometer (Beltrán et al. 2005). A comparison of the column densities that we derive using the rotation diagram method and those we derive from spectral modelling can be found in Table 3.3.

Spectral models of CH_3CN emission, using only a single column density and excitation temperature, do not reproduce the observations accurately (Figure 3.2). We hypothesize that this 'poor' fit may be due to a combination of factors: (i) different transitions of CH_3CN may peak, or may be tracing, different temperatures and densities within our emission region, (ii) the emission we observe may not be in LTE, (iii) contributions due to blending, (iv) CH_3CN opacities are highly variable from the K=1 to the K=7 transitions, (v) the poor signal-noise ratio of the high–energy K-transitions. The best fit of all of the CH_3CN transitions is achieved at T_{ex} ranging from $410-450$ K across our hot core sample. For $HCOOCH_3$ emission we have produced a spectral fit for the transition at 220.258 GHz (Figure 3.3) and the transition at 220.307 GHz. We are unable to model any isotopologues of methyl formate with CASSIS and have therefore omitted the transition at 220.551 GHz from our fit. In G31, where the rotation diagram column density was derived from multiple transitions of methyl formate, we find the spectral model column density required to match the observations to be the same order of magnitude as the value derived from the rotation diagram method (6.06×10^{17} cm^{-2}). For the other hot cores we require a modelled column density a factor of $2-3$ larger than the rotation diagram value. This is not surprising as the rotation diagram column density was derived from only one transition in these cores and therefore represents a less reliable estimate of the methyl formate column density in these objects. As we only have one confirmed methyl formate transition in several of our hot cores, it is difficult to accurately measure the T_{ex} required to reproduce these observations. We are confident from this modelling that we have correctly identified the $18_{8,10}-17_{8,9}$E and $18_{10,9}-17_{10,8}$E transitions of $HCOOCH_3$ in our hot core sample.

For $CH_2(OH)CHO$ emission we have produced a spectral fit for the transition at 220.466 GHz (Figure 3.4). For G31 the required column density to reproduce the spectra

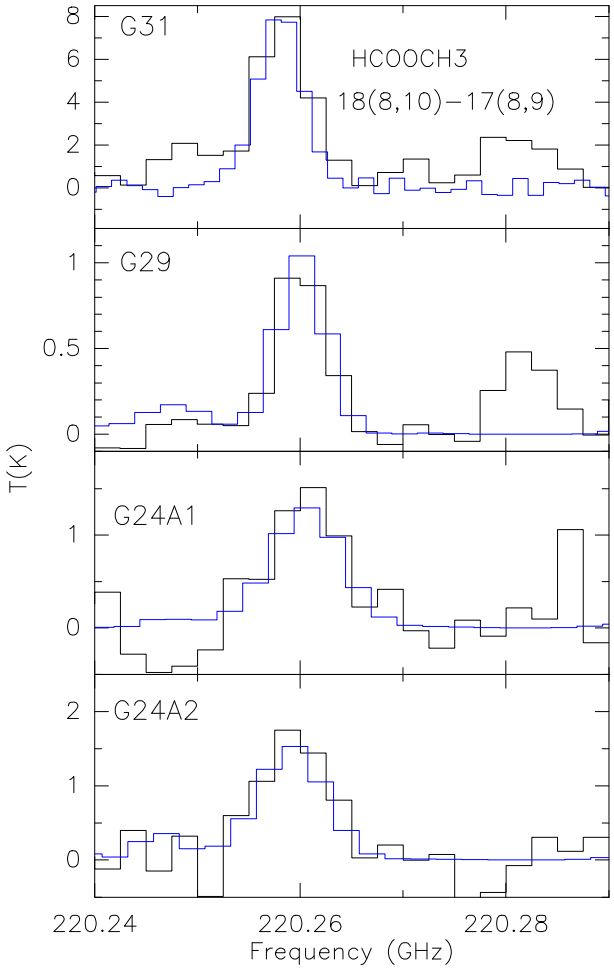

Figure 3.3: Models of the $18_{8,10}-17_{8,9}$E transition of $HCOOCH_3$ using CASSIS (blue line) overlaid on the PdBI observations (black line).

is similar to the observed value. For G29, G19, G24A1, and G24A2 the required model column densities are a factor of 1.5 – 3 larger than the observed values. This is likely to be due, again, to the rotation diagram column densities for these hot cores being derived using only one CH_2(OH)CHO transition, and therefore represent a less reliable estimate of the column densities.

We have also explored the possibility that this transition of glycolaldehyde is blended with the $46_{20,26}-46_{19,27}$ EE (E_u = 816 K, $S\mu^2$ = 2843 D^2) and the $11_{11,1,1}-10_{10,0,1}$AE (E_u = 63 K, $S\mu^2$ = 519 D^2) transitions of acetone. We find for column densities and excitation temperatures of acetone which produce enough emission to explain the line at 220.466 GHz, we overproduce emission at 220.368 GHz. It is possible that both acetone and glycolaldehyde could be present in the hot cores in our sample, however, the contribu-

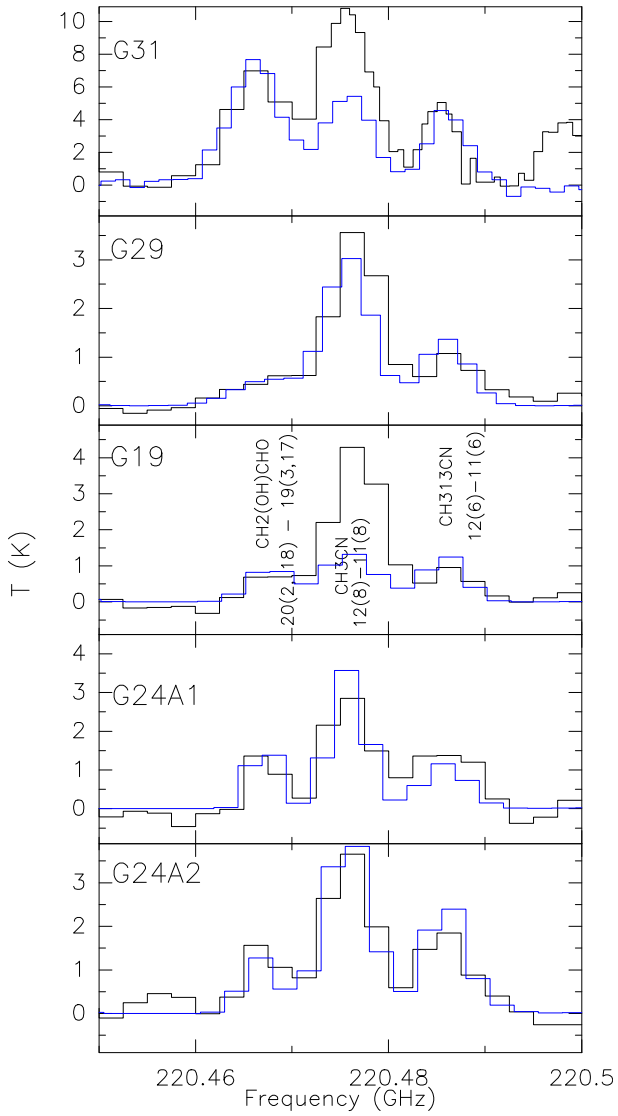

Figure 3.4: $CH_2(OH)CHO$ spectra with CASSIS models (blue line) overlaid on the PdBI observations (black line). From left to right: the $20_{2,18} - 19_{3,17}$ transition of glycolaldehyde, the $12(8) - 11(8)$ transition of CH_3CN, and the $12(6) - 11(6)$ transition of $CH_3{}^{13}CN$.

Table 3.3: A comparison table between spectral modelling column densities (CD) and excitation temperatures, and column densities (CD) derived using the rotation diagram (RD) method at specific temperatures, for methyl cyanide, methyl formate and glycolaldehyde.

Hot core	T_{ex} (K)	Spectrally modelled CD (cm^{-2})	CD derived using RD method (cm^{-2})
		CH_3CN	
G31	450	9×10^{15}	$8\times10^{16\dagger}$ (164 K)
G29	410	5×10^{15}	$1\times10^{16\dagger}$ (158 K)
G19	450	4×10^{15}	$2\times10^{16\dagger}$ (244 K)
G24a1	310	4×10^{15}	$2\times10^{16\dagger}$ (132 K)
G24a2	450	6×10^{15}	$2\times10^{16\dagger}$ (132 K)
		$HCOOCH_3$	
G31	223	3.31×10^{17}	6.06×10^{17} (150 K)
G29	300	4.30×10^{16}	1.62×10^{16} (300 K)
G24A1	300	9.60×10^{16}	3.42×10^{16} (300 K)
G24A2	300	1.00×10^{17}	3.80×10^{16} (300 K)
		$CH_2(OH)CHO$	
G31	300	8.20×10^{16}	1.00×10^{17} (300 K)
G29	300	8.00×10^{15}	5.14×10^{15} (300 K)
G19	300	9.00×10^{15}	4.59×10^{15} (300 K)
G24A1	300	1.00×10^{16}	3.95×10^{15} (300 K)
G24A2	300	1.00×10^{16}	8.14×10^{15} (300 K)

† These values are taken from Beltrán et al. (2005) and are therefore quoted to the same precision given in this paper.

tion of acetone to the line seen at 220.466 GHz is not significant (<7%). More observations are needed to confirm the presence of both glycolaldehyde and acetone in these hot cores.

3.4 Conclusions

A rotation diagram analysis of methyl formate emission in G31 yields a column density of 6.06×10^{17} cm^{-2}. This is at least one order of magnitude larger than the column densities in the other hot cores in our sample. We have also found a single temperature component of 223 K (using a source size of $3\farcs5$) that fits these transitions, although the vibrationally excited transitions we have found, and our very large column densities would suggest that methyl formate may trace multiple temperature components of G31. This may also be true of the hot cores in G29 and G24. The spatial distribution of methyl formate does indicate that it traces the dense and compact parts of hot cores. Spectral modelling of methyl formate produces the same column density in G31 as determined by the rotation diagram method. In the other cores we find that the differences between column densities determined through spectral modelling and through the rotation diagram method are less

than an order of magnitude. This is to be expected when the column density is only computed for a single transition.

In Chapter 2 we postulate that we have found the $20_{2,18} - 19_{3,17}$ transition of glycolaldehyde in two more hot cores bringing the total number of detections in high mass star forming regions, outside the Galactic Centre, to five hot cores. We have spectrally modelled our emission to explore the possible contamination of this transition with the $46_{20,26} - 46_{19,27}$ EE and $11_{11,1,1} - 10_{10,0,1}$AE transitions of acetone. We find that any contribution of acetone emission to the line seen at 220.466 GHz is not significant. More observations are needed to confirm the presence of glycolaldehyde in these hot cores. Our other complex molecule detections in our sample highlight chemical homogeneity among G29, G19, G24A1, and G24A2, not only in terms of presence or absence of certain transitions but also when comparing column densities. G31, however, is the most chemically rich object, and the significantly different column densities we find in this core combined with the variety of transitions seen may suggest that it represents a different evolutionary stage to the other hot cores in our sample, or it may surround a star with a higher mass.

Chapter 4

Chemical Modelling

It is a mistake to think you can solve any major problems just with potatoes.

Douglas Adams

In Chapter 3, we found a chemical difference between G31 and rest of our hot core sample. Chemical differentiation in hot cores has been observed before (Mookerjea et al. 2007; Garay & Lizano 1999) and attributed to either differences in their host star mass and/or differences in ages. Results of chemical models in the past have suggested that determining abundance ratios of typical hot core tracers (e.g. CH_3CN) as well as sulphur–bearing species could serve as indicators of both mass and age (Hatchell et al. 1998; Viti et al. 2001; Buckle & Fuller 2003; Viti et al. 2004). However, much care has to be taken due to the fact that most species do not necessarily trace the very inner part of the core and their emission region probably spans a range of densities and temperatures that make the interpretation difficult (Wakelam et al. 2004). The complex species discussed in Chapters 2 and 3, on the other hand, may be a better choice of age/mass discrimination as they all seem to trace a more compact region than the more widely–observed species such as CH_3OH and CH_3CN.

In the next section we make use of a chemical model, UCL_CHEM (Viti et al. 2004) to simulate the formation and evolution of hot cores and see if the differences in ratios of the species listed in Table 3.2, between G31 and the rest of the cores, can shed some light on the masses and ages of our sources.

4.1 UCL_CHEM

UCL_CHEM (Viti et al. 2004) is a two–phase time–dependent gas–grain model, which follows the collapse of a pre–stellar core (Phase I), followed by the subsequent warming and evaporation of grain mantles (Phase II). Phase I starts from the number density of a diffuse cloud (10^2 cm^{-3}) and allows a free–fall collapse to take place until a final density (which varies between 10^{6-8} cm^{-3}) is reached. This occurs isothermally at a temperature of 10 K. During the collapse, atoms and molecules collide with, and freeze on to, grain surfaces. The depletion efficiency is determined by the fraction of the gas–phase material that is frozen on to the grains (Rawlings et al. 1992). This fraction is arrived at by adjusting the grain surface area per unit volume, and assuming a sticking probability of unity for all species. The fraction of material on grains is then dependent on the product of the sticking probability and the amount of cross–section provided per unit volume by the adopted grain size distribution. Grains are considered to be spheres. We assume that hydrogenation occurs rapidly on the grain surfaces, so that, for example, some percentage of carbon atoms accreting will rapidly become frozen out methane (CH_4) etc. In Phase II we increase the dust and gas temperature up to 300 K, to simulate the presence of a nearby infrared source, i.e the nearby forming star 'switching on'. The observational luminosity profile of Molinari et al. (2000) is used to derive the temperature of the gas (which is assumed to be the same as the dust temperature), as a function of the luminosity of the protostar. It is assumed that the rise in stellar intensity is too slow to be considered instantaneous and therefore grain surface evaporation is time–dependent. Temperature programmed desorption (TPD) experiments by Collings et al. (2004) on a variety of ices found that all species relevant to hot cores can be categorised as H_2O like (Fraser et al. 2001), CO–like (Collings et al. 2003*b*), and intermediate. Two additional categories, reactive and refractory, were proposed by Viti et al. (2004) to account for species not yet studied with TPD. For each category they used the information in Collings et al. (2004), Collings et al. (2003*b*) and Collings et al. (2003*a*) to estimate the fraction of a particular species that is desorbed in various temperature bands. The specific details for each category including desorption band, species, and fraction desorbed in each band can be found in Table 1 in Viti et al. (2004). This form of time–dependent desorption is included in the warm–up phase of UCL_CHEM.

Initial atomic abundances are taken from Sofia & Meyer (2001) and can be found in

Table 4.1: Initial fractional abundances compared to the total number of hydrogen nuclei, as taken from Sofia & Meyer (2001).

Element	Fractional abundance
He	0.075
N	8.52×10^{-5}
O	4.45×10^{-4}
C	1.79×10^{-4}
Si	1.43×10^{-6}
S	1.48×10^{-6}
Mg	5.12×10^{-6}

Table 4.1.

We use a chemical network which includes 2453 gas phase and grain surface reactions, for 228 different species. For the gas–phase chemistry, reaction rate coefficients are taken from the UMIST database (Woodall et al. 2007). Some coefficients have been updated with those from the KInetic Database for Astrochemistry (KIDA) database (Wakelam et al. 2009). Some simple grain–surface reactions (mainly hydrogenation) are also included, as in Viti et al. (2004). For this work we have also included selected routes for grain–surface formation of glycolaldehyde as in Woods et al. (2012) and methyl formate as in Occhiogrosso et al. (2011). In Phase I three mechanisms of non–thermal desorption are considered as in Roberts et al. (2007): Desorption resulting from H_2 formation, desorption by direct cosmic ray heating, and cosmic ray–induced photo–desorption. Laboratory experiments on graphite substrates suggest that a non–negligible fraction (Creighan et al. 2006) of the ∼4.5 eV released in the exothermic surface formation of H_2 is transferred to the grain surface. This may thermally desorb weakly bound mantle species (Duley & Williams 1993). Considerations of the energy threshold required and the range of volatile species affected can be found in Roberts et al. (2007). The rate of desorption by direct cosmic ray heating is calculated by considering the number of molecules capable of being desorbed per cosmic ray impact. As with H_2 formation, this process is expected to only affect volatile species, e.g. CO. Prasad & Tarafdar (1983) found that cosmic ray particles or secondary electrons released by cosmic ray ionisation may excite the absorbing gas in a molecular core, and result in a significant level of UV photon flux inside dark clouds. The UV photons are most likely absorbed by H_2O leading to dissociation and local heating, resulting in the desorption of nearby molecules.

We use this model to investigate how varying key model parameters, such as the final

Table 4.2: The range of final densites, efficiencies of freeze-out, and masses of the star varied in the 84 models we have run.

Final density (cm^{-3})	Efficiency of freeze-out (%)	Mass
10^6	14 – 62	$15\,M_\odot$, $25\,M_\odot$
10^7	56 – 100	$15\,M_\odot$, $25\,M_\odot$
10^8	100	$15\,M_\odot$, $25\,M_\odot$

collapse density, lifetime of the cold phase, the type of evaporation, and the efficiency of the freeze–out of species (measured as a percentage of the total CO in the solid phase) affect the abundances of methyl cyanide, methyl formate, glycolaldehyde, ethyl cyanide and isocyanic acid during the hot core evolution. We do not include deuterated formic acid in our reaction network because a full deuterated network would have been required. Before this work, this species had only ever been detected in G31 (Beltrán et al. 2005) and very little is known, experimentally, about its formation and destruction in the ISM. We have run 84 models using the range of final densities, efficiencies of freeze-out, and mass of the forming star listed in Table 4.2.

Since the period in which the grains are warmed from very low temperatures to the temperatures observed in typical hot cores is determined by the time taken for a pre–stellar core to evolve towards the main sequence, and hence by its mass (Viti & Williams 1999) we have explored the effect of new–born stars with different masses ($15\,M_\odot$ and $25\,M_\odot$), corresponding to contraction times of 118,000 yr and 70,000 yr respectively – see Bernasconi & Maeder (1996).

In the following section we explore the sensitivity of the aforementioned species to changes in the physical and chemical parameters described above, before comparing our theoretical models with observations. Figures 4.1 – 4.3 show gas–phase abundances in Phase II of the model, for ease of comparison to observationally–derived results.

4.2 Sensitivity to stellar masses

Figure 4.1 shows an example of two models, each with a final density at the end of Phase I of $10^7\,cm^{-3}$ and a freeze–out percentage of ≈60% in the solid phase, differing in the final mass of the star in Phase II. At $\approx 10^{4.5}$ yrs the sudden jump in abundance of methyl formate and ethyl cyanide is due to the evaporation of these species from the grain mantle surface. At late times varying the final mass of the star does not seem to affect the

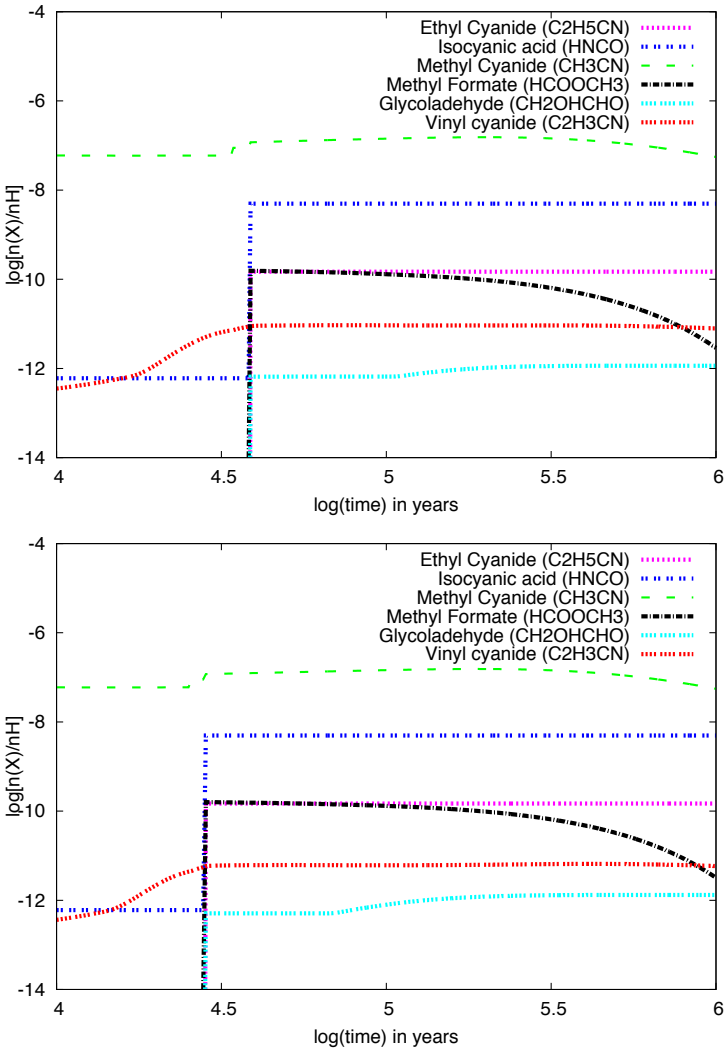

Figure 4.1: Gas phase fractional abundances of selected species as a function of time for a $15\,M_{\odot}$ (top) and a $25\,M_{\odot}$ star (bottom), both with a final gas density after Phase II of $10^7\,cm^{-3}$. At $\approx 10^{4.5}$ yrs the sudden jump in abundance of methyl formate and ethyl cyanide is due to the evaporation of these species from the grain mantle surface.

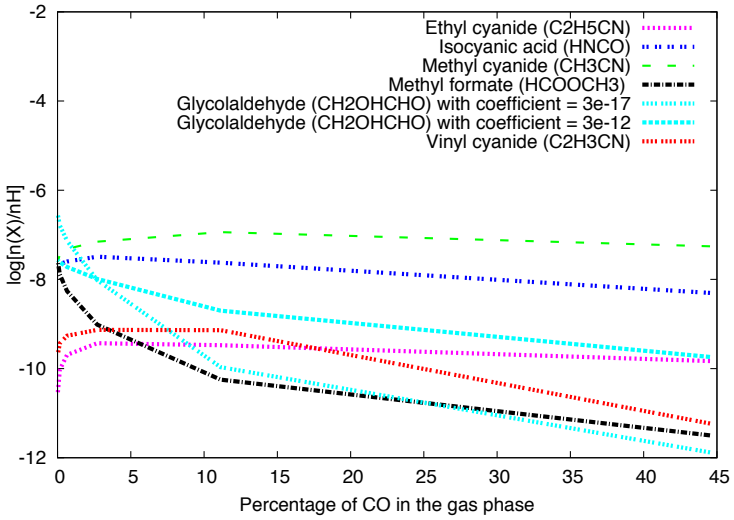

Figure 4.2: Fractional abundances of selected species at 10^6 yr after the 'switch on' of the star as a function of the percentage of CO left in the gas phase at the end of Phase I, for a $25\,M_\odot$ star with a final gas density after Phase I of $10^7\,cm^{-3}$.

fractional abundances of the complex species we consider; however, as expected (see Viti et al. 2004), a higher mass implies an earlier icy mantle evaporation. In general a very low abundance of COMs (complex organic molecules) implies a young age with the exception of methyl cyanide (but see Sect. 4.4) whose abundance is high regardless of the age of the core; hence, a core where this species is the *only* abundant complex molecule may be a very young core. The theoretical low fractional abundances before evaporation translate into column densities of the order of $<10^{10}\,cm^{-2}$, much lower than the lowest observed values for our sample.

4.3 Sensitivity to the icy mantle composition

Figure 4.2 is a plot of the fractional abundances of selected species at 10^5 yr after Phase II starts, as a function of the percentage of CO left in the gas phase at the end of Phase I. Note that after few thousand years from the beginning of Phase II CO will have completely evaporated back into the gas phase so the percentage on the x–axis is *not* an indication of the final gas CO abundance. In the figure, we present models which use two different values of the reaction rate coefficient for the formation of glycolaldehyde. This is due to the uncertainties in the value of this quantity (see Woods et al. 2012). We only consider one formation route for glycolaldehyde for simplicity: g–CH_3OH + g–

HCO → g–CH_2(OH)CHO, where g– refers to a species which is frozen on to the grain surface. As expected, the abundance of most complex species increases with an increase in freeze–out efficiency (corresponding to a decrease in the percentage of CO in the gas phase). However, it is interesting to note that ethyl cyanide seems to decrease at a very high freeze-out efficiency while the abundance of methyl cyanide is more or less constant. The main route of formation for ethyl cyanide is via hydrogenation of HC_3N on the grains so in principle its abundance should increase with the efficiency of freeze–out. However, as HC_3N is efficiently formed in the gas phase via reactions involving H_2O, HCN and other hydrocarbons, when freeze–out is very efficient, the reactants are depleted from gas deposited on the grains at a higher efficiency than that of the reactions forming HC_3N.

4.4 Sensitivity to the gas density

Figure 4.3 shows the abundance of our selected molecules as a function of time for three different final densities. The fractional abundance of most species increases with density when going from 10^6 to 10^7 cm^{-3} although the increase is less pronounced at high densities. An interesting effect of increasing densities is observed with methyl cyanide whose abundance before thermal evaporation is still high at the lowest density, while it drops considerably at high densities: we interpret this as a direct effect of freeze–out, which is directly proportional to collisional frequency of the parent species forming CH_3CN during Phase I. Finally, we note that at a late stage of the evolution of the core, the ratio of the selected COMs varies as a function of density: for example, at lower densities CH_3CN is always higher than the other organic molecules, while already at 10^7 cm^{-3} CH_3CN/C_2H_5CN is $\sim$1 and at higher densities, $<$1. We also see that at lower densities C_2H_3CN/C_2H_5CN $>$1, however, at higher densities this ratio is inverted. Similar considerations can be made about other species, making the ratios of our selected COMs ideal tracers of densities for evolved hot cores.

4.5 Comparison with observations

Table 3.2 shows that the differences in column densities among cores, for most species, are seldom larger than one order of magnitude. We note that of the species we are modelling, only methyl formate and methyl cyanide have been extensively studied in the laboratory (Modica & Palumbo 2010; Bennett & Kaiser 2007; Khlifi et al. 1996; Defrees

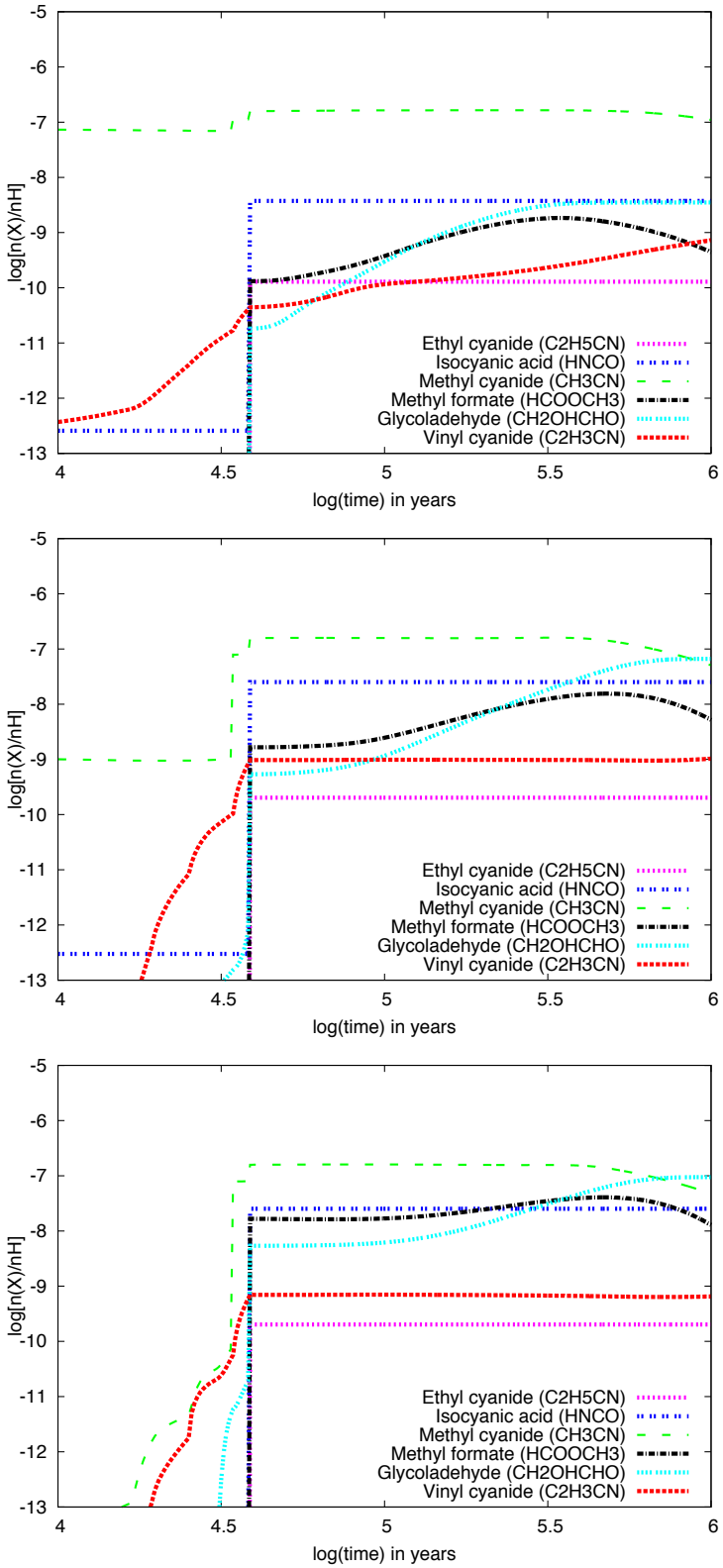

Figure 4.3: The gas phase abundance of isocyanic acid, ethyl cyanide, methyl cyanide, methyl formate, and glycolaldehyde as a function of time for the percentage of CO left in the solid phase of 100% , a mass of 15 $M_{\odot}$, equivalent to a contraction time of 115 000 yr, with step evaporation of the icy mantles. The top panel corresponds to a final density after Phase I of 10^6 cm^{-3}. The middle panel corresponds to a final density after Phase I of 10^7 cm^{-3}. The bottom panel corresponds to a final density after Phase I of 10^8 cm^{-3}.

et al. 1985; Huntress & Mitchell 1979). The other complex molecules are little–known and it is very likely that our models are missing routes of formation and destruction for these species. Moreover, we note that the LTE calculations shown in Table 3.2 were for a temperature of 300 K; a lower temperature would in general yield a lower column density. The uncertainties related to the size of the emission region and temperatures, together with the incompleteness of the chemical networks for COMs makes a quantitive comparison with chemical modelling difficult. Nevertheless, we do attempt a qualitative comparison with observations by estimating theoretical column densities from our models. We derive the theoretical column density of the organic species detected in our hot core sample N, by using the approximate formula below:

$$N = X \times A_{\rm V} \times {\rm N}_{H2}, \tag{4.1}$$

where X is the fractional abundance from our models and $\rm N_{H2}$ is the column density of $\rm H_2$ that corresponds to 1 mag of visual extinction (Bohlin et al. 1978), which is $1.6{\times}10^{21}$ $\rm cm^{-2}$. For $A_{\rm V}$ we adopt a typical hot core visual extinction of 600 mag (noting that the column density simply scales linearly with extinction and that the fractional abundances calculated from the models are insensitive to visual extinctions above a critical value of $\sim$10 mag, when photons do not penetrate any further).

The first general conclusion we can draw by comparing Table 3.2 with our models (see Figs. 4.1, 4.2 and 4.3) is that all cores are evolved enough that all the mantles have evaporated. From our models this means that they are at least 20,000 yr old cores (this estimate increases with decreasing mass).

We find that in most models the theoretical column densities of HNCO do not vary by more than one magnitude ($8{\times}10^{15}$ – $3{\times}10^{16}$ $\rm cm^{-2}$), where the upper values coincide with models with a high density and freeze-out (as expected since HNCO forms mainly on the grains). HNCO seems to be fairly constant among cores and its observed column densities are closer to the upper theoretical values; hence, the only tentative conclusion we can derive here is that the density of the observed cores is $>10^6$ $\rm cm^{-3}$, possibly as high as 10^8 $\rm cm^{-3}$; this is consistent with the emission of COMs being so compact that they trace the gas closer to the protostar. In Figure 4.4 this can be seen more clearly. We show plots of the theoretical column densities as a function of time for three different final densities. The points on the plots represent the observed column densities for every hot core in our

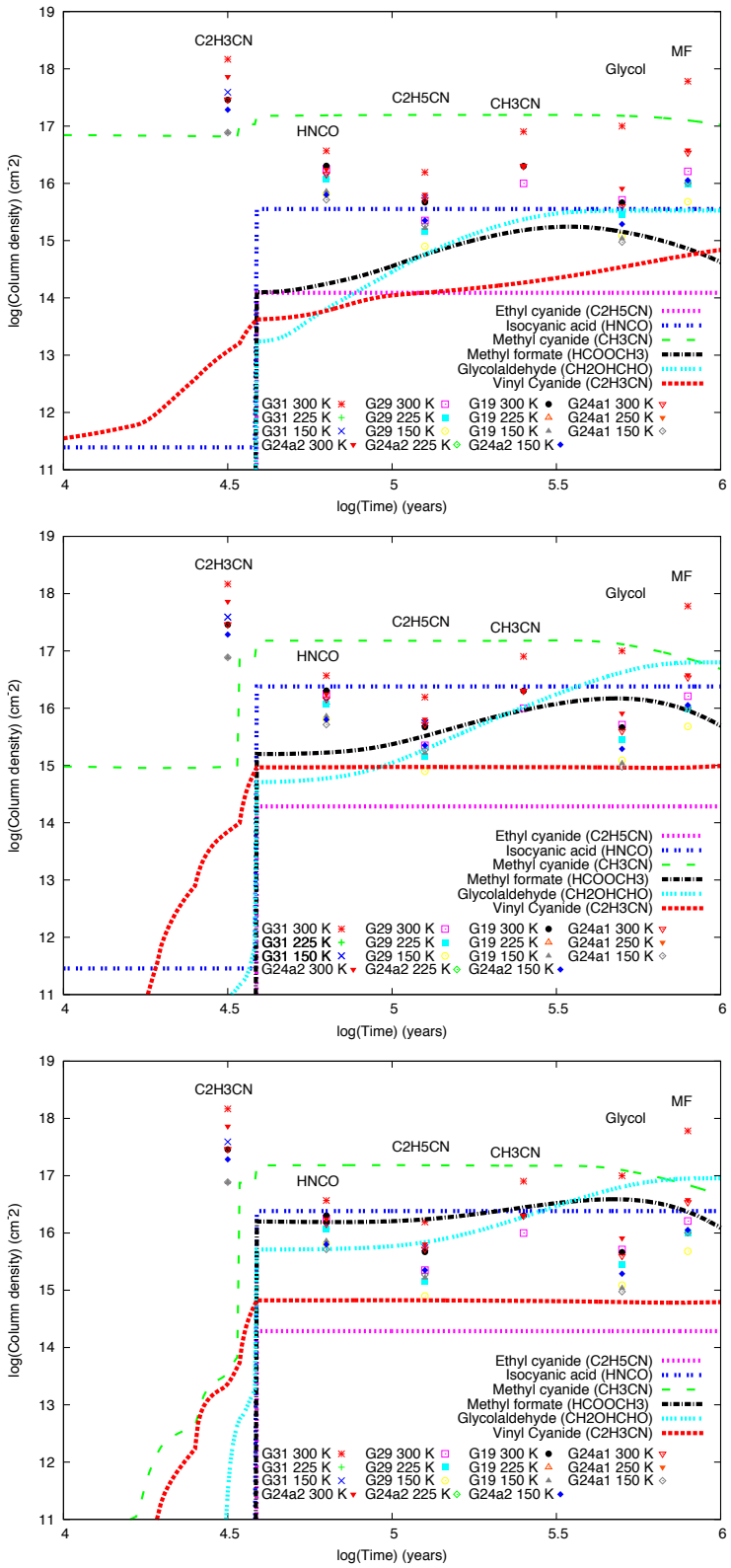

Figure 4.4: The theoretical column densities of isocyanic acid, ethyl cyanide, methyl cyanide, methyl formate, and glycolaldehyde as a function of time for a models where a 100% of CO is found in the solid phase, and the mass is $15\,M_{\odot}$, equivalent to a contraction time of 115 000 yr. The points on each graph are the observational column densities for each hot core, as determined in Chapter 3. The top panel corresponds to a final density after Phase I of $10^6\,cm^{-3}$. The middle panel corresponds to a final density after Phase I of $10^7\,cm^{-3}$. The bottom panel corresponds to a final density after Phase I of $10^8\,cm^{-3}$.

sample. For G31 the observed column densities of HNCO most clearly match theoretical column densities in the model shown in the bottom panel, where the final density is 10^8 cm^{-3}.

C_2H_5CN is, on the other hand, always under abundant in our models although, again, it is highest in models where the density and freeze-out are high. We note that, among the cores, the highest value for this species is found in G31, implying a higher density for this core.

Figure 4.4 highlights how C_2H_3CN is also under abundant in our models but is highest when the density and freeze-out are high. Again, the highest column density for this species is found in G31.

CH_3CN shows a larger variation in observed column densities, from 10^{16} cm^{-2} in G29 to 8×10^{16} in G31. A similar range is found in our models as a function, again, of density, although interestingly not of freeze-out (see Figure 4.1). Again, we conclude that G31 is the densest core, with n_H close to 10^8 cm^{-3}.

The observed $CH_2(OH)CHO$ column density is similar among all cores but G31, where it is two orders of magnitude higher than in the other objects. It is interesting to note that we can match its column density with models of gas densities of the order of 10^8 cm^{-3} for G31 and $10^6 - 10^7$ cm^{-3} for the rest of the cores, again supporting the conclusion that G31 has a higher gas densities than the rest of the objects in our sample. We note that only models where we use a high rate coefficient for the formation of glycolaldehyde are able to reproduce the observations, in agreement with the findings of Woods et al. (2012).

Finally, $HCOOCH_3$ shows the same behaviour as glycolaldehyde in that it is higher by at least one order of magnitude in G31 compared to the rest of the sample where it is more or less constant at 10^{16} cm^{-2}. In our models, we reach a column density of 10^{16} cm^{-2} at gas densities of 10^7 cm^{-3}; interestingly an increase to 10^8 cm^{-3} only yields an increase in methyl formate by a factor of few and only for a relatively short period of time, since this species seems to decline in abundance after 5×10^5 yrs. However, we point out that the column density for G31 was determined using a temperature derived from a rotational diagram, while for all the other cores a simple LTE calculation at 300 K, 225 K and 150 K was performed. In fact, in general, LTE calculations at lower temperature would yield a lower column densities, and therefore without determining the rotation temperature for all molecules it is difficult to compare observational and theoretical column densities fully.

4.6 Conclusions

We have undertaken a comparison between observations and a chemical model, UCL_CHEM, to interpret the molecular inventory of the six cores and qualitatively characterise each core and its evolutionary stage. We note that of the species we are modelling, only methyl formate and methyl cyanide have been extensively studied in the laboratory (Modica & Palumbo 2010; Bennett & Kaiser 2007; Khlifi et al. 1996; Defrees et al. 1985; Huntress & Mitchell 1979). The other complex molecules are little–known and it is very likely that our models are missing routes of formation and destruction for these species. The uncertainties related to the size of the emission region and temperatures, together with the incompleteness of the chemical networks for COMs makes a more quantitative comparison with chemical modelling inappropriate.

In conclusion, a qualitative comparison between our modelling and observations seem to yield a consistently higher density for G31 than the other objects in our sample, a result consistent with the fact that most lines are indeed the brightest in G31. We can also safely conclude that our sample only contains evolved hot cores, with an age of at least 20,000 years. The variations in the theoretical abundance of glycolaldehyde and methyl formate with time could be used as a diagnostic of age. For our sample of cores, however, their ratio is very similar in all hot cores and does not elude to any differences in age. We are unable to constrain the mass of each core; this information would have led to a better constraint for the age of each core.

Chapter 5

Acetic acid and its isomers

You're gonna need a bigger boat.

Jaws, 1975

Acetic acid (CH_3COOH) and its two isomers, methyl formate ($HCOOCH_3$), and glycolaldehyde (CH_2OHCHO), are astronomically important complex molecules. Both glycolaldehyde and methyl formate have been found to trace very compact regions of massive star formation (Beltrán et al. 2009; Calcutt et al. 2014), and acetic acid is a precursor to the amino acid acid glycine. This makes these molecules important for the study of environments significant to the formation of life, and to the understanding of massive star formation. Whilst methyl formate has been detected in a large variety of star forming regions, and acetic acid has been detected in several star forming regions, glycolaldehyde has only been detected in a handful of regions (see references below). These few detections have, however, raised interesting questions as to how these isomers form in star forming environments, and in particular how their formation routes differ in Galactic Centre locations, compared to those outside the Galactic Centre.

The first detection of glycolaldehyde was in the Sagittarius B2 region of the Large Molecule Heimat (LMH), located towards the Galactic Centre (Hollis et al. 2001). It was found to have an extended spatial extent ($\sim 60''$) with a low excitation temperature, implying that it originated from condensed–phase ice chemistry in the extended envelope, rather

than from warm gas–phase chemistry in the hot molecular core (HMC). The emission of both methyl formate and acetic acid were found to be less extended than glycolaldehyde (Hollis et al. 2001). Beltrán et al. (2009) detected glycolaldehyde for the second time outside the Galactic Centre, in the HMC G31.41+0.31 (G31). In contrast to the Galactic Centre detection, they found the emission from glycolaldehyde to be very compact, more so than methyl cyanide, a typical hot core tracer. The deconvolved size at 50% of the peak emission was found to be $\sim 1\farcs3$ ($\sim 10^4$ au) at 1.4 mm. This suggests that the emission is rather concentrated towards the centre of the core, and that glycolaldehyde is an excellent tracer of the innermost, hottest, and densest regions of HMCs, associated with the embedded high–mass protostar(s). A further detection of glycolaldehyde was made by Jørgensen et al. (2012) in the low–mass binary protostar IRAS 16293. Glycolaldehyde emission was again found to originate from the centres of the two protostars. This difference in spatial scale may indicate a different formation route in the Galactic Centre compared to that in HMCs. The 20(2,18) – 19(3,17) transition of glycolaldehyde found in G31 has also been detected in the HMCs G24.78+0.08 (G24; Beltrán et al. 2005) and in G29.96–0.02 (G29) and G19.61–0.23 (G19; Calcutt et al. 2014), bringing the total number of detections in HMCs outside the Galactic Centre to five.

Methyl formate has been detected in many high-mass (e.g. Favre et al. 2011; Sakai et al. 2007; Ikeda et al. 2001) and low–mass sources (Shiao et al. 2010; Bottinelli et al. 2004). In Calcutt et al. (2014) vibrationally excited (vt=1) transitions of methyl formate were detected in G31, G29, and G24. It was found to trace a region slightly more compact than methyl cyanide but larger than the compact region traced by glycolaldehyde, and detections of vibrationally excited transitions would suggest that methyl formate traces multiple temperature components (Calcutt et al. 2014). In Calcutt et al. (2014) we were only able to detect one transition of methyl formate in G29, G19, and G24, making our column density estimates less reliable than those of G31, which were calculated from twenty nine transitions of methyl formate. The spatial extent of methyl formate in G29 and G24 was found to be similar to that in G31 ($3''$), however the spatial extent of glycolaldehyde in the other HMCs was not found to be as compact as that in G31, and is coincident with the methyl formate emission.

Acetic acid has also been detected in both high–mass and low–mass regions. The first

detection was made by Mehringer et al. (1997) in the Sgr B2 (LMH) using the Berkeley–Illinois–Maryland Association (BIMA) Array and then confirmed with the Caltech Owens Valley Radio Observatory (OVRO) Millimeter Array, with a total of three transitions being detected. Remijan et al. (2002) used the OVRO Array to detect two new transitions toward Sgr B2 (LMH) and BIMA to detect ten transitions toward the HMC W51e2. Following on from this work Remijan et al. (2003) conducted the first survey of acetic acid, surveying twelve HMCs, and detecting it in the HMC G34.3+0.02. They found a relative $CH_3COOH/HCOOCH_3$ abundance ratio of $\sim 3.3\times10^{-2}$, which is comparable to the abundance ratio found in Sgr B2 (LMH; 3.0×10^{-2}) and W51e2 (6.0×10^{-2}). Requena-Torres et al. (2006) carried out a study of complex organic molecules in the Galactic Centre, and detected acetic acid in 40 molecular clouds. Acetic acid has also been detected in a low–mass star forming region, IRAS 16293–2422 (Cazaux et al. 2003). A survey of acetic acid was also conducted using the Combined Array for Research in Millimeter–wave Astronomy (CARMA) at 3 mm (Shiao et al. 2010), to determine if co–spatial O and N species may be an indicator for detecting acetic acid. They detected two transitions toward G19 and tentatively confirmed the detection of acetic acid toward IRAS 16293–2422. The column density of acetic acid toward G19 was found to be $2.0\times10^{16}\,\mathrm{cm}^{-2}$ and the $CH_3COOH/HCOOCH_3$ abundance ratio was found to be 0.22. A column density of $1.6\times10^{15}\,\mathrm{cm}^{-2}$ was found toward IRAS 16293–2422, with a $CH_3COOH/HCOOCH_3$ abundance ratio of 0.1 toward G19.

To date, there are only four sources where acetic acid, methyl formate, and glycolaldehyde have all been detected: MC G-0.11-0.08 and MC G-0.02-0.07, located in the Sgr A* complex (Requena-Torres et al. 2008), and MC G+0.693-0.03 (Requena-Torres et al. 2008) and the LMH (Hollis et al. 2001), located in the Sgr B2 complex. All of these sources are in the Galactic Centre. Table 5.1 shows the relative abundance ratios of acetic acid, glycolaldehyde, and methyl formate determined in each of these objects. In order to explore how these differing physical conditions affect the chemistry of acetic acid, glycolaldehyde, and methyl formate in the Galactic Centre compared to that outside the Galactic Centre, their abundance ratio must also be determined in several hot cores outside the Galactic Centre. In April 2013 we began a series of single–dish observations with the JCMT to increase the number of sources where this ratio has been calculated. Whilst our limited spatial resolution means we cannot investigate the spatial extent of

Table 5.1: Abundance ratios for acetic acid (aa) : glycolaldehyde (gly) : methyl formate (mf) determined in the only four sources where these molecules have been detected, all of which are located in the Galactic Centre.

Source	Ratio aa:gly:mf
LMH, Sgr B2	∼1:0.5:26
MC G+0.693 – 0.03, Sgr B2	1:>5:>25
MC G – 0.11 – 0.08, Sgr A*	1:>4:>20
MC G – 0.02 – 0.07, Sgr A*	1:>6:>20

these molecules, we have been able to perform a comparative study of acetic acid, methyl formate, and glycolaldehyde chemistry in several HMCs.

Following on from the detections of methyl formate and glycolaldehyde detailed in Chapters 2 – 4, in this Chapter we present the results of a study of acetic acid, methyl formate, and glycolaldehyde emission in G31, G29, G19, and G24. The aims of this work are:

1. To increase the number of methyl formate transitions detected in our hot core sample, focusing on excited (vt=1) transitions, to determine if multiple temperature components are present.

2. To increase the number of glycolaldehyde transitions detected in our hot core sample, thereby providing more accurate column densities and rotation temperature estimates, and in the case of G29, G19 and G24, confirm the presence of glycolaldehyde in these cores.

3. To detect transitions of acetic acid for the first time in G31, G29, and G24.

4. To determine the abundance ratio between acetic acid, methyl formate, and glycolaldehyde in our sample of HMCs, to constrain the chemical formation pathways of these molecules in HMCs.

5.1 Observations and data analysis

5.1.1 A3 observations

The dual–band A3 receiver on the JCMT was used in beam–switch mode to observe G31 between April 2013 and June 2013. A severe line blending problem was seen due to the

spectrally crowded nature of hot cores and the dual–band nature of the receiver. The observations were centred on the 228.073 GHz, 20(*,19) – 19(*,18) vt=0 transition of acetic acid in the lower sideband, as this was one of the few bright (106 Sμ^2) lines of acetic acid that had an uncontaminated frequency space in the upper sideband. To ensure the sideband separation was exactly 8 GHz, and the line of acetic acid would not be blended with another line in the upper sideband, the telescope was centred on a doppler shifted frequency to account for the source velocity of 96.6 kms^{-1}, and then the source velocity was set to 0 kms^{-1}. This ensured the acetic acid detection was in the centre of the sideband. As part of the data analysis process the spectra were doppler shifted back to the correct frequency. Additionally, observations were taken that were centred at 271.874 GHz, 230.538 GHz, 238.517 GHz, and 260.632 GHz, to detect more transitions of glycolaldehyde, acetic acid, and methyl formate. A total of 24 hrs was used to observe G31 with the A3 receiver. The beam size was 20″and the beam efficiency was 0.69.

5.1.2 HARP observations

Between April and May 2014 the HARP receiver on the JCMT was used with two spectral regions, to observe two frequency ranges towards G24, G29, and G19, the first centred on the 30(*,29) – 29(*,28) transition of acetic acid at 334.498 GHz, and the second centred on the 30(*,27) – 29(*,26) transition of acetic acid at 354.231 GHz. Each spectral region is separated by 0.99 GHz and is 0.91 GHz in width. HARP was chosen for the follow up observations to avoid the dual sideband blending issues that were encountered with receiver A3. For G19 and G24 the beam–switch mode was used on the telescope, whereas for G29 the position–switch mode had to be used as CO maps (Olmi et al. 2003) indicated there was no region free of emission within 180″of the source centre (the beam–switch limit for the JCMT). A total of 11.8 hrs was used to observe G24, G29, and G19. Details of the coordinates and V_{LSR} for each source can be found in Table 2.1. The beam size was 14″and the beam efficiency was 0.63.

The calibrated data product was retrieved from the JCMT OMP and then reduced and analysed using the starlink and class software packages. The data were combined using the makecube command in smurf, and then converted into class format for line fitting. The line fitting procedure and error calculations are the same as those described in Sections 2.4.1 and 2.4.2 in Chapter 2.

Table 5.2: Transitional information, including the quantum numbers, rest frequencies, upper energy levels, Einstein A coefficients, and upper state degeneracies, for the nine transitions of $HCOOCH_3$ detected in these observations.

Transition	Rest frequency (GHz)	E_u (K)	A (s^{-1})	g_u
22(10, 13) – 21(10,12)A vt=0	271.67085	216	2.41e-4	90
27(11, 17, 1) – 26(11, 16, 1)E vt=0	334.04436	304	4.74e-4	110
26(5, 21, 5) – 25(5, 20, 5)E vt=1	334.22860	416	5.48e-4	106
27(10, 17, 2) – 26(10, 16, 2)E vt=0	334.85095	290	4.93e-4	110
27(10, 17, 0) – 26(10, 16, 0)A vt=0	334.87279	290	4.94e-4	110
33(1, 33, 1) – 32(0, 32, 2)E vt=0	354.60777	293	6.96e-5	134
29(13, 17, 3) – 28(13, 16, 3)A vt=1	355.15521	556	5.47e-4	118
29(13, 17, 4) – 28(13, 16, 4)E vt=1	355.42621	556	5.48e-4	118
29(12, 18, 3) – 28(12, 17, 3)A vt=1	355.58863	539	5.69e-4	118

In these observations we detect a large range of molecular transitions, including strong lines of $^{13}CH_3OH$, C_2H_3CN, and HCN. A full analysis of these lines, however, is beyond the scope of this chapter, and in the following sections we focus on methyl formate, glycolaldehyde, and acetic acid emission.

5.2 Methyl formate ($HCOOCH_3$)

In this work we detect nine new transitions of methyl formate, including four excited (vt=1) transitions (Table 5.2). We determine the integrated intensity, main beam temperature, FWHM, rms, and sigma detection level for each transition from a Gaussian fit (Table 5.3). The blue line in Figures 5.1, 5.2, 5.3, and 5.4 show these fits overlaid on the spectra. The solid lines represent the fit to the methyl formate lines of interest, and the dashed lines represent the fits to the transition they are blended with.

Several of these transitions suffer from severe blending with other molecules. In particular, the 27(11, 17, 1) – 26(11, 16, 1)E vt=0 transition of methyl formate is blended with vinyl cyanide in all cores, but in G29 this severe blend leads to a poor fit. This transition is therefore excluded from the rotation diagram analysis for G29. The 27(10, 17, 2) – 26(10, 16, 2)E vt=0 transition of methyl formate is more severely blended in G29 than the other cores. In order to generate a realistic fit to the data the FWHM was fixed, and the centre and temperature peak were free parameters. For parameters that are fixed a fitting error cannot be generated, and the flux error derived from the fit can be underestimated. The

29(13, 17, 4) – 28(13, 16, 4)E vt=1 and 29(12, 18, 3) – 28(12, 17, 3)A vt=1 transitions were also severely blended in G29 and G24, and the 27(10, 17, 0) – 26(10, 16, 0)A vt=0 transition was severely blended in G19. These fits were determined by fixing the FWHM, based on a visual inspection of the data.

Using the rotation diagram method we combine the transitions detected in Chapter 2 and those detected in this work to derive a column density (Table 5.4) and rotation temperature (Table 5.5) for methyl formate in our HMC sample. We use a source size of 3″.5 in G31 and 3″in G29, G29, G19, and G24, as determined from the spatial extent map in Figure 2.10, to correct for beam dilution. Figure 5.5 shows the rotation diagrams for G31, G29, G19 and G24. A large scatter of data points is seen in the rotation diagrams for all of our hot core sample, with vt=0 transitions being particularly affected. These diagrams strengthen the argument discussed in Section 3.1 of Chapter 3, that methyl formate is optically thick or in non–LTE conditions in these hot cores. At present there is no indication that this scatter is due to two temperature components, however without a far larger sample of data points it is difficult to accurately characterise these rotation diagrams. In particular, additional observations are needed of methyl formate isotopologues in order to compute optical depths.

The column densities we derive for G31 and G29 are of the same order of magnitude as was determined in Chapter 3, however in the case of of G19 and G24 the column densities are an order of magnitude higher. This highlights the need to determine column densities from a large number of transitions to ensure that an accurate value is determined. We the additional transitions detected in this chapter we have been able to determine rotation temperatures in every hot core in our sample. G29, G19, and G24 have a range of 141 – 169 K. The value for G31 is slightly higher at 191 K.

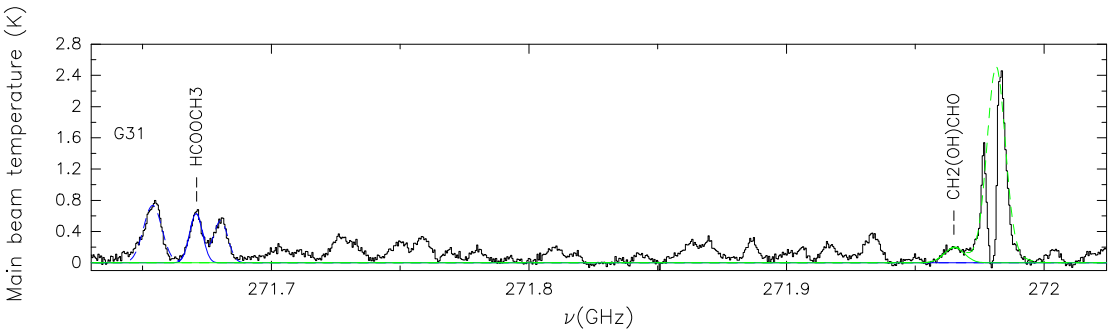

Figure 5.1: Spectra centred at 271.874 GHz on the HMC G31. The solid blue line is for Gaussian fits of $HCOOCH_3$ transitions, and the solid green line is for Gaussian fits of $CH_2(OH)CHO$ transitions. The dashed lines are the fits of blended transitions not discussed in this chapter.

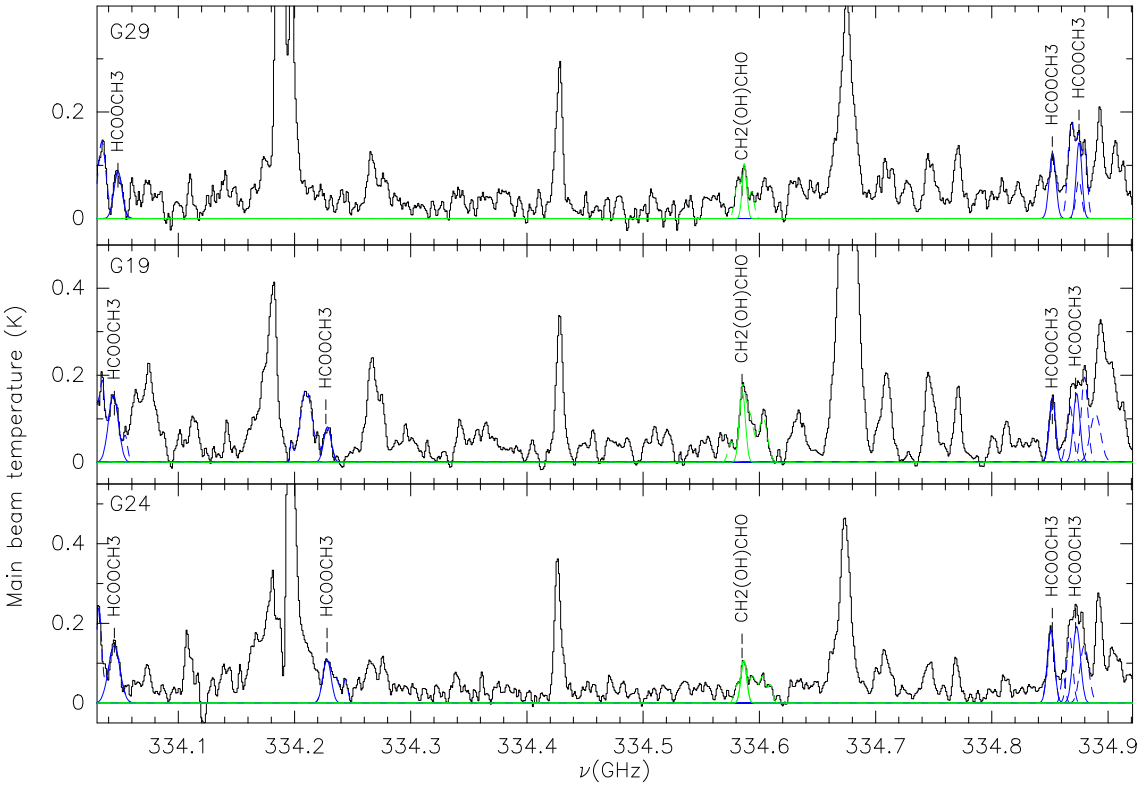

Figure 5.2: Spectra centred at 334.498 GHz on the HMCs G29, G19, and G24. The blue line is for Gaussian fits of $HCOOCH_3$ transitions, and the green line is for Gaussian fits of $CH_2(OH)CHO$ transitions.

Table 5.3: Integrated intensity, main beam temperature, FWHM, rms, and sigma detection level information determined from a Gaussian fit of the $HCOOCH_3$ transitions detected in these observations.

Frequency (GHz)	$\int T\,\mathrm{d}v$ (Err) ($\mathrm{Kkms^{-1}}$)	FWHM (Err) ($\mathrm{kms^{-1}}$)	T_{MB} (Err) (K)	rms (K)	Sigma detection level
		G31			
271.67122	4.36 (1.05)	6.49 (0.67)	0.63 (0.08)	0.04	$>5\sigma$
		G29			
334.04892	0.70 (0.44)	7.41 (2.65)	0.09 (0.02)	0.02	$>5\sigma$
334.85285	0.78 (0.16)	6.00 (0.00)	0.13 (0.02)	0.02	$>5\sigma$
334.87500	0.78 (0.23)	5.15 (0.69)	0.14 (0.02)	0.02	$>5\sigma$
354.60810	1.78 (0.34)	5.80 (0.34)	0.18 (0.03)	0.02	$>5\sigma$
355.15573	0.28 (0.13)	4.94 (0.82)	0.05 (0.02)	0.02	3σ
355.42410	0.28 (0.06)	3.00 (0.00)	0.09 (0.03)	0.02	5σ
355.59138	0.40 (0.09)	4.30 (0.00)	0.08 (0.03)	0.02	4σ
		G19			
334.04442	1.5 (0.38)	9.10 (0.88)	0.16 (0.03)	0.02	$>5\sigma$
334.22845	0.59 (0.17)	6.78 (0.39)	0.08 (0.02)	0.02	4σ
334.85226	0.91 (0.17)	5.76 (0.23)	0.14 (0.02)	0.02	$>5\sigma$
334.87318	1.01 (0.16)	6.00 (0.00)	0.16 (0.03)	0.02	$>5\sigma$
354.60908	2.75 (0.66)	7.02 (0.86)	0.36 (0.05)	0.02	$>5\sigma$
355.15583	0.55 (0.09)	4.54 (0.04)	0.11 (0.02)	0.02	$>5\sigma$
355.42541	0.50 (0.22)	6.01 (0.88)	0.08 (0.02)	0.02	4σ
355.58997	0.75 (0.20)	5.64 (0.48)	0.13 (0.03)	0.02	$>5\sigma$
		G24			
334.04443	1.5 (0.42)	9.10 (0.88)	0.16 (0.03)	0.02	$>5\sigma$
334.23007	0.59 (0.16)	6.78 (0.39)	0.08 (0.02)	0.02	4σ
334.85227	1.23 (0.20)	6.30 (0.00)	0.19 (0.03)	0.02	$>5\sigma$
334.87316	1.42 (0.30)	6.94 (0.44)	0.19 (0.03)	0.02	$>5\sigma$
354.60815	3.08 (0.50)	6.07 (0.24)	0.48 (0.06)	0.02	$>5\sigma$
355.15398	0.47 (0.14)	5.81 (0.44)	0.08 (0.02)	0.02	5σ
355.42410	0.44 (0.14)	6.70 (0.00)	0.06 (0.02)	0.02	4σ
355.59117	0.31 (0.31)	5.00 (0.00)	0.06 (0.05)	0.02	4σ

Table 5.4: Column densities derived with the rotation diagram method using transitions of $HCOOCH_3$ detected in Chapter 2 and in these observations.

Hot core	Column density ($\mathrm{cm^{-2}}$)
G31	$4.70\ (0.02)\times10^{17}$
G29	$6.40\ (0.21)\times10^{16}$
G19	$1.00\ (0.18)\times10^{17}$
G24	$1.80\ (0.19)\times10^{17}$

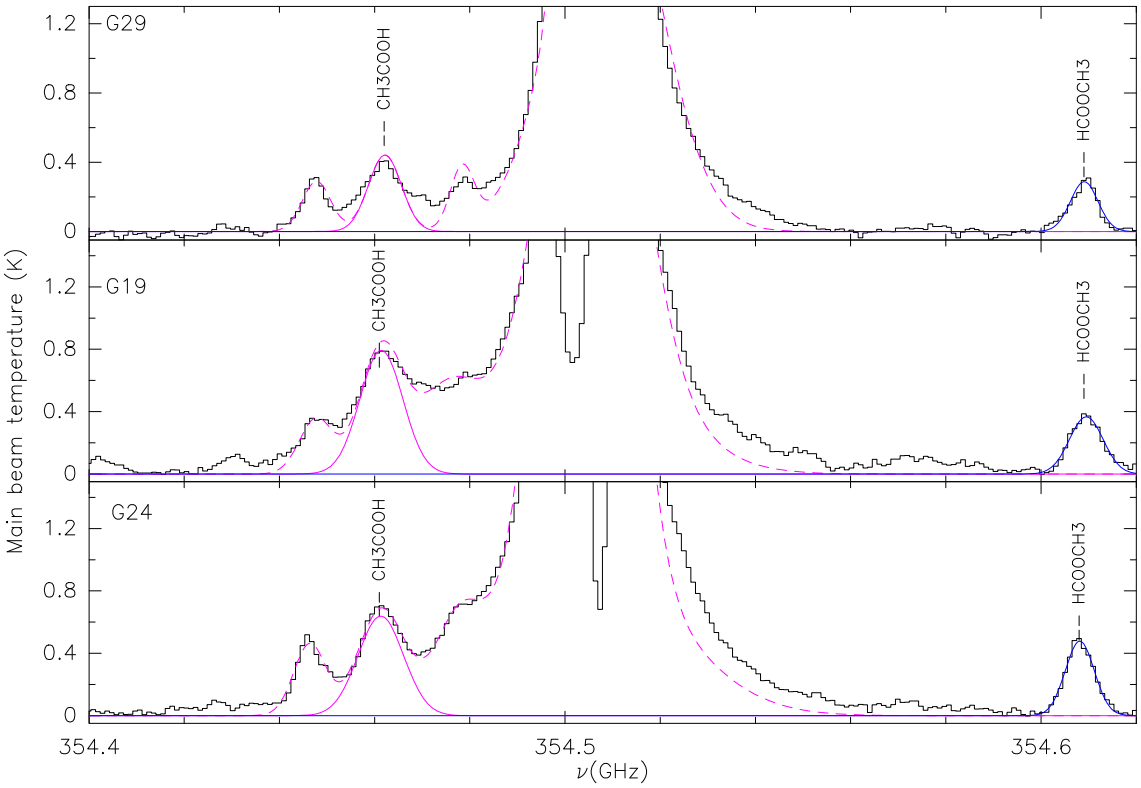

Figure 5.3: Spectra centred at 354.231 GHz on the HMCs G29, G19, and G24. The blue line is for Gaussian fits of $HCOOCH_3$ transitions, and the pink line is for Gaussian fits of CH_3COOH transitions.

Table 5.5: Rotation temperatures derived from the rotation diagram method for $HCOOCH_3$ in the hot cores G31, G19, and G24. We use a source size of 3″.5 in G31 and 3″in G29, G19, and G24 as found in Figure 2.10 to correct for beam dilution in the JCMT observations. We assume that the source fills the beam in the PdBI observations.

Hot core	Rotation temperature (K)
G31	191±19
G29	141±10
G19	169±14
G24	153±13

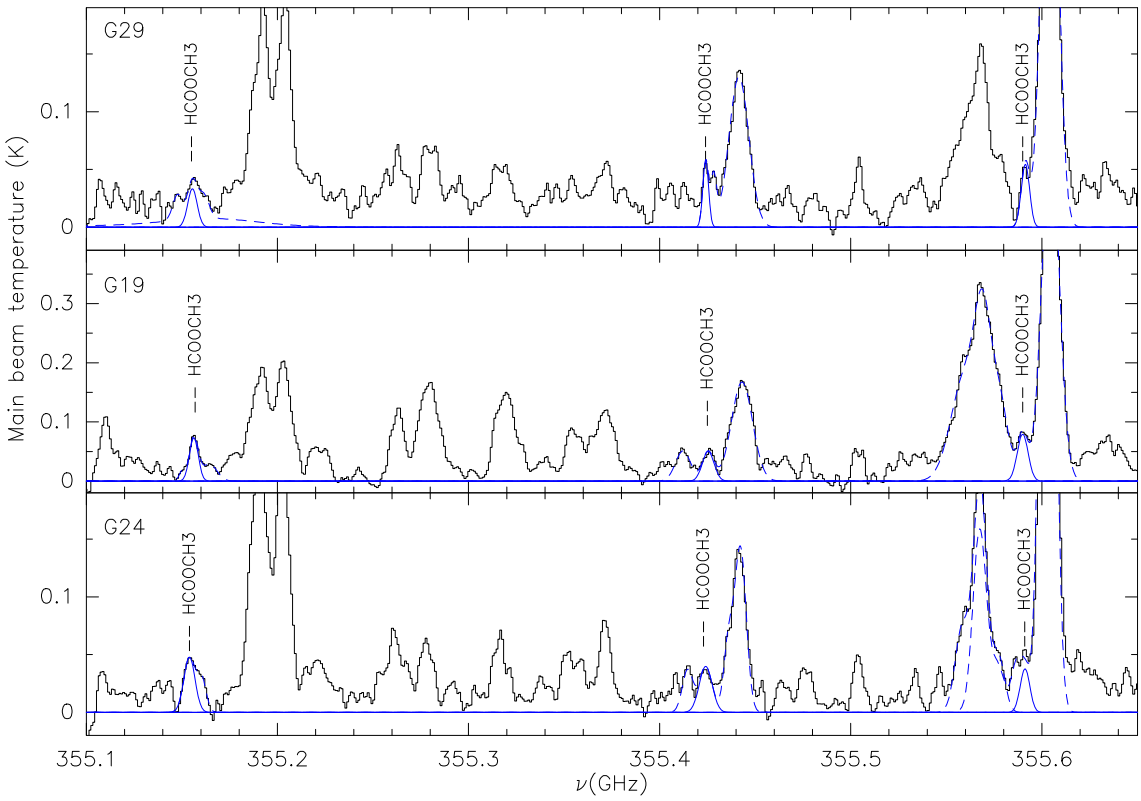

Figure 5.4: Spectra centred at 355.231 GHz on the HMCs G29, G19, and G24. The blue line is for Gaussian fits of $HCOOCH_3$ transitions.

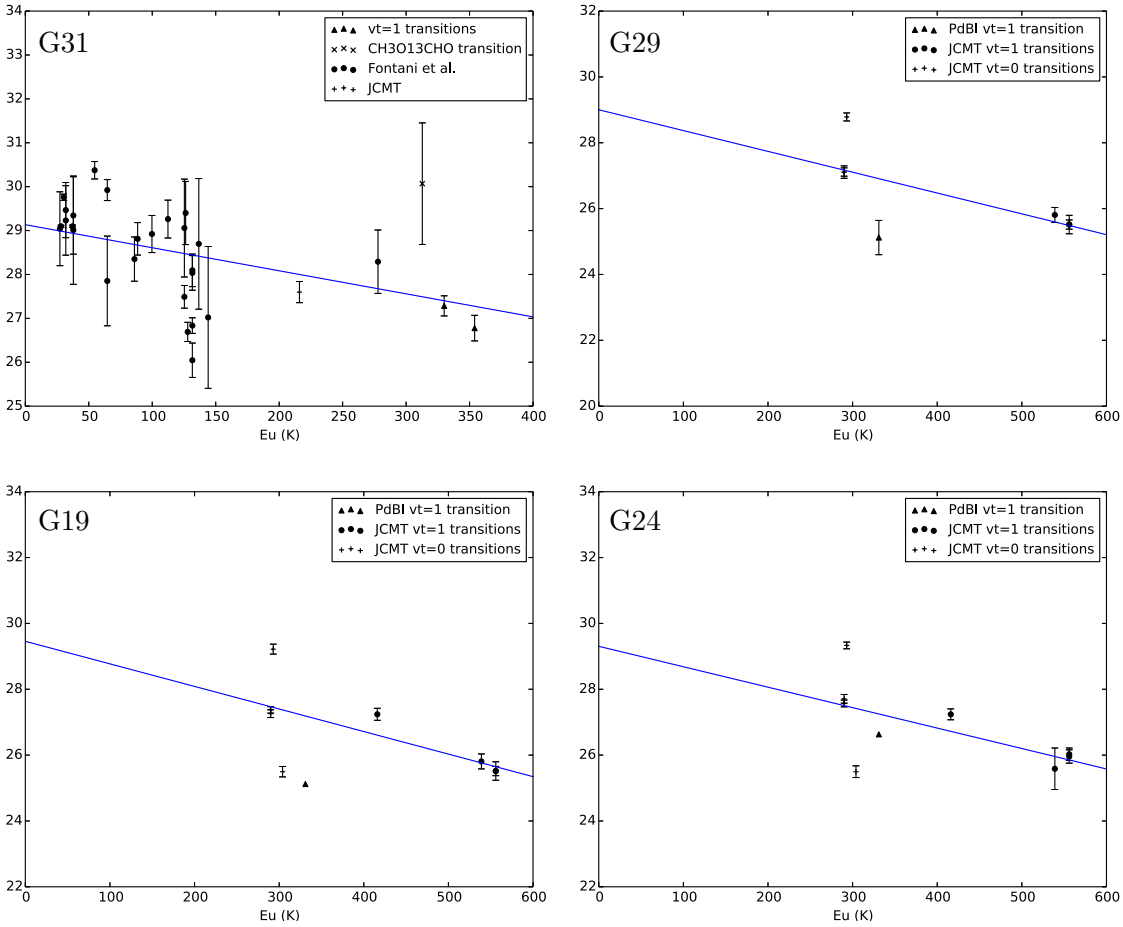

Figure 5.5: Rotation diagrams for methyl formate emission in G31, G29, G19, and G24.

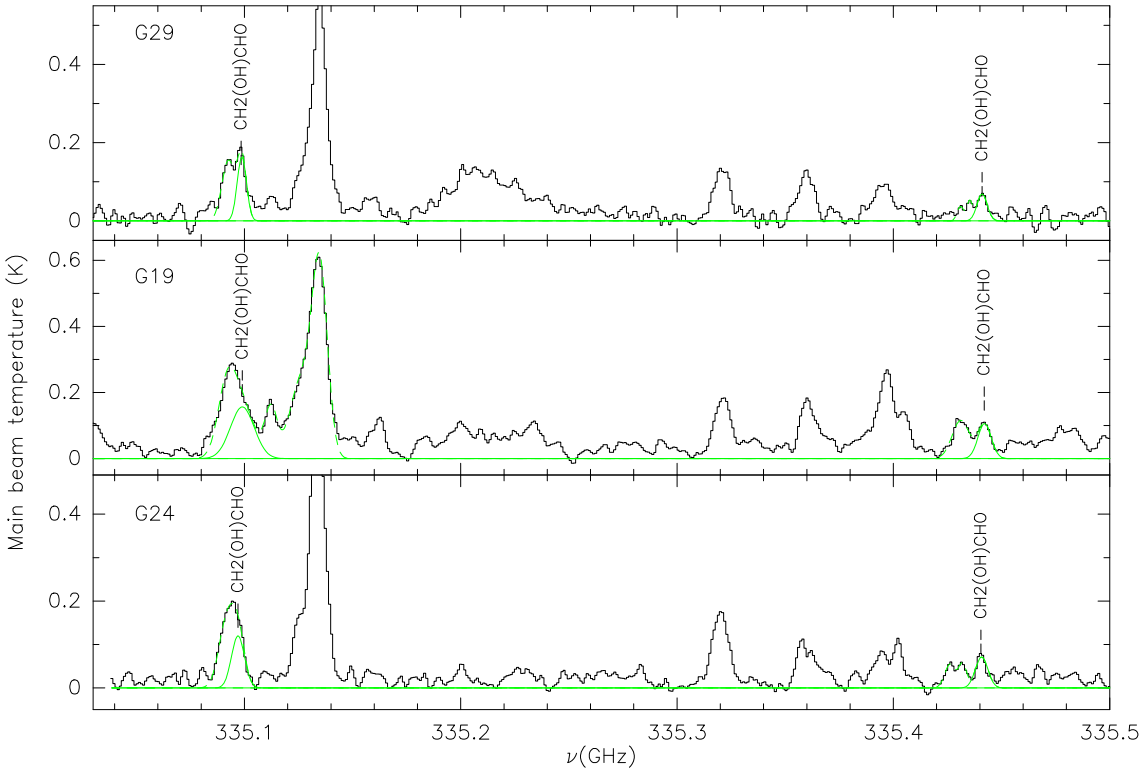

Figure 5.6: Spectra centred at 335.498 GHz on the HMCs G29, G19, and G24. The green line is for Gaussian fits of $CH_2(OH)CHO$ transitions.

5.3 Glycolaldehyde ($CH_2(OH)CHO$)

In this work we detect four transitions of glycolaldehyde (Table 5.6). These detections confirm the presence of glycolaldehyde in the HMCs G29, G19, and G24. We determine the integrated intensity, main beam temperature, FWHM, rms, and sigma detection level for each transition from a Gaussian fit (Table 5.7). The green lines in Figures 5.1, 5.2, and 5.6 show these fits overlaid on the spectra.

Unfortunately, each of these new detections suffers from blending with other molecules, however, despite this a good fit was achieved for almost all transitions. The exception to this is the 26(2,25) – 25(1,24) transition in G31, where due to blending from a prominent transition of HNC, these transitions were difficult to fit. A fit was achieved by fixing the FWHM of the 26(2,25) – 25(1,24) transition. Due to this poor fit the errors on the main beam temperature are very large. In order to achieve a realistic fit for the 17(6,11) – 16(5,12) transition of glycolaldehyde in G29, the FWHM also had to be fixed, however the quality of the fit is reasonable and this is reflected in the fitting errors for this transition.

Table 5.6: Transitional information, including the quantum numbers, rest frequencies, upper energy levels, Einstein A coefficients, and upper state degeneracies, for the five transitions of $CH_2(OH)CHO$ detected in these observations.

Transition	Rest frequency (GHz)	E_u (K)	A (s^{-1})	g_u
26(2,25) – 25(1,24)	271.96700	184	7.06e-4	53
35(14,21) – 35(13,22)	334.58731	470	8.03e-4	71
17(6,11) – 16(5,12)	335.09789	107	5.34e-4	35
34(14,20) – 34(13,21)	335.44098	450	7.97e-4	69

Figure 5.7 shows the rotation diagrams for glycolaldehyde emission in G29, G19, and G24. We combine the detections in Chapter 2 and this work to determine column densities (Table 5.8) and rotation temperatures (Table 5.9). We use a source size of $2''$ in G31 and $3''$ in G29, G19, and G24, which are determined from the spatial extent maps in Figure 2.10, to correct for beam dilution. We are unable to determine rotation temperatures for G31. The temperatures we derive for G29 (292 K), G19 (368 K) and G24 (241 K) suggest that glycolaldehyde traces relatively hot gas. The column densities of glycolaldehyde we derive for G29 and G24 are of the same order of magnitude as we found in Chapter 3. In Table 5.8, the column density for G31 is given as a range of values, determined for each

Table 5.7: Integrated intensity, main beam temperature, FWHM, rms, and sigma detection level information determined from a Gaussian fit of $CH_2(OH)CHO$ transitions detected in the HMCs G31, G29, G19, and G24.

Frequency (GHz)	$\int T\,\mathrm{d}v$ (Err) ($\mathrm{Kkms^{-1}}$)	FWHM (Err) ($\mathrm{kms^{-1}}$)	T_{MB} (Err) (K)	rms (K)	Sigma level
		G31			
271.96516	2.11 (7.80)	10.22 (0.58)	0.19 (0.70)	0.04	
		G29			
334.58843	0.44 (0.23)	4.16 (0.88)	0.09 (0.03)	0.02	$>5\sigma$
335.09974	0.80 (0.17)	4.50 (0.00)	0.16 (0.03)	0.02	$>5\sigma$
335.44205	0.36 (0.17)	4.94 (0.24)	0.06 (0.03)	0.02	4σ
		G19			
334.58644	0.94 (0.36)	5.51 (0.88)	0.16 (0.03)	0.02	$>5\sigma$
335.09950	1.92 (0.63)	11.58 (0.87)	0.16 (0.03)	0.02	$>5\sigma$
335.44397	0.72 (0.31)	6.44 (0.40)	0.11 (0.03)	0.02	$>5\sigma$
		G24			
334.58764	0.59 (0.20)	5.18 (0.17)	0.11 (0.03)	0.02	$>5\sigma$
335.09805	0.80 (0.36)	5.44 (0.78)	0.14 (0.05)	0.02	$>5\sigma$
335.44196	0.23 (0.14)	3.17 (0.59)	0.06 (0.03)	0.02	4σ

Table 5.8: Column densities derived with the rotation diagram method using transitions of $CH_2(OH)CHO$ detected in Chapter 2 and in these observations.

Hot core	Column density ($\mathrm{cm^{-2}}$)
	300 K
G31	4.77 (0.1)$\times10^{15}$–8.10 (0.07)$\times10^{16}$
G29	1.08 (0.19)$\times10^{16}$
G19	2.28 (0.26)$\times10^{16}$
G24	1.08 (0.33)$\times10^{16}$

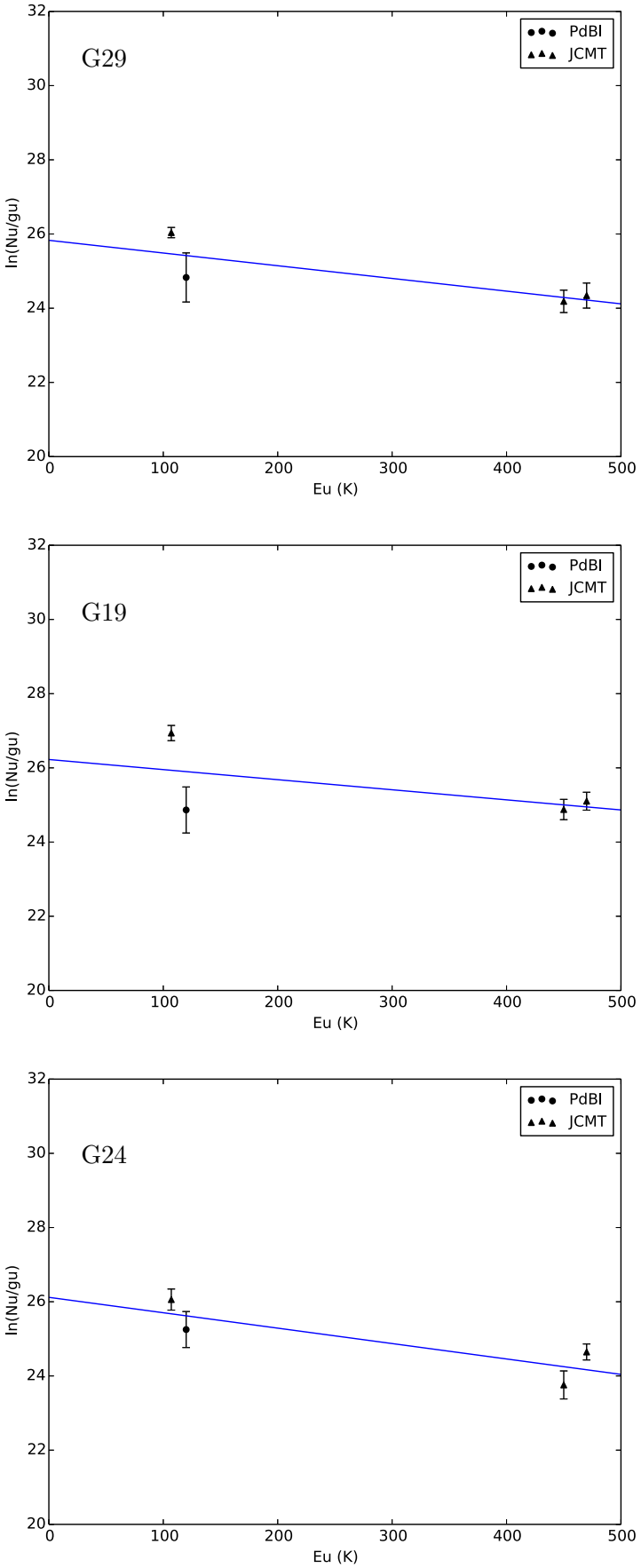

Figure 5.7: Rotation diagrams for glycolaldehyde emission in G29, G19, and G24.

Table 5.9: Rotation temperatures derived from the rotation diagram method for $CH_2(OH)CHO$ in the hot cores G29, G19, and G24. We use a source size of $2''$ in G31 and $3''$in G29, G19, and G24, which are determined from the spatial extent maps in Figure 2.10, to correct for beam dilution in the JCMT observations. We assume the source fills the beam in the PdBI observations.

Hot core	Rotation temperature (K)
G29	292±64
G19	368±102
G24	241±50

transition. The spread in column density spans an order of magnitude indicating that transitions of glycolaldehyde in this core may be affected by optical thickness or non-LTE conditions.

5.4 Acetic acid (CH_3COOH)

In this work we detect two transitions of acetic acid (Table 5.10). The detections made in G31, G29, and G24 are the first detections of this molecule in these hot cores, however, more transitions are needed to determine accurate column densities and rotation temperatures. We determine the integrated intensity, main beam temperature, FWHM, rms, and sigma detection level for each transition from a Gaussian fit (Table 5.11). The pink line in Figures 5.3, and 5.8 show these fits overlaid on the spectra. We estimate column densities in each core in Table 5.11, but are unable to derive rotation temperatures as more transitions are needed. We assume a source size of $2''$ for all HMCs, as was found in G19 by Shiao et al. (2010).

The 30(*,27) – 29(*,26) – vt=0 transition of acetic acid detected in G29, G19, and G24 is blended with several other molecules including the J=4–3 transition of HCN. Self–absorption is seen in the HCN line indicating that it might be tracing an outflow. In order to determine the level of contamination of the acetic acid line with nearby molecules, all emission was modelled, including a high–velocity component to account for the wings on the HCN line. Figure 5.3 shows the acetic acid, and the overall profile of the combined fit of all blended molecules. In order to achieve this fit in G29 and G19, it was necessary to fix the FWHM of the acetic acid transition to produce a realistic fit. This produced a very good fit to the data, however, the error on the flux for these transitions is underestimated, as no error can be calculated for the FWHM.

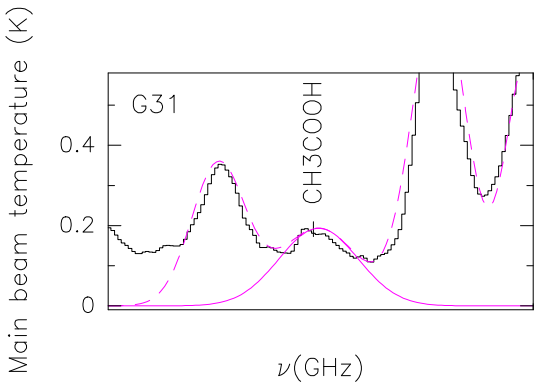

Figure 5.8: The spectrum of the 20(*,19) – 19(*,18) – vt=0 transition of CH_3COOH detected in G31.

Table 5.10: Transitional information, including the quantum numbers, rest frequencies, upper energy levels, Einstein A coefficients, and upper state degeneracies, for the two transitions of CH_3COOH detected in these observations.

Transition	Rest frequency (GHz)	E_u (K)	A (s^{-1})	g_u
20(*,19) – 19(*,18) – vt=0†	228.07369	122	3.59e-4	41
30(*,27) – 29(*,26) – vt=0	354.46196	286	1.29e-3	61

† For details of the * notation please see Ilyushin et al. (2008).

5.5 Abundance ratios

Table 5.13 shows the abundance ratios between acetic acid, glycolaldehyde, and methyl formate in the HMCs in our sample. For G31 we calculate the ratio between glycolaldehyde and acetic acid for lowest and highest column density we derive from the transitions of glycolaldehyde. Work by Lattelais et al. (2009) and Lattelais et al. (2010) has explored the relationship between the stability of different molecular isomers and their observational abundance in the interstellar medium. By comparing the column densities for fourteen sets of isomers, detected in hot cores, molecular clouds, PDRs, and AGBs, they found that for most sets of isomers, the most stable isomer (i.e. the lowest energy) was the most abundant, and that there was a relationship between the difference in energy of two isomers and the difference in abundance. These two properties are referred to as the minimum energy principle (MEP). This result suggests that the formation and destruction pathways for different isomers is not the most important factor in determining the abundance ratios of isomers. They did, however, find that acetic acid and its isomers did not follow the MEP when comparing their results to the observations. Their calculations determined

Table 5.11: Source name, integrated intensity, main beam temperature, FWHM, and rms determined from a Gaussian fit of CH_3COOH transitions in the HMCs G31, G29, G19, and G24. All detections are $>5\sigma$.

Source	Frequency	$\int T\,\mathrm{d}v$ (Err)	FWHM (Err)	T_{MB} (Err)	rms
(GHz)	($Kkms^{-1}$)	(kms^{-1})	(K)	(K)	
G31	228.07020	3.30 (0.84)	17.27 (0.97)	0.18 (0.03)	0.03
G29	354.46216	3.25 (0.59)	6.90 (0.00)	0.44 (0.08)	0.02
G19	354.46239	7.59 (0.73)	9.00 (0.00)	1.25 (0.20)	0.02
G24	354.46130	6.47 (16.45)	9.53 (0.87)	0.64 (1.56)	0.02

Table 5.12: Column densities derived with the rotation diagram method using transitions of CH_3COOH detected in these observations.

Hot core	Column density (cm^{-2})
	300 K
G31	1.35 (0.18)$\times10^{17}$
G29	3.02 (0.12)$\times10^{17}$
G19	7.07 (0.09)$\times10^{17}$
G24	6.02 (1.60)$\times10^{17}$

that acetic acid is the most stable of the isomers and glycolaldehyde is the least stable. Observationally this would translate to acetic acid being the most abundant species and glycolaldehyde being the least abundant. We find in our sample that this is the case for all hot cores except for G31. The difference between this ratio in G31 and the other cores would suggest that their is a significant physical difference between G31 and the rest of the cores in the sample. The same conclusion was drawn from a discussion of the chemical richness of the hot core sample in Section 2.5 of Chapter 2. However, it was not possible to determine if the spectral difference seen is due to the effects of luminosity or age. Lattelais et al. (2010) suggest that acetic acid and its isomers might not follow MEP because there may be a stronger adsorption on the grains of acetic acid than of methyl formate, at the moment of their formation on the grain surfaces. Puletti et al. (2010) have suggested that one might observe a slow, selective isomerisation with these species, resulting in a change of abundance ratio toward the most stable isomer, i.e. acetic acid, as the interaction with the radiation field increases. This means that this ratio could be used as an indicator of age for HMCs. Applying this to the sample of hot cores discussed in this chapter, the ratio of methyl formate to acetic acid is the smallest in G19, indicating that it is the oldest core, followed by G29, and G24, and G31 is the youngest core.

Table 5.13: Abundance ratios for acetic acid (aa) : glycolaldehyde (gly) : methyl formate (mf) in the HMCs in our sample.

Hot core	Ratio aa:gly:mf
G31	1:0.04–0.6[†]:3
G29	1:0.04:0.21
G19	1:0.03:0.14
G24	1:0.02:0.30

[†]A single column density could not be derived for glycolaldehyde in G31, and hence a range for the ratio of acetic acid to glycolaldehyde is given here.

Comparing the abundance ratios determined in our sample of cores, to those determined by Hollis et al. (2001) and Requena-Torres et al. (2008) (Table 5.1), we find that the difference between Galactic Centre clouds and those in our sample are very different. The abundance ratios determined by Requena-Torres et al. (2008), in the Galactic Centre clouds MC G+0.693 – 0.03, MC G – 0.11 – 0.08, MC G – 0.02 – 0.07, are very similar, suggesting similar chemical processes are occurring in the clouds. The abundance ratio in the LMH Galactic Centre source of acetic acid and methyl formate, is similar to that of the other Galactic Centre Clouds, however, the acetic acid, glycolaldehyde ratio is significantly different, with glycolaldehyde being an order of magnitude less abundant with respect to to acetic acid, than in the other Galactic Centre clouds. Hollis et al. (2001) suggest that the conditions of the LMH favour the chemically reactive nature of glycolaldehyde over its isomers, and the ensuing chemistry leads to glycolaldehyde destruction. The abundance ratio we have determined in G29, G19, and G24 also show a significantly lower abundance of glycolaldehyde with respect to acetic acid, suggesting that the destruction of glycolaldehyde may be favoured in these cores.

5.6 Conclusions

This study highlights the importance that single–dish facilities play in abundance studies of relatively strong molecules. Detection studies of weak molecules, such as acetic acid, however, can be very difficult and it is essential that sidebands can be separated, owing to the very crowded spectra seen in star forming regions, in order to detect a large number of transitions.

Despite this, we have detected acetic acid for the first time in the HMCs G31, G29, and G24. We have also added to the number of detections in the HMC G19. We do, however, need to detect more transitions in G31, G29, and G24 to confirm the presence of acetic acid and improve the estimates of column density in these cores. Ideally these transitions should be across a wide range of upper energy levels in order to compute rotation temperatures for the first time in these cores.

In this work we detect nine new transitions of methyl formate, including four excited (vt=1) transitions, and their rotation diagrams indicate that methyl formate may be optically thick or effected by non-LTE conditions. A larger number of transitions need to be detected, particularly of isotopologues of methyl formate in order to compute optical depths.

We have also detected four transitions of glycolaldehyde which confirm the presence of glycolaldehyde in G29, G19 and G24. These detections have allowed us to compute the rotation temperatures for several of the cores indicating that glycolaldehyde does trace a hotter component compared to that of methyl formate.

We determine the abundance ratios between acetic acid, glycolaldehyde, and methyl formate for the first time in several HMCs outside the Galactic Centre. The ratio in G31 supports the conclusion drawn from Chapter 2, that G31 is physical different from the other hot cores, where a very similar ratio is determined. We find that these ratios are significantly different from those determined in the Galactic Centre, indicating significant physical differences between these populations. It is unclear whether these differences represent a difference in formation pathways for these isomers in the Galactic Centre, without comparison with a larger number of star forming regions, both in and outside the Galactic Centre. We do however postulate that the relative abundances of these isomers could be used as an indicator of age of an HMC, owing to the slow isomerisation towards the most stable isomer. To explore this concept further, a larger sample of hot cores is needed, with high spectral and spatial resolution to explore the abundance ratio of a number of isomer triplets. This would also allow the spatial extent of these molecules to be probed, ensuring abundances are not affected by beam dilution.

Chapter 6

The Chemical Composition of IRAS 17233–3606

Orbiting this at a distance of roughly ninety–eight million miles is an utterly insignificant little blue–green planet whose ape–descended life forms are so amazingly primitive that they still think Apple Watches are a pretty neat idea.

Douglas Adams

Key to understanding the chemical environments in massive star forming regions, is the study of their chemistry in a variety of objects, to build up a picture of star formation across the galaxy. In particular, it is important to find chemical tracers of the most compact regions of hot cores, in order to confirm or deny whether accretion disks are required in order to form massive stars. Current observations have only detected accretion disks around stars with masses $\leq$20 $M_{\odot}$ and luminosities $\leq 10^4$ $L_{\odot}$ (e.g. Kraus et al. 2010). With the increasing spatial resolution of current interferometers, commonly used hot core tracers such as CH_3CN, may no longer be the best molecules to use. With these goals in mind, the prominent far infrared source, IRAS 17233–3606, has been studied. Also known as G351.78–0.54, this region shows the typical signs of massive star formation, and has previously been found to have a rich complex chemistry. The region contains two cm continuum sources, a compact HII region and a weak double UCHII source (Hughes &

MacLeod 1993), found close to the location of H_2O, OH and CH_3OH masers. Zapata et al. (2008) found a cluster of four compact radio objects of sizes equal or less than $0.3''$ and varying (mostly thermal) spectral indices in the region of the double radio source. One of them is at the centre of a bipolar outflow traced by OH masers (Fish et al. 2005). Continuum observations of 1.2 mm dust emission by Faúndez et al. (2004) suggest a mass of $200\,M_\odot$ and a bolometric luminosity of $2.7\times10^4\,L_\odot$, determined from the spectral energy distribution (SED). Distances to the object have been computed by several authors (Miettinen et al. 2006; Forster & Caswell 1989) and a range of values found, between 700 pc and 2.2 kpc. Kinematical distance were constrained to $\leq$1 kpc, which is the distance we adopt for this work.

Leurini et al. (2008) studied the molecular content of the core associated with the source using the Atacama Pathfinder Experiment (APEX) telescope and mapped the CO (3 – 2), and the HCO^+ (4 – 3) emission. They also detected and modelled the CH_3OH ($6_K - 5_K$), ($7_K - 6_K$) and CH_3CN ($16_K - 15_K$) transitions, revealing a rich molecular hot core. Modelling of the spectrum suggested a hot core of size $3''$ and excitation temperature of 150 K. They also found evidence of outflows in the source, with observations of broad non–Gaussian profiles in CO (3 – 2), CS, H_2CO, SO, SO_2, and HCO^+. In Leurini et al. (2009) these molecular outflows were investigated further with combined observations, using the submillimeter array (SMA), APEX, and United kingdom Infrared Telescope (UKIRT), of CO (2 – 1), CO (6 – 5) and H_2 respectively. They found a clumpy extended ($\sim 50''$) structure with well separated blue– and red–shifted emission, and an overall structure roughly aligned along the N–S direction and centred on the region where the H_2O, CH_3OH, and OH masers are found, where the 1.3 mm emission peaks, and where four hyper–compact HII regions are located. The outflow is associated with extremely high velocities, up to $\sim$-200 and $+120\,\mathrm{km s^{-1}}$ with respect to the ambient LSR velocity. Their CO(2 – 1) observations indicated that up to eight outflow clumps were present, and that outflow multiplicity was present, as would be expected in a cluster of forming massive stars. They also determine the kinematic age of the outflows to be $10^2 - 10^3$ yr, which indicates that these are young objects which have not yet reached the main sequence, and are ideal to study the earliest stages of massive star formation. Leurini et al. (2011) followed on from this work with a dedicated search for the best tracers of rotation in IRAS 17233–3606 with a study using the SMA at 230 GHZ in the upper sideband (USB). They

found linear velocity gradients in many transitions of the same molecular species and in several molecules. Whilst a rich spectrum was found in these observations much of the emission seen remained unidentified in this paper.

In this chapter, we present a reanalysis of these observations, with the aim of identifying the remaining unidentified emission found in IRAS 17233–3606 at 230 GHz and 220 GHz, by Leurini et al. (2009), and Leurini et al. (2011). We present a discussion of the line contamination and confusion problems in the data, as well as a spectral model of the molecular emission. We analyse the column densities and rotation temperatures of the molecular content of IRAS 17233–3606, and compare the results to the molecular emission of the other hot cores presented in this thesis, with the aim of providing a more complete understanding of the chemistry seen in hot cores, as well as to identify new tracers of hot, dense and compact emission.

6.1 Observations

IRAS 17233–3606 was observed by Leurini et al. (2011) with the SMA on the 10th April 2007, using a compact configuration with seven antennas. The frequency range of the observations is 219.458 – 221.384 GHz in the LSB and 229.451 – 231.381 GHz in the USB. The quasar 3C273 was used as the phase calibrator for the observations (Leurini et al. 2011). The correlator had a bandwidth of ∼1.9 GHz and the channel spacing was 0.000406 GHz. A source velocity of $-3.40\,\mathrm{kms}^{-1}$ was used for IRAS 17233–3606. The observations were centred at α_{2000} =$17^h26^m41^s.757$, $\delta_{2000} = -36°09'0''.50$. The conversion factor from flux density to brightness temperature in the synthesized beam is $\sim 2.25\,\mathrm{K\ (Jy/beam)}^{-1}$ for the LSB, and $\sim 2.53\,\mathrm{K\ (Jy/beam)}^{-1}$ in the USB (Leurini et al. 2011). The observations were performed in good weather conditions, with zenith opacities τ(225 GHz) between 0.1 and 0.14 measured by the National Radio Astronomy Observatory (NRAO) tipping radiometer operated by the Caltech Submillimeter Observatory (CSO). Details of the synthesized beam, velocity resolution and r.m.s for each sideband can be found in Table 6.1.

6.2 Spectral identification

Figures 6.1 and 6.2 show the rich molecular emission seen in both the lower sideband (LSB) and upper sideband (USB) of these observations, labelled with the molecules that have already been identified in IRAS 17266–3606. The LSB is dominated by CH_3CN

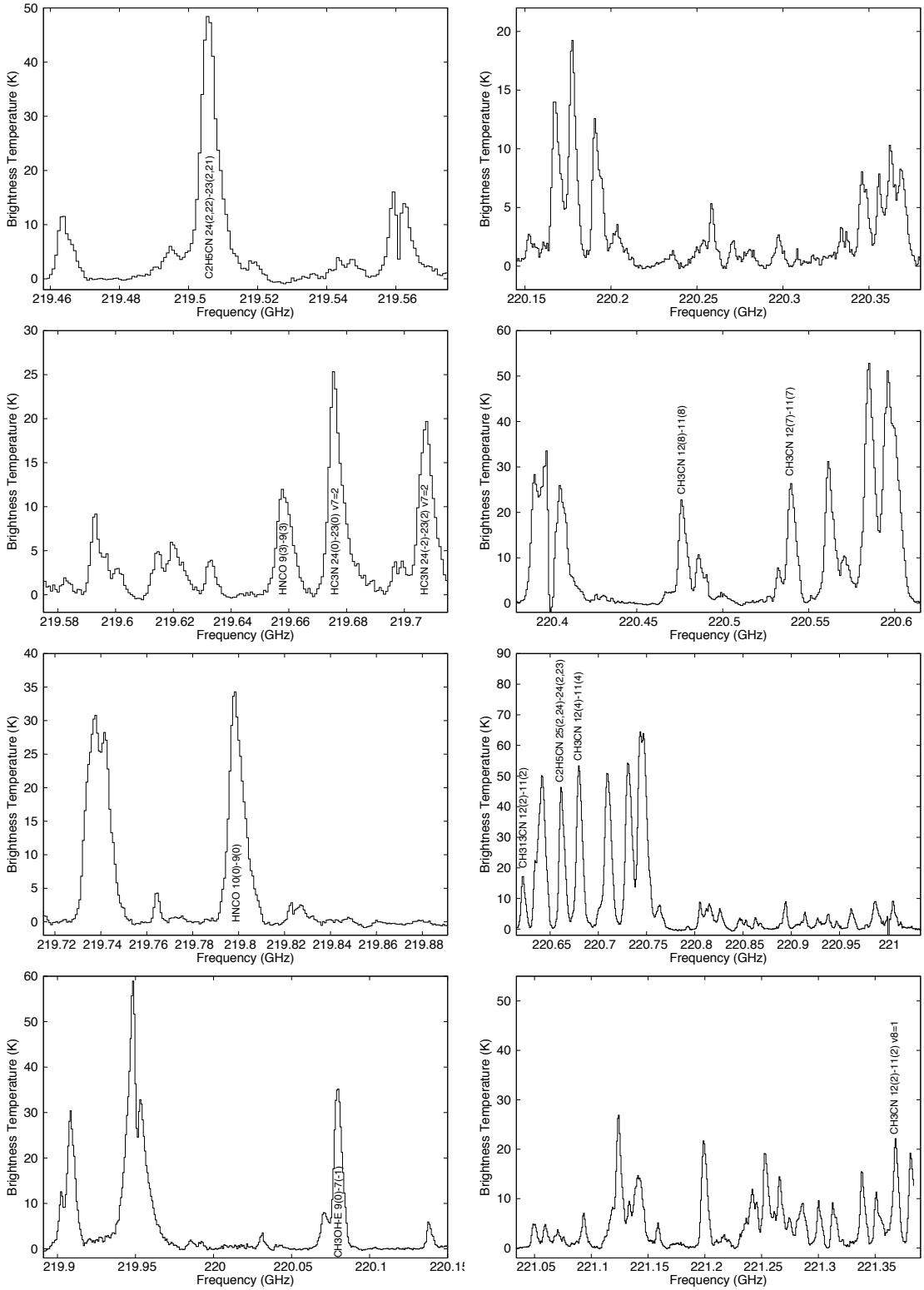

Figure 6.1: Spectra of the lower sideband, labelled with the transitions that have already been detected in this object.

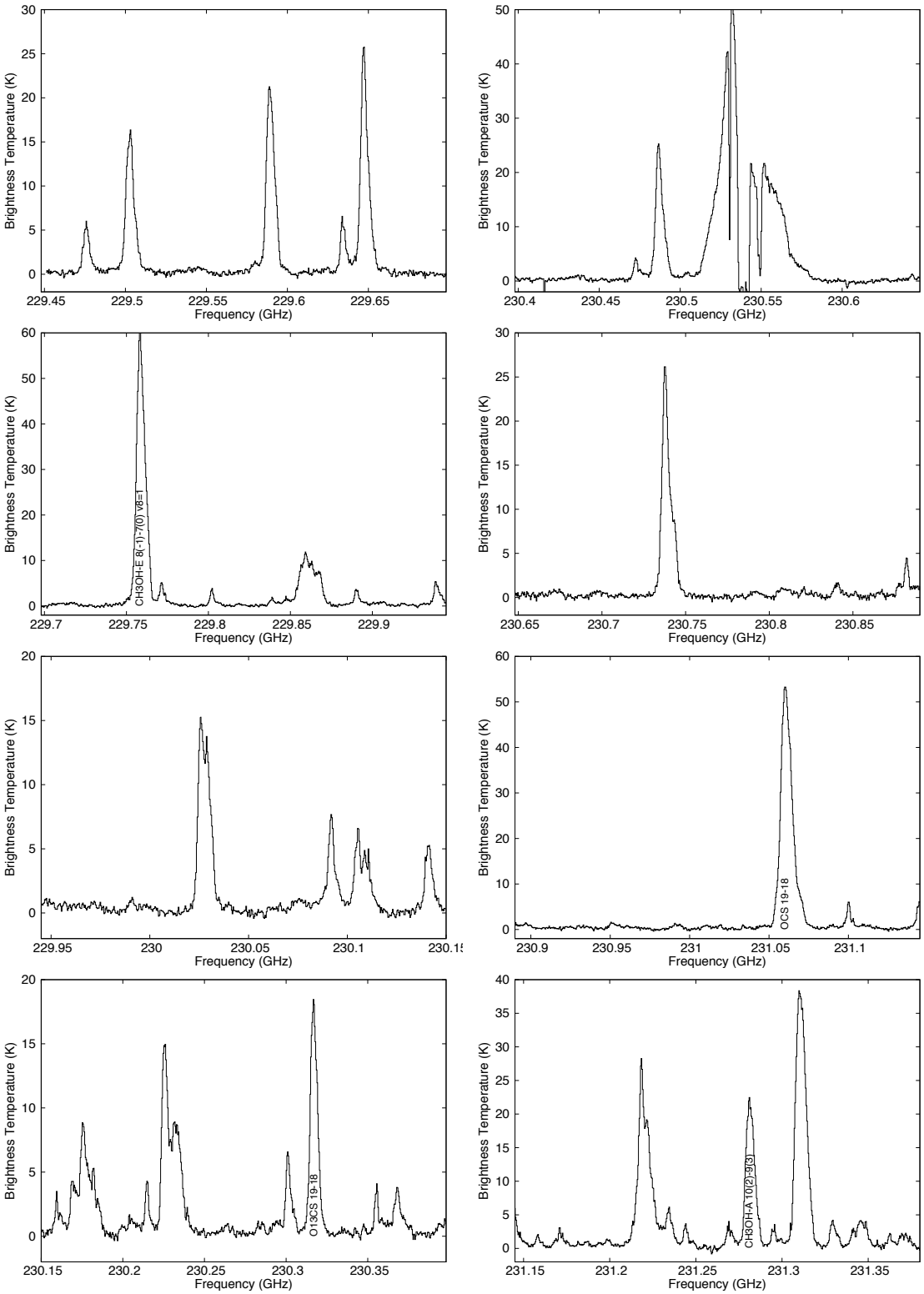

Figure 6.2: Spectra of the upper sideband, labelled with the transitions that have already been detected in this object.

Table 6.1: Details of the synthesized beam, velocity resolution and typical r.m.s for each sideband of the observations.

	HPBW ($''$)	P.A. ($\circ$)	δv (kms^{-1})	r.m.s (Jy beam^{-1})
LSB	5.″4 x 1.″9	∼29	0.5	0.1
USB	4.″9 x 1.″8	∼29	0.5	0.1

(12K – 11K), v=1 and $CH_3{}^{13}CN$ emission, whilst the USB is dominated by CO emission. Blending between different molecules in the spectra is common and therefore identifying all the emission present is a challenge. In some cases line emission overlaps to an extent where determining a fit for a specific line is impossible. It is also unclear as to what extent the molecular emission is affected by the outflows in the region, and Leurini et al. (2011) already propose that evidence of this is seen in CH_3CN in the LSB. In this work we use a combination of the identification criteria discussed in Chapter 2, and spectral modelling with the CASSIS spectral modelling software (as described in Chapter 3), to simultaneously fit multiple transitions of several molecules. To start we spectrally modelled C_2H_5CN, HNCO, HC_3N, $HCC^{13}CN$, CH_3CN, $CH_3{}^{13}CN$, $^{13}CH_3OH$, CH_3OH, $O^{13}CS$, OCS, CO, ^{13}CO, $C^{18}O$, H_2O, OH, SO, ^{34}SO, ^{33}SO, SO_2, CS, $C^{34}S$, H_2CS, DCN, $HCOOCH_3$, CH_3CCH, H_2CO, and HCO^+ emission, as these molecules have already been identified in the object. A candidate line list was then determined from the Splatalogue catalogue, with an upper energy range of 0 – 1300 K, as the highest upper energy level of a transition previously detected was 1157 K for the 12(8, 1, 11) – 11(8, 1, 11) transition of CH_3CN v8=1. After this process there remained several emission features which had not been identified, suggesting the emission was due to species that are not listed in the JPL, CDMS or NIST databases, which CASSIS uses in order to model spectra. Species were then excluded from the candidate line list if spectral modelling predicted transitions at detectable levels in spectral regions of no emission. Only transitions with a frequency error of <0.05 GHz were considered. Column densities and excitation temperatures were varied within the spectral model until a best fit was found for all detected species. In this process LTE was assumed and a source size for all species of $3''$ is assumed as in Leurini et al. (2008). The LSR used for all species was taken to be that of the object LSR (-3.40 kms^{-1}). Using the CLASS software from the Gildas software package, a Gaussian fit was performed to derive the velocity, integrated intensity, brightness temperature, and

FWHM for each detected transition. In instances where many transitions were blended together, spectral modelling was used as a guide to perform a multiple line Gaussian fit of all of the emission seen. The fitting procedure and error calculations are described in detail in Sections 2.4.1 and 2.4.2 in Chapter 2.

6.2.1 Deuterated cyanoacetylene (DC_3N)

The 26 – 25 v=0 transition of DC_3N is detected at 219.49078 GHz (Figure 6.3). Table 6.2 details the velocity, integrated intensity, temperature brightness, FWHM, and rms information determined from a Gaussian fit. Table 6.3 shows the transitional information, including the rest frequency, upper energy level, Einstein A coefficient, and upper state degeneracy. This transition is blended with an unidentified line at 219.49460 GHz but it does pass the Rayleigh criterion. This species has previously been detected in several massive star forming regions, e.g. the hot core of the Orion KL (Esplugues et al. 2013) and NGC7129 (Fuente et al. 2014). This is however the first transition detected in IRAS 17233–3606. No other transitions of DC_3N are predicted in the frequency range of our observations. At least two further transitions of this species need to be detected in IRAS 17233–3606 in order to confirm its presence and to accurately determine observational column densities. Determining the identity of the line blended with DC_3N is also needed to determine the extent of the blending observed. Despite these concerns, a column density derived from this transition has been determined in Section 6.3 in order to provide quantitative comparison of the chemistry observed in different massive star forming regions.

Table 6.2: Velocity, integrated intensity, temperature brightness, FWHM, and rms information determined from a Gaussian fit for the 26 – 25 transition of DC_3N.

Frequency (GHz)	V_{LSR} (kms^{-1})	V_{peak} (kms^{-1})	$\int T\,dv$ ($Kkms^{-1}$)	FWHM (kms^{-1})	T_B (K)	rms (K)
219.49013	−3.40	−2.96	9.73 (3.52)	4.00 (0.55)	2.29 (0.51)	0.2

Table 6.3: Transitional information, including the quantum number, rest frequency, upper energy level, Einstein A coefficient, and upper state degeneracy, for the 26 – 25 transition of DC_3N detected in these observations.

Transition	Rest frequency (GHz)	E_u (K)	A (s^{-1})	g_u
26 – 25 v=0	219.49045	142	0.00084	53

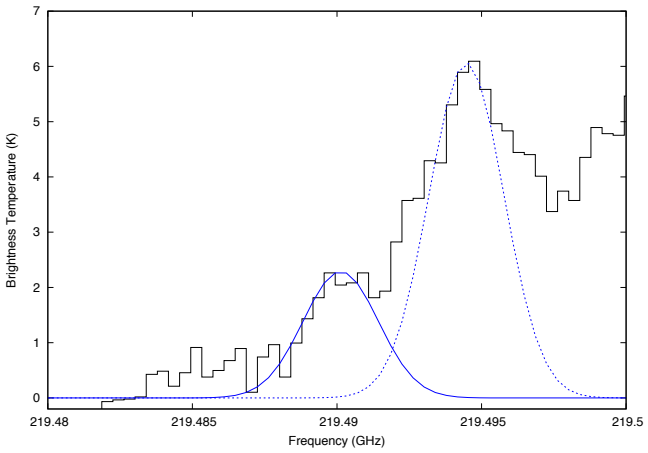

Figure 6.3: The solid line shows the fit of the 26 – 25 transition of DC_3N. This transition is blended with an unidentified line at 219.49460 GHz represented by the dashed line, but it does pass the Rayleigh criterion.

6.2.2 Ethyl cyanide (C_2H_5CN)

Table 6.4: Velocity, integrated intensity, temperature brightness, FWHM, and rms information determined from a Gaussian fit for all four transitions of C_2H_5CN.

Frequency (GHz)	V_{LSR} (kms^{-1})	V_{peak} (kms^{-1})	$\int T\,dv$ ($Kkms^{-1}$)	FWHM (kms^{-1})	T_B (K)	rms (K)
219.50560	−3.40	−3.41	386.45 (89.62)	7.95 (0.24)	45.68 (9.21)	0.2
219.90219	−3.40	−3.00	63.71 (15.44)	4.84 (0.20)	12.37 (2.49)	0.2
220.66187	−3.40	−4.69	405.49 (93.42)	8.66 (0.25)	43.97 (8.86)	0.2
231.31076	−3.40	−3.84	372.15 (80.39)	9.06 (0.14)	38.60 (7.74)	0.3

In these observations four transitions of C_2H_5CN are detected (Figure 6.4). The 24(2,22) – 23(2,21) and 25(2,24) – 24(2,23) transitions have been detected previously by Leurini et al. (2011) and here we present new detections of the 12(3,10) – 11(2,9) and 26(1,25) – 25(1,24) transitions. Table 6.4 details the velocity, integrated intensity, temperature brightness, FWHM, and rms information determined from a Gaussian fit. Table 6.5 shows the transitional information, including the rest frequency, upper energy level, Einstein A coefficient, and upper state degeneracy. The 12(3,10) – 11(2,9) transition is blended with the 3(1, 2) – 2(1, 1) transition of $H_2{}^{13}CO$.

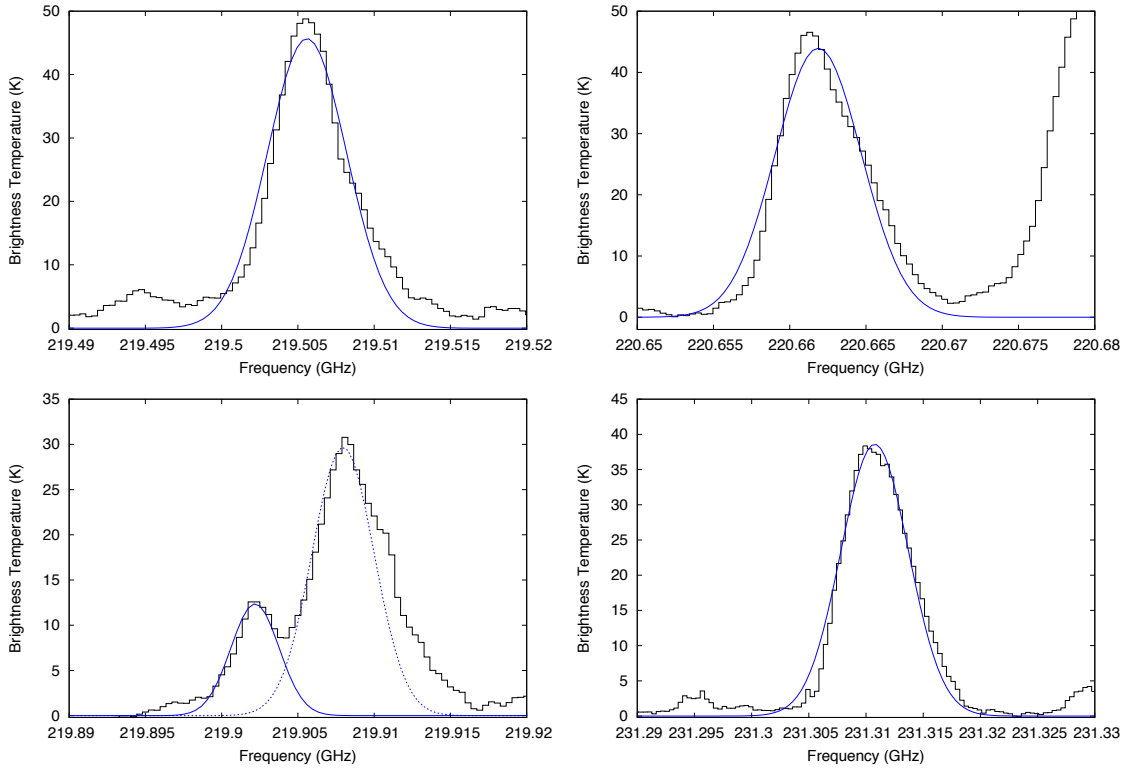

Figure 6.4: The spectra of four transitions of C_2H_5CN which are detected in the observations presented in this chapter. The solid lines are the fits to the transitions of C_2H_5CN, and the dashed line is the fit to the 3(1, 2) – 2(1, 1) transition of $H_2{}^{13}CO$.

6.2.3 Isocyanic acid (HNCO)

The 10(3, 8, 11) – 9(3, 7, 10) and 10(0, 10, 10) – 9(0, 9, 10) transitions of HNCO were detected and their moment maps determined in IRAS 17233–3606 by Leurini et al. (2011). Here we present the detection of a further four transitions of HNCO (Figure 6.5) with Gaussian fit and transitional information in Tables 6.6 and 6.7. The 10(4, 6, 9) – 9(4, 5, 8) transition is blended with at least two unidentified lines at 219.543 GHz and 219.550 GHz, which do pass the Rayleigh criterion. The 10(3, 8, 11) – 9(3, 7, 10) transition is severely blended with an unidentified transition, and this blend does not pass the Rayleigh criterion. We fit two Gaussians to this blend of different FWHMs in order to determine the $\int T\,dv$, and T_B of the 10(3, 8, 11) – 9(3, 7, 10) transition. As the transition is blended with an unknown transition which may trace a different gas temperature, the difference in FWHM is reasonable. Due to the severity of this blend, however, we omit this transition from column density calculations in Section 6.3. We also omit the 10(2, 9, 10) – 9(2, 8, 10) and

Table 6.5: Transitional information, including the quantum numbers, rest frequencies, upper energy levels, Einstein A coefficients, and upper state degeneracies, for the four transitions of C_2H_5CN detected in these observations.

Transition	Rest frequency (GHz)	E_u (K)	A (s^{-1})	g_u
24(2,22) – 23(2,21)	219.50559	136	8.87e−4	49
12(3,10) – 11(2,9)	219.90250	44	3.04e−5	25
25(2,24) – 24(2,23)	220.66092	143	9.01e−4	51
26(1,25) – 25(1,24)	231.31042	153	1.04e−3	53

Table 6.6: Velocity, integrated intensity, temperature brightness, FWHM, and rms information determined from a Gaussian fit for all six transitions of HNCO.

Frequency (GHz)	V_{LSR} (kms^{-1})	V_{peak} (kms^{-1})	$\int T\,dv$ ($Kkms^{-1}$)	FWHM (kms^{-1})	T_B (K)	rms (K)
219.54697	−3.40	−3.23	15.43 (4.29)	3.84 (0.29)	3.77 (0.77)	0.2
219.65696	−3.40	−2.65	44.05 (11.71)	5.54 (0.33)	7.47 (1.54)	0.2
219.73487	−3.40	−4.00	91.29 (32.44)	5.65 (0.31)	15.19 (4.56)	0.2
219.73714	−3.40	−4.22	100.73 (27.09)	5.00 (0.00)	18.93 (5.09)	0.2
219.79831	−3.40	−2.41	302.95 (67.57)	8.49 (0.19)	33.52 (6.73)	0.2
220.58501	−3.40	−2.79	479.71 (108.04)	9.04 (0.22)	49.83 (10.01)	0.2

10(2, 8, 9) – 9(2, 7, 9) transitions as they are heavily blended with several transitions of C_2H_3CN.

Table 6.7: Transitional information, including the quantum numbers, rest frequencies, upper energy levels, Einstein A coefficients, and upper state degeneracies, for the six transitions of HNCO detected in these observations.

Transition	Rest frequency (GHz)	E_u (K)	A (s^{-1})	g_u
10(4, 6, 9) – 9(4, 5, 8)	219.54709	750	1.25e−4	19
10(3, 8, 11) – 9(3, 7, 10)	219.65671	447	1.37e−4	23
10(2, 9, 10) – 9(2, 8, 10)	219.73443	231	1.45e−6	21
10(2, 8, 9) – 9(2, 7, 9)	219.73654	231	1.60e−6	19
10(0, 10, 10) – 9(0, 9, 10)	219.79903	58	1.51e−6	21
10(1, 9, 10) – 9(1, 8,10)	220.58546	102	1.51e−6	21

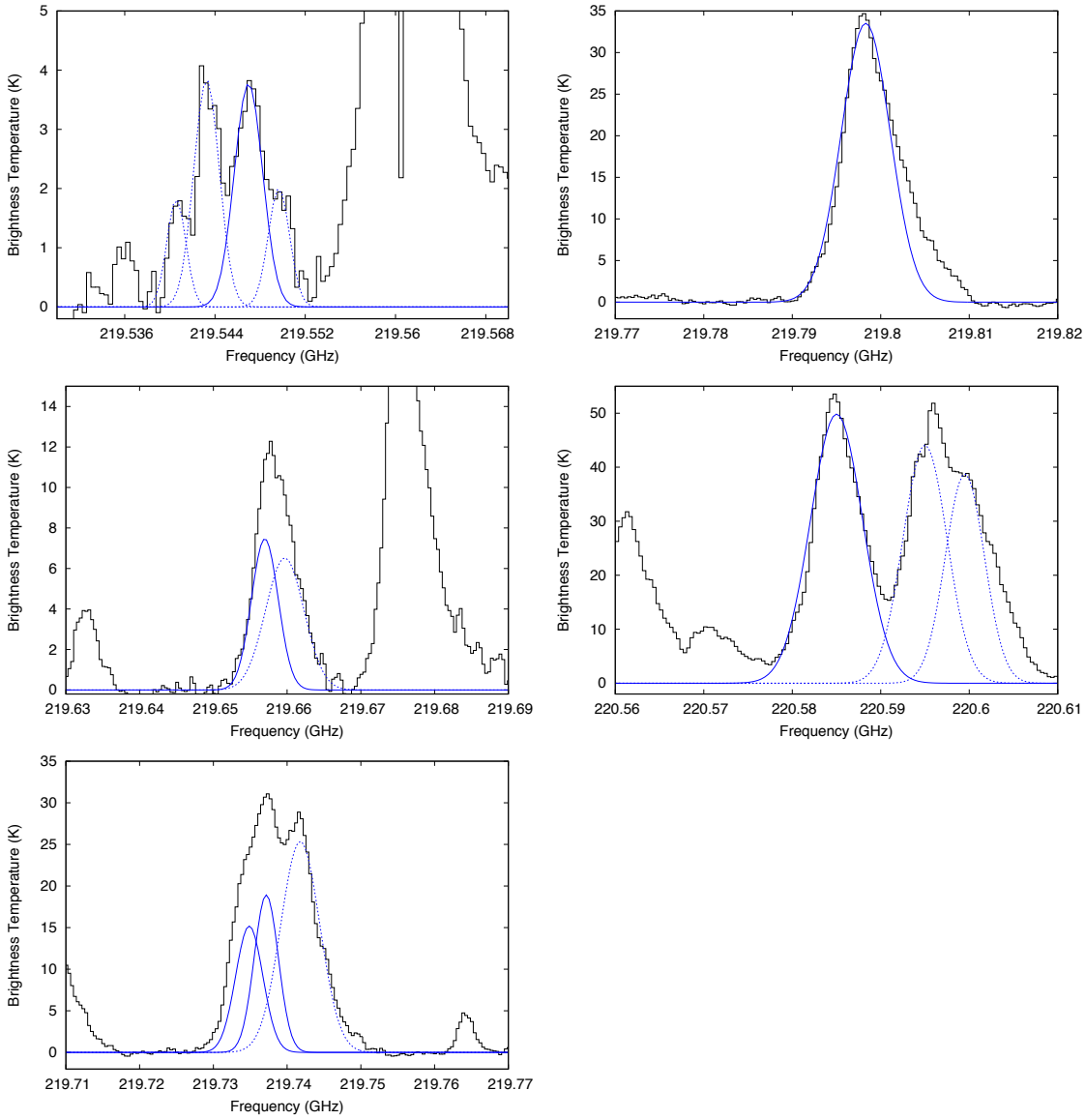

Figure 6.5: The spectra of six transitions of HNCO which are detected in the observations presented in this chapter. The solid lines are the fits to the HNCO lines and the dashed lines are the fits to the molecules HNCO is blended with.

6.2.4 Formaldehyde ($H_2{}^{13}CO$)

The 3(1, 2) – 2(1, 1) transition of $H_2{}^{13}CO$ is detected at 219.90796 GHz (Figure 6.6) but is partially blended with the 12(3,10) – 11(2,9) transition of C_2H_5CN at 219.90250 GHz. These transitions do pass the Rayleigh criterion, however, the profile of the of $H_2{}^{13}CO$ is non-Gaussian suggesting it may be contaminated with another molecule. Despite this, Gaussian fit and transitional information can be found in Tables 6.8 and 6.9. Further transitions of $H_2{}^{13}CO$ are required to confirm its presence in IRAS 17233–3606 and derive accurate column densities; however, values are calculated from this single transition in Section 6.3.

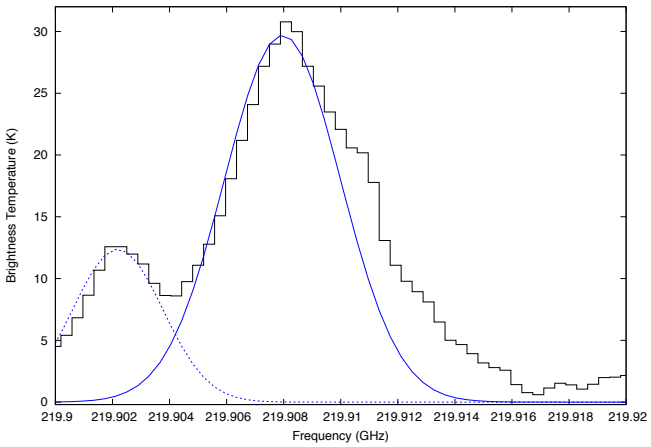

Figure 6.6: The spectra of the 3(1, 2) – 2(1, 1) transition of $H_2{}^{13}CO$. A Gaussian fit is represented by the solid line and the dashed line represents the fit of the unidentified transition it is blended with.

Table 6.8: Velocity, integrated intensity, temperature brightness, FWHM, and rms information determined from a Gaussian fit for the 3(1, 2) – 2(1, 1) transition of $H_2{}^{13}CO$.

Frequency (GHz)	V_{LSR} (kms^{-1})	V_{peak} (kms^{-1})	$\int T\,dv$ ($Kkms^{-1}$)	FWHM (kms^{-1})	T_B (K)	rms (K)
219.90796	−3.40	−2.62	196.93 (46.08)	6.23 (0.21)	29.69 (5.95)	0.2

6.2.5 Cyanoacetylene (HC_3N)

The 24(0) – 23(0) v_7=2 and 24(−2) – 23(2) v_7=2 transitions of HC_3N were detected and analysed in Leurini et al. (2011). We report the Gaussian fit and transitional information

Table 6.9: Transitional information, including the quantum number, rest frequency, upper energy level, Einstein A coefficient, and upper state degeneracy, for the 3(1, 2) – 2(1, 1) transition of $H_2{}^{13}CO$ detected in these observations.

Transition	Rest frequency (GHz)	E_u (K)	A (s^{-1})	g_u
3(1, 2) – 2(1, 1)	219.90853	33	0.00026	21

in Tables 6.10 and 6.11 for these transitions, as well as the 24(2) – 23(−2) v_7=2 transition identified in this work. The 24(2) – 23(−2) v_7=2 transition is heavily blended with transitions of HNCO and C_2H_3CN, and therefore the parameters derived from a Gaussian fit of the transition may not be accurate. For this reason this transition is excluded from the column density calculations in Section 6.3.

Table 6.10: Velocity, integrated intensity, temperature brightness, FWHM, and rms information determined from a Gaussian fit for all three transitions of HC_3N.

Frequency (GHz)	V_{LSR} (kms^{-1})	V_{peak} (kms^{-1})	$\int T\,dv$ ($Kkms^{-1}$)	FWHM (kms^{-1})	T_B (K)	rms (K)
219.67579	−3.40	−4.33	177.70 (44.40)	7.39 (0.34)	22.58 (4.61)	0.2
219.70726	−3.40	−3.26	161.45 (39.21)	8.28 (0.28)	18.33 (3.83)	0.2
219.74179	−3.40	−3.29	218.75 (67.55)	8.11 (0.55)	25.35 (6.11)	0.2

Table 6.11: Transitional information, including the quantum numbers, rest frequencies, upper energy levels, Einstein A coefficients, and upper state degeneracies, for the three transitions of HC_3N detected in these observations.

Transition	Rest frequency (GHz)	E_u (K)	A (s^{-1})	g_u
24(0) – 23(0) v_7=2	219.67511	773	0.00083	49
24(−2) – 23(2) v_7=2	219.70735	777	0.00083	49
24(2) – 23(−2) v_7=2	219.74187	777	0.00083	49

6.2.6 Methyl Formate ($HCOOCH_3$)

Methyl formate has been detected and analysed previously in IRAS 17233–3606 by Leurini et al. (2008). In these observations an additional eight transitions of v=0 methyl formate and seven transitions of v=1 methyl formate are detected (Figure 6.7). Parameters derived from a Gaussian fit of each transition can be found in Table 6.12 and transitional information can be found in Table 6.13. The emission of seven transitions is uncontaminated by the emission from other molecules; the remaining transitions are blended. The 17(4, 13, 0) – 16(4, 12, 0) transition is blended with an unidentified line at 220.194 GHz but they do pass the Rayleigh criterion. The 18(10, 9, 3) – 17(10, 8, 3) v=1 transition is blended with an unidentified line at 219.827 GHz, however, they do not pass the Rayleigh criterion. The 18(8, 10, 5) – 17(8, 9, 5) v=1 transition is partially blended with an unidentified line at 220.254 GHz, but they do pass the Rayleigh criterion. The 18(7, 12, 3) – 17(7, 11, 3) transition is blended with an unidentified line at 220.910 GHz, which do pass the Rayleigh criterion. In order to determine a realistic fit for the 18(7, 12, 3) – 17(7, 11, 3) transition, the FWHM and centre were fixed. The 18(16, 2, 0) – 17(16, 1, 0) v=0 transition is blended with an unidentified line at 220.930 GHz. The 18(14, 4, 0) – 17(14, 3, 0) v=0 is significantly blended with an unidentified line at 220.050 GHz and is therefore excluded from the rotation diagram analysis in Section 6.3. The 18(14, 5, 1) – 17(14, 4, 1) v=0 transition is heavily blended with several unidentified lines, and in order to generate a realistic fit for this transition, the centre and FWHM had to be fixed. Due to this severe blending this transition is also excluded from the rotation diagram analysis. The 18(8, 10, 5) – 17(8, 9, 5) v=1 transition suffers from some blending, however, a good fit was achieved by fixing the centre and FWHM, as well as fixing the FWHM of the other molecules it is blended with. The 18(8, 11, 4) – 17(8, 10, 4) v=1 transition is blended as part of a large mixture of emission from 221.109 GHz – 221.150 GHz. This region of emission is a combination of C_2H_3CN, $HCOOCH_3$, and CH_3CN emission as well as some unidentified features. Considering the weakness (1.61 K) of the $HCOOCH_3$ component compared to the other molecules, an accurate Gaussian fit has been difficult, but can be found in Figure 6.7. We do, however, exclude this transition from the rotational diagram analysis (see Section 6.3). The differences between the rest frequencies and the observational frequency of each of these transitions is within the observational frequency error.

Table 6.12: Velocity, integrated intensity, temperature brightness, FWHM, and rms information determined from a Gaussian fit for all fifteen transitions of $HCOOCH_3$.

Frequency (GHz)	V_{LSR} (kms^{-1})	V_{peak} (kms^{-1})	$\int T\,dv$ ($Kkms^{-1}$)	FWHM (kms^{-1})	T_B (K)	rms (K)
219.76407	−3.40	−3.60	16.15 (3.78)	3.26 (0.10)	4.66 (0.94)	0.2
219.82216	−3.40	−3.43	7.11 (2.49)	2.58 (0.31)	2.59 (0.60)	0.2
220.03065	−3.40	−3.80	16.61 (4.54)	5.07 (0.32)	3.08 (0.65)	0.2
220.16705	−3.40	−3.62	73.47 (15.58)	5.00 (0.00)	13.80 (2.93)	0.2
220.19026	−3.40	−3.37	57.29 (18.36)	4.30 (0.50)	12.53 (2.55)	0.2
220.25829	−3.40	−3.66	22.88 (4.64)	4.00 (0.00)	5.37 (1.09)	0.2
220.30801	−3.40	−4.30	3.58 (1.64)	2.90 (0.55)	1.16 (0.31)	0.2
220.91372	−3.40	−3.08	24.78 (5.33)	4.25 (0.00)	5.48 (1.18)	0.2
220.92682	−3.40	−4.02	10.81 (3.40)	3.15 (0.22)	3.23 (0.79)	0.2
220.94685	−3.40	−4.10	12.67 (3.57)	4.81 (0.34)	2.47 (0.52)	0.2
221.04829	−3.40	−4.07	15.01 (4.33)	3.68 (0.26)	3.83 (0.84)	0.2
221.06753	−3.40	−4.21	11.81 (0.97)	5.00 (0.00)	2.21 (0.59)	0.2
221.11063	−3.40	−3.35	3.06 (8.01)	3.00 (0.00)	0.96 (2.51)	0.2
221.15841	−3.40	−3.20	26.06 (6.30)	5.19 (0.20)	4.71 (0.96)	0.2
231.01905	−3.40	−3.46	3.12 (1.42)	2.85 (0.44)	1.03 (0.27)	0.3

Table 6.13: Transitional information, including the quantum numbers, rest frequencies, upper energy levels, Einstein A coefficients, and upper state degeneracies, for all fifteen transition of $HCOOCH_3$ detected in these observations.

Transition	Rest frequency (GHz)	E_u (K)	A (s^{-1})	g_u
18(9, 9, 5) – 17(9, 8, 5) v=1	219.76395	342	1.20e−4	74
18(10, 9, 3) – 17(10, 8, 3) v=1	219.82213	355	1.11e−4	74
18(9, 10, 3) – 17(9, 9, 3) v=1	220.03034	342	1.20e−4	74
17(4, 13, 2) – 16(4, 12, 2) v=0	220.16689	103	1.52e−4	70
17(4, 13, 0) – 16(4, 12, 0) v=0	220.19028	103	1.52e−4	70
18(8, 10, 5) – 17(8, 9, 5) v=1	220.25810	331	1.29e−4	74
18(10, 9, 4) – 17(10, 8, 4) v=1	220.30738	354	1.12e−4	74
18(7, 12, 3) – 17(7, 11, 3) v=1	220.91396	321	1.38e−4	74
18(16, 2, 0) – 17(16, 1, 0) v=0	220.92636	271	3.42e−5	74
18(7, 11, 3) – 17(7, 10, 3) v=0	220.94635	321	1.38e−4	74
18(14, 4, 0) – 17(14, 3, 0) v=0	221.04779	231	6.40e−5	74
18(14, 5, 1) – 17(14, 4, 1) v=0	221.06693	231	6.45e−5	74
18(8, 11, 4) – 17(8, 10, 4) v=1	221.11067	330	1.31e−4	74
18(13, 6, 1) – 17(13, 5, 1) v=0	221.15854	213	7.82e−5	74
12(4, 9, 1) – 11(3, 8, 2) v=0	231.01900	57	1.03e−5	50

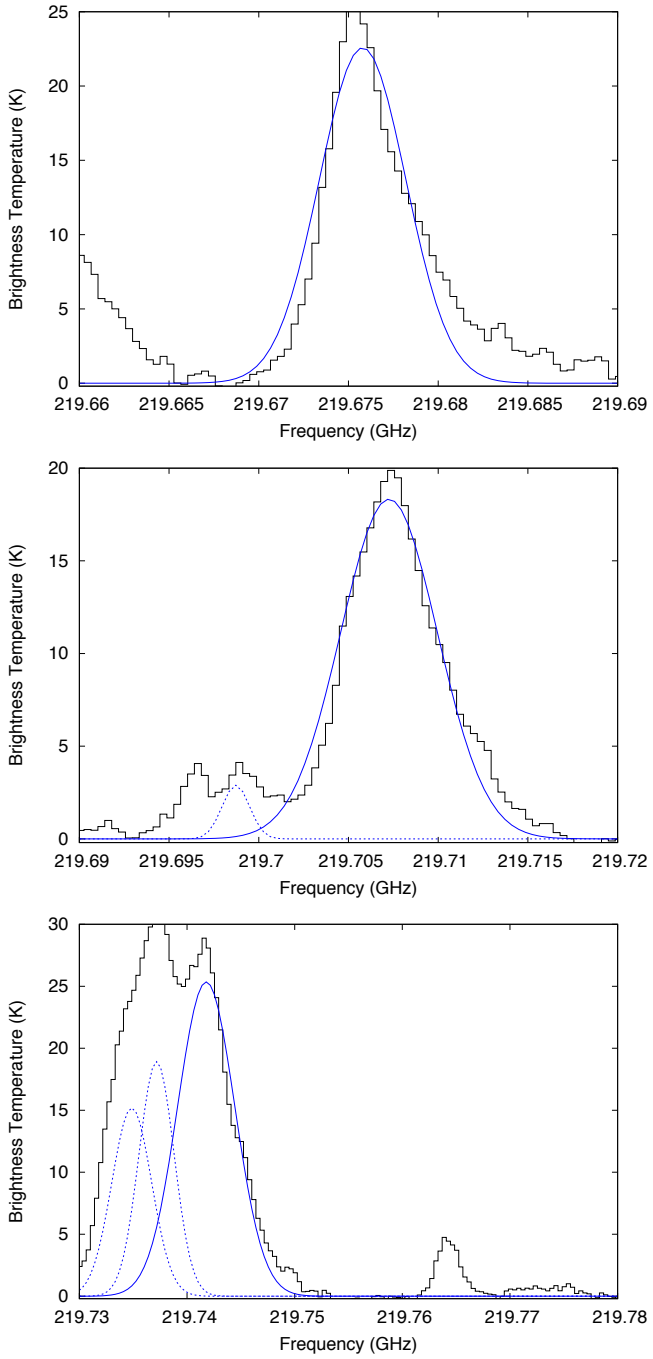

Figure 6.7: The spectra of three transitions of HC_3N which are detected in these observations. The Gaussian fit of the HC_3N emission is represented by the solid lines, and the dashed lines represent the fit of the molecular transitions that HC_3N is blended with.

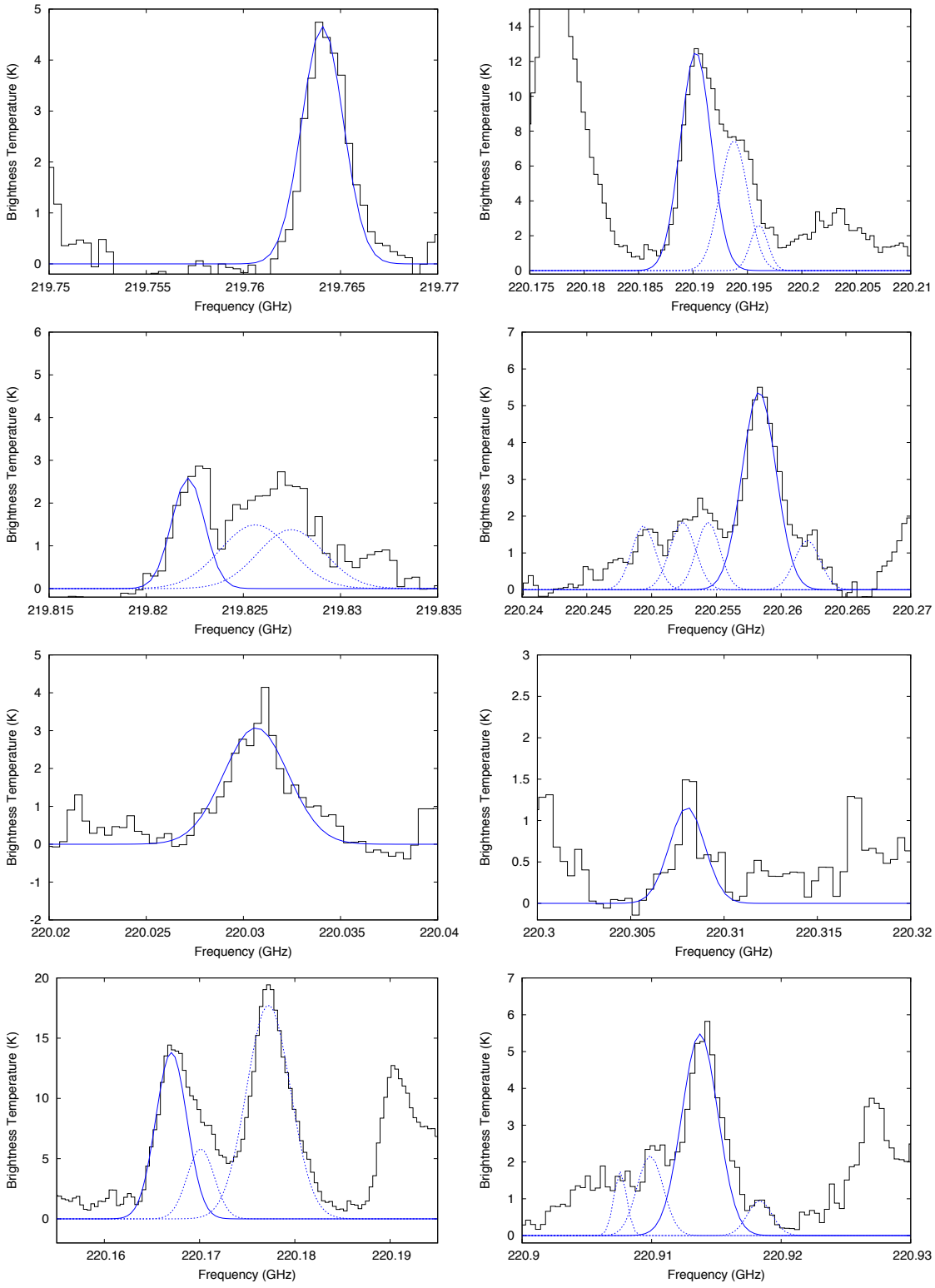
Brightness Temperature (K)
Frequency (GHz)
219.75 219.755 219.76 219.765 219.77
220.175 220.18 220.185 220.19 220.195 220.2 220.205 220.21
219.815 219.82 219.825 219.83 219.835
220.24 220.245 220.25 220.255 220.26 220.265 220.27
220.02 220.025 220.03 220.035 220.04
220.3 220.305 220.31 220.315 220.32
220.16 220.17 220.18 220.19
220.9 220.91 220.92 220.93

(a)

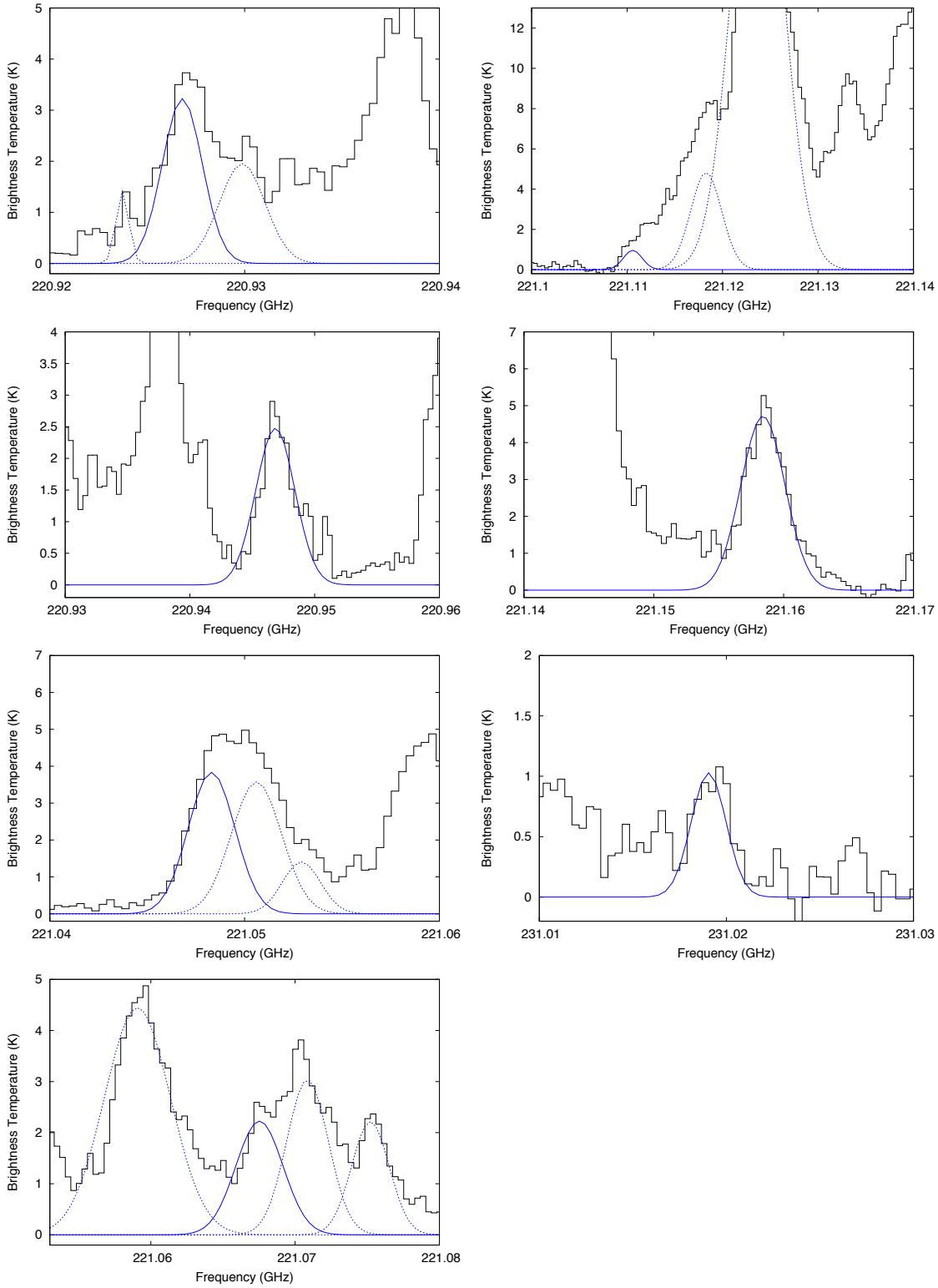

(b)

Figure 6.7: Spectra of the fifteen transitions of $HCOOCH_3$ detected in these observations. The Gaussian fits to transitions of $HCOOCH_3$ are represented by the solid lines, and the dashed lines represent the fit of the molecular transitions that $HCOOCH_3$ is blended with.

6.2.7 Acetone (CH_3COCH_3)

In these observations we detect seven transitions of acetone for the first time in IRAS 17233–3606 (Figure 6.8). Parameters derived from a Gaussian fit of each transition can be found in Table 6.14 and transitional information can be found in Table 6.15. The 22(1, 22) – 21(1, 21)AE v=0, 22(0, 22) – 21(1, 21)EE v=0 and 22(1, 22) – 21(1, 21)AA v=0 transitions are blended with each other. In order to generate a realistic fit for these transitions the centre and FWHM was fixed. This produced a reasonable fit to these transitions, however, it is difficult to rule out contamination from unidentified transitions within this blend. The 22(0, 22) – 21(1, 21)EE v=0 and 22(1, 22) – 21(1, 21)AA v=0 transitions do not pass the Rayleigh criterion. The 46(20, 26) – 46(19, 27)EE v=0 transition is blended with unknown emission at 220.470 GHz. Due the severe blending seen with this transition it was necessary to fix the centre and the FWHM in order to produce a realistic fit. The 16(8, 8) – 15(9, 7)EE v=0 transition is slightly blended with an unidentified transition at 230.286 GHz. The 27(1, 26) – 27(1, 27)EE v=0 transition is blended with an unidentified line at 230.413 GHz, and in order to generate a realistic fit the centre and FWHM parameters were fixed.

Table 6.14: Velocity, integrated intensity, temperature brightness, FWHM, and rms information determined from a Gaussian fit for all seven transitions of CH_3COCH_3.

Frequency (GHz)	V_{LSR} (kms^{-1})	V_{peak} (kms^{-1})	$\int T\,dv$ ($Kkms^{-1}$)	FWHM (kms^{-1})	T_B (K)	rms (K)
220.35544	−3.40	−3.48	38.19 (8.92)	4.50 (0.00)	7.97 (1.86)	0.2
220.36236	−3.40	−3.97	53.19 (11.80)	5.00 (0.00)	9.99 (2.22)	0.2
220.36851	−3.40	−3.66	70.60 (19.67)	8.27 (0.38)	8.00 (1.87)	0.2
220.46697	−3.40	−4.61	13.58 (12.60)	4.32 (0.00)	2.95 (1.44)	0.2
220.76240	−3.40	−1.70	60.66 (28.96)	6.88 (0.50)	8.28 (3.35)	0.2
220.96234	−3.40	−2.40	50.38 (11.72)	7.76 (0.22)	6.10 (1.25)	0.2
230.41116	−3.40	−2.30	0.76 (0.40)	1.50 (0.00)	0.48 (0.25)	0.3

6.2.8 Methyl Isocyniade (CH_3NC)

Five transitions of methyl isoyanide are detected in these observations (Figure 6.9). The 221.012 GHz transition suffers from minimal blending, however, the line profile is poorly represented by a Gaussian, and hence required the FWHM and centre to be fixed in order to generate a realistic fit. The transition at 221.093 GHz does not suffer from significant

Table 6.15: Transitional information, including the quantum numbers, rest frequencies, upper energy levels, Einstein A coefficients, and upper state degeneracies, for all seven transition of CH_3COCH_3 detected in these observations.

Transition	Rest frequency (GHz)	E_u (K)	A (s^{-1})	g_u
22(1, 22) – 21(1, 21)AE v=0	220.35538	124	5.08e−4	90
22(0, 22) – 21(1, 21)EE v=0	220.36188	124	4.17e−3	20
22(1, 22) – 21(1, 21)AA v=0	220.36832	124	5.08e−4	70
46(20, 26) – 46(19, 27)EE v=0	220.46608	816	3.63e−3	99
11(11, 0) – 10(10, 0)EE v=0	220 763.62	63	2.54e−3	68
11(11, 0) – 10(10, 1)AA v=0	220.96310	63	4.72e−4	30
27(1, 26) – 27(1, 27)EE v=0	230.41201	195	1.20e−5	80

blending. The transitions at 221.118 GHz, 221.133 GHz, and 221.139 GHz are part of a large region of blended emission. The blending is very servere for the 221.118 GHz and 221.139 GHz transitions, and are therefore excluded from the rotation diagram analysis below. Parameters derived from a Gaussian fit and transitional information can be found in Tables 6.16 and 6.17. This is the first detection of this molecule in IRAS 17233–3606.

Table 6.16: Velocity, integrated intensity, temperature brightness, FWHM, and rms information determined from a Gaussian fit of five transitions of CH_3NC.

Frequency (GHz)	V_{LSR} (kms^{-1})	V_{peak} (kms^{-1})	$\int T\,dv$ ($Kkms^{-1}$)	FWHM (kms^{-1})	T_B (K)	rms (K)
221.01297	−3.40	−2.88	4.50 (3.63)	2.42 (0.92)	1.75 (0.74)	0.2
221.09291	−3.40	−2.84	43.48 (10.70)	6.38 (0.23)	6.40 (1.35)	0.2
221.11826	−3.40	−3.33	25.61 (15.44)	5.00 (0.00)	4.81 (2.68)	0.2
221.13292	−3.40	−2.88	56.50 (19.57)	5.00 (0.00)	10.62 (3.68)	0.2
221.13908	−3.40	−4.46	36.03 (17.53)	5.00 (0.00)	6.77 (3.29)	0.2

Table 6.17: Transitional information, including the quantum numbers, rest frequencies, upper energy levels, Einstein A coefficients, and upper state degeneracies, for transitions of CH_3NC.

Transition	Rest frequency (GHz)	E_u (K)	A (s^{-1})	g_u
11(5) – 10(5)	221.01338	240	7.2e−4	46
11(3) – 10(3)	221.09332	127	8.4e−4	92
11(2) – 10(2)	221.11831	92	8.8e−4	46
11(1) – 10(1)	221.13330	71	9.0e−4	46
11(0) – 10(0)	221.13829	64	9.1e−4	46

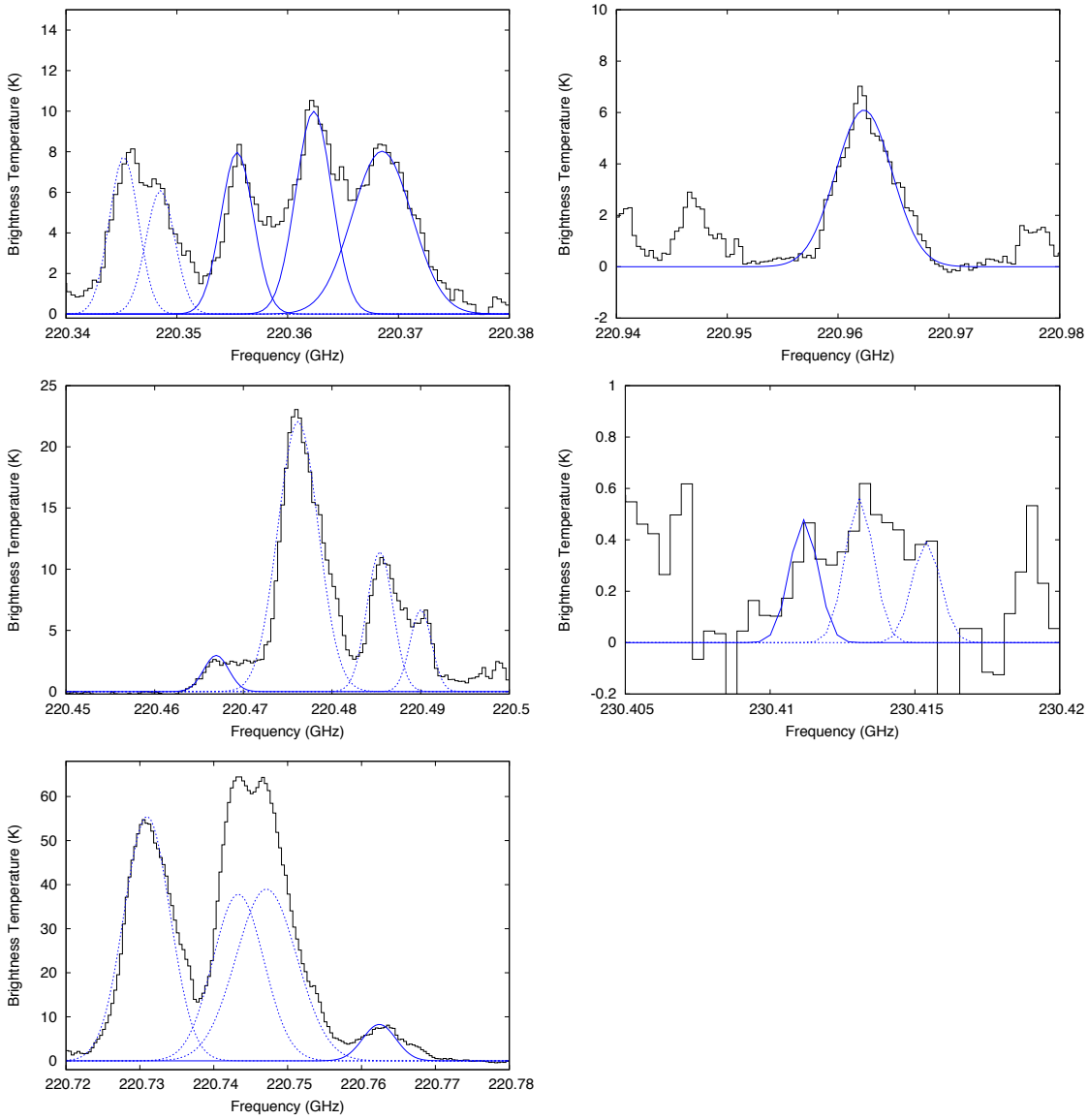

Figure 6.8: Spectra of the seven transitions of CH_3COCH_3 detected in these observations. The Gaussian fits to transitions of CH_3COCH_3 are represented by the solid lines, and the dashed lines represent the fit of the molecular transitions that CH_3COCH_3 is blended with.

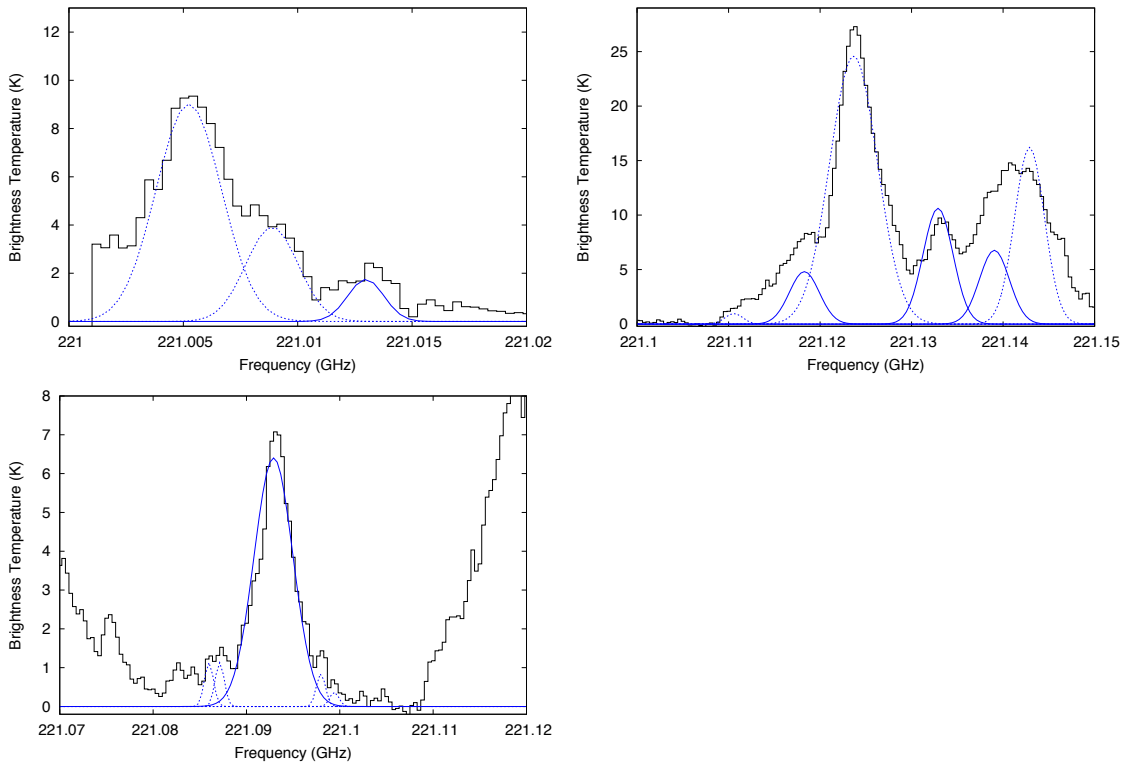

Figure 6.9: Spectra of the five detected transitions of CH_3NC detected in these observations. The Gaussian fits to transitions of CH_3NC are represented by the solid lines, and the dashed lines represent the fits to the molecular transitions that CH_3NC is blended with.

Table 6.18: Velocity, integrated intensity, temperature brightness, FWHM, and rms information determined from a Gaussian fit of transitions of CH_3OH.

Frequency (GHz)	V_{LSR} (kms^{-1})	V_{peak} (kms^{-1})	$\int T\,dv$ ($Kkms^{-1}$)	FWHM (kms^{-1})	T_B (K)	rms (K)
220.07908	−3.40	−4.20	261.23 (59.59)	6.82 (0.19)	35.98 (7.21)	0.2
229.58939	−3.40	−3.80	172.72 (37.06)	7.81 (0.11)	20.78 (4.17)	0.3
229.75862	−3.40	−3.20	488.26 (105.87)	7.99 (0.13)	57.43 (11.51)	0.3
229.93935	−3.40	−3.60	33.18 (9.04)	7.06 (0.45)	4.42 (0.92)	0.3
230.02731	−3.40	−3.70	138.19 (33.65)	8.90 (0.36)	14.58 (2.96)	0.3
230.29318	−3.40	−4.00	6.53 (3.83)	5.87 (2.04)	1.04 (0.25)	0.3
230.36788	−3.40	−2.98	19.90 (6.16)	5.11 (0.50)	3.66 (0.77)	0.3
231.28136	−3.40	−3.70	179.23 (39.98)	7.69 (0.17)	21.90 (4.40)	0.3

6.2.9 Methanol (CH_3OH)

The 8(0, 8) – 7(1, 6), 8(−1, 8) – 7(0, 7) and 10(2, 9) – 9(3, 6) transitions have been detected and analysed previously by Leurini et al. (2011). Here we present the identification and analysis of a further six transitions of CH_3OH and one transition of $^{13}CH_3OH$ (Figures 6.10 and 6.11). Parameters derived from a Gaussian fit and transitional information for each transition can be found in Tables 6.18, 6.20, 6.19 and 6.21. The 3(−2, 2) – 4(−1, 4) transition exhibits a degree of self-absorption most likely due to contamination from the outflows in the region, and is therefore excluded from the rotation diagram analysis below. The 22(4, 18) – 21(5, 17) transition is within a region where there are at least five transitions blended with each other. This means a reasonable fit was only possible by fixing the centre and FWHM of the CH_3OH transition as well as those of the molecules that this transition is blended with. The 8(−1, 8, 0) – 7(0, 7, 0) vt=0,1 transition of $^{13}CH_3OH$ also required the centre and FWHM to be fixed in order to achieve a good fit.

Table 6.19: Transitional information, including the quantum numbers, rest frequencies, upper energy levels, Einstein A coefficients, and upper state degeneracies, for all seven transition of CH_3OH detected in these observations.

Transition	Rest frequency (GHz)	E_u (K)	A (s^{-1})	g_u
8(0, 8) – 7(1, 6)	220.07849	97	2.52e−5	17
15(4, 11) – 16(3, 13)	229.58907	374	2.08e−5	31
8(−1, 8) – 7(0, 7)	229.75876	89	4.19e−5	17
19(5, 15) – 20(4, 16)	229.93918	579	2.07e−5	39
3(−2, 2) – 4(−1, 4)	230.02706	40	1.49e−5	7
22(4, 18) – 21(5, 17)	230.36820	683	2.08e−5	45
10(2, 9) – 9(3, 6)	231.28110	165	1.84e−5	21

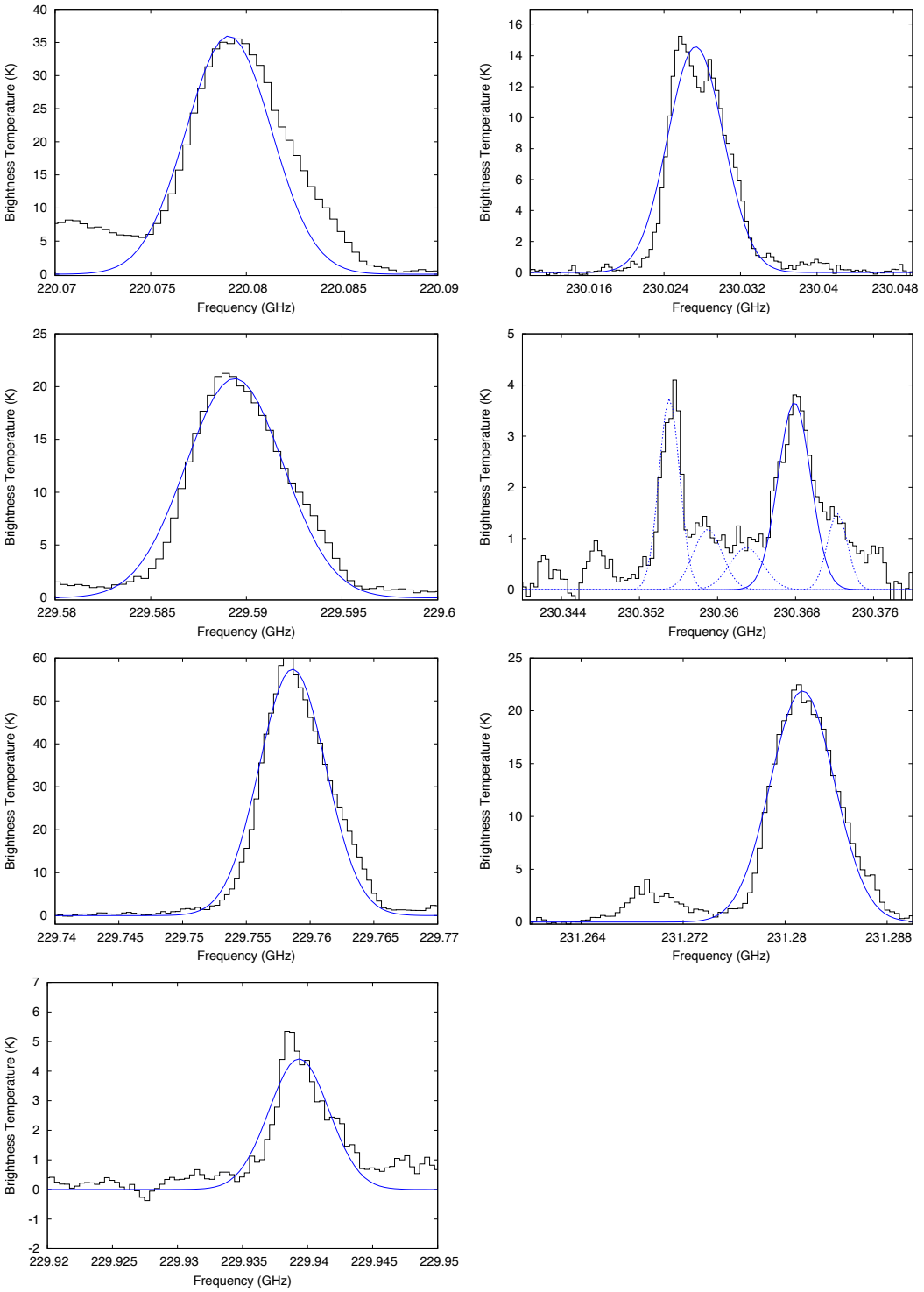

Figure 6.10: Spectra of the seven detected transitions of CH_3OH represented by the solid lines. The dashed lines represent the fits to the molecular transitions that CH_3OH is blended with.

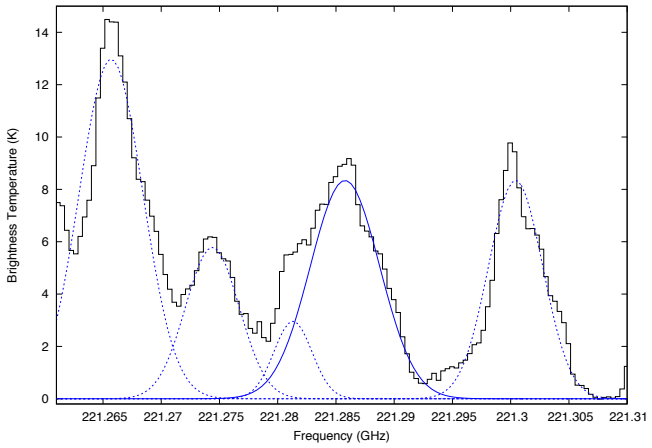

Figure 6.11: Spectra of the $^{13}CH_3OH$ transition detected in these observations. The solid line represents the fit to $^{13}CH_3OH$ and the dashed lines represent the fits for the molecular transitions $^{13}CH_3OH$ is blended with.

Table 6.20: Velocity, integrated intensity, temperature brightness, FWHM, and rms information determined from a Gaussian fit for transitions of $^{13}CH_3OH$.

Frequency (GHz)	V_{LSR} (kms^{-1})	V_{peak} (kms^{-1})	$\int T\,dv$ (Kkms^{-1})	FWHM (kms^{-1})	T_B (K)	rms (K)
221.28577	−3.40	−4.12 (0.38)	81.05 (25.69)	9.13 (0.87)	8.34 (1.85)	0.2

6.2.10 Vinyl cyanide (C_2H_3CN)

In these observations we detect fourteen transitions of C_2H_3CN and one transition of $C_2H_3{}^{13}CN$ in IRAS 17233–3606. Parameters derived from a Gaussian fit and transitional information for each transition can be found in Tables 6.22, 6.24, 6.23 and 6.25. Figures 6.12, and 6.13 show the fits overlaid on the spectra. Many of the transitions are severly blended with other molecular transitions within the spectra that remain unidentified. Where possible a Gaussian fit has been derived by allowing CLASS to vary the T_{peak},

Table 6.21: Transitional information, including the quantum numbers, rest frequencies, upper energy levels, Einstein A coefficients, and upper state degeneracies, for the 8(-1, 8, 0) – 7(0, 7, 0) transition of $^{13}CH_3OH$ detected in these observations.

Transition	Rest frequency (GHz)	E_u (K)	A (s^{-1})	g_u
8(−1, 8, 0) – 7(0, 7, 0) vt=0,1	221.28524	87	3.72e−5	17

centre and FWHM until a reasonable fit is generated. In some cases it was necessary to fix the centre and the FWHM and vary the parameters manually until a good fit was found. For the transitions at 230.106, 230.808, 230.841, 230.951, 231.101, and 231.145 GHz, a realistic fit could not be generated due to severe blending. These transitions are excluded from further anlysis. The 23(1, 22, 0, 23) – 22(1, 21, 0, 22) v11=0 transition is partially blended with CH_3NC emission and in order to achieve a good fit the FWHM and centre were fixed. The 25(0, 25, 0, 25) – 24(0, 24, 0, 24) v11=0 transition is blended with an unidentified line at 230.743 GHz, but a fit was achieved by allowing CLASS to vary all parameters. This fit is therefore more reliable and has more realistic errors associated with it. The 25(0, 25, 2, 25) – 24(0, 24, 2, 24) v15=1 transition is blended with an unidentified transition at 231.233 GHz, and the FWHM and centre had to be fixed in order to achieve a good fit.

Table 6.22: Velocity, integrated intensity, temperature brightness, FWHM, and rms information determined from a Gaussian fit of C_2H_3CN transitions.

Frequency (GHz)	V_{LSR} (kms^{-1})	V_{peak} (kms^{-1})	$\int T\,dv$ ($Kkms^{-1}$)	FWHM (kms^{-1})	T_B (K)	rms (K)
220.13802	−3.40	−3.50	31.83 (8.44)	5.49 (0.32)	5.45 (1.13)	0.2
220.56116	−3.40	−3.07	195.80 (50.92)	6.03 (0.35)	30.50 (6.16)	0.2
221.00524	−3.40	−3.43	42.04 (11.66)	4.39 (0.28)	9.02 (1.92)	0.2
221.12367	−3.40	−3.14	208.67 (60.68)	7.98 (0.53)	24.56 (5.51)	0.2
229.64734	−3.40	−2.70	182.86 (41.64)	7.25 (0.19)	23.71 (4.77)	0.3
230.10506	−3.40	−1.70	33.84 (8.81)	5.26 (0.30)	6.04 (1.23)	0.3
230.48697	−3.40	−2.10	183.08 (43.18)	7.44 (0.26)	23.11 (4.68)	0.3
230.73745	−3.40	−1.96	145.06 (33.46)	5.46 (0.16)	24.97 (5.03)	0.3
231.14456	−3.40	−1.90	35.41 (10.09)	6.66 (0.49)	5.00 (1.05)	0.3
231.23591	−3.40	−4.15	13.18 (3.46)	3.60 (0.00)	3.44 (0.90)	0.3

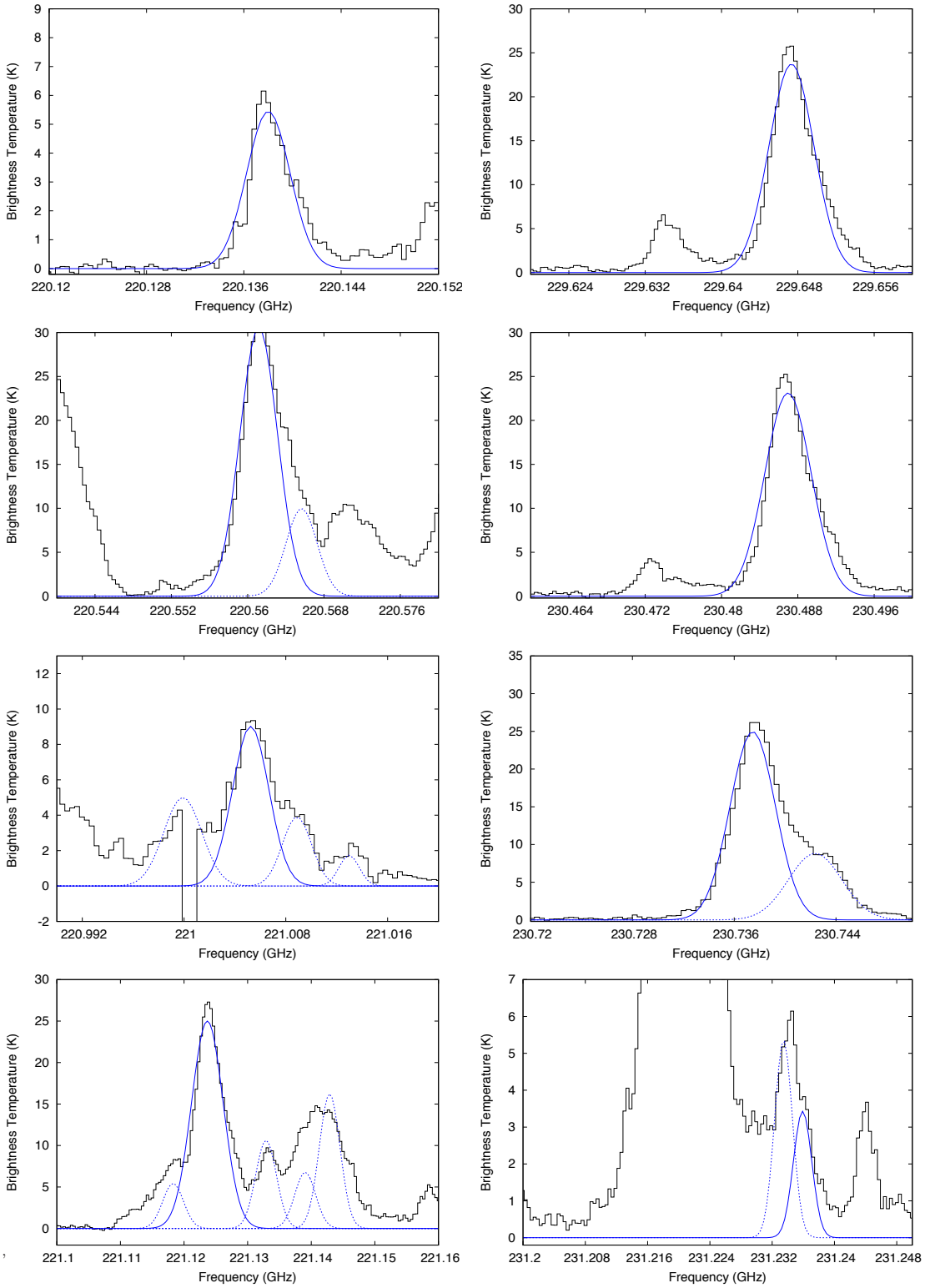

(a)

Figure 6.12: Spectra of the eight transitions of C_2H_3CN that a realistic Gaussian fit could be derived for. The solid lines represent the fits to the transitions of C_2H_3CN and the dashed lines represent fits to blended emission from other molecules.

Table 6.23: Transitional information, including the quantum numbers, rest frequencies, upper energy levels, Einstein A coefficients, and upper state degeneracies, for all transitions of C_2H_3CN detected in these observations.

Transition	Rest frequency (GHz)	E_u (K)	A (s^{-1})	g_u
23 (3, 20, 1, 24) – 22 (3, 19, 1, 23) v11=1	220.13795	490	8.69e−4	141
24 (1, 24, 0, 25) – 23 (1, 23, 0, 24) v11=0	220.56140	135	8.88e−4	147
24 (1, 24, 1, 25) – 23 (1, 23, 1, 24) v11=0	221.00522	479	8.83e−4	147
23 (1, 22, 0, 23) – 22 (1, 21, 0, 22) v11=0	221.12386	130	8.82e−4	141
25 (1, 25, 0, 26) – 24 (1, 24, 0, 25) v11=0	229.64784	146	9.92e−4	153
36 (3, 34, 0, 36) – 37 (0, 37, 0, 37) v11=1	230.10638	323	4.12e−7	219
24 (1, 23, 0, 24) – 23 (1, 22, 0, 24) v11=0	230.48794	141	1.00e−3	147
25 (0, 25, 0, 25) – 24 (0, 24, 0, 24) v11=0	230.73856	146	1.01e−3	153
24 (1, 24, 0, 24) – 23 (0, 23, 0, 23) v11=0	230.80837	135	4.19e−5	147
24 (1, 23, 2, 24) – 23 (1, 22, 2, 23) v15=1	230.84143	631	1.00e−3	147
19 (3, 17, 0, 18) – 19 (2, 18, 0, 18) v11=0	230.95145	106	2.90e−5	117
24 (1, 23, 1, 25) – 23 (1, 22, 1, 24) v11=1	231.10116	486	1.01e−3	147
25 (0, 25, 1, 25) – 24 (0, 24, 1, 24) v11=1	231.14571	490	1.01e−3	153
25 (0, 25, 2, 25) – 24 (0, 24, 2, 24) v15=1	231.23533	635	1.01e−3	153

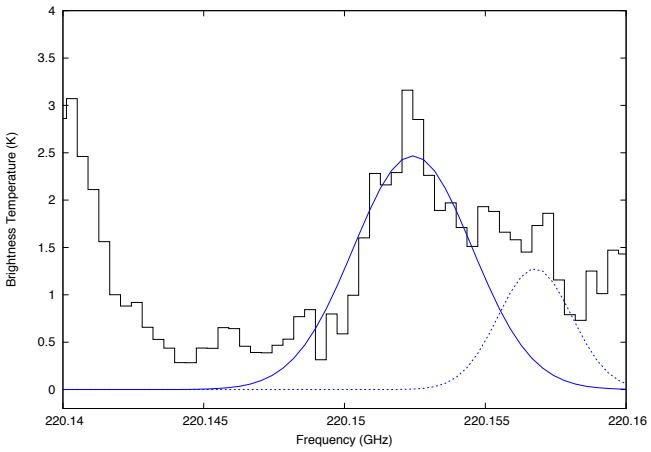

Figure 6.13: Spectra of the 23(1, 22) – 22(1, 21) transition of $C_2H_3{}^{13}CN$. The solid line represents the fit to the transition of $C_2H_3{}^{13}CN$ and the dashed line represents the fit for the unidentified blended transition.

6.3 Column densities and rotation temperatures

In this section we use the rotation diagram method as detailed in Chapter 3, to determine the column densities and rotation temperatures of the molecular emission identified in these observations. For molecules where only one transition is identified, we compute a

Table 6.24: Velocity, integrated intensity, temperature brightness, FWHM, and rms information determined from a Gaussian fit of the 23(1, 22) – 22(1, 21) transition of $C_2H_3{}^{13}CN$.

Frequency (GHz)	V_{LSR} (kms^{-1})	V_{peak} (kms^{-1})	$\int T\,dv$ ($Kkms^{-1}$)	FWHM (kms^{-1})	T_B (K)	rms (K)
220.15243	−3.40	−3.65	16.96 (1.24)	6.46 (0.60)	2.47 (0.31)	0.2

Table 6.25: Transitional information, including the quantum number, rest frequency, upper energy level, Einstein A coefficient, and upper state degeneracy, for the 23(1, 22) – 22(1, 21) transition of $C_2H_3{}^{13}CN$ detected in these observations.

Transition	Rest frequency (GHz)	E_u (K)	A (s^{-1})	g_u
23(1, 22) – 22(1, 21)	220.15252	130	8.82e−4	47

column density from a single transition at 300 K. Table 6.26 contains the column densities for DC_3N, C_2H_5CN, HNCO, $H_2{}^{13}CO$, HC3N, $HCOOCH_3$, CH_3COCH_3, CH_3NC, CH_3OH, and C_2H_3CN assuming LTE and optically thin emission. Figures 6.14 – 6.20 show the rotation diagrams for C_2H_5CN, HNCO, $HCOOCH_3$, CH_3COCH_3, CH_3NC, CH_3OH, and C_2H_3CN. In the case of HC_3N we are unable to determine a rotation temperature and column density from a rotation diagram, as the two transitions we detect in these observations are too close in upper energy level. We instead determine the column density from the parameters derived for only the 24(0) – 23(0) v_7=2 transition of HC_3N. We also compute a ratio of deuterium to hydrogen of 0.08, using the column densities of HC_3N and DC_3N. This value is enhanced compared to the standard interstellar value of 1.5×10^{-5}. Chemical modelling by Awad et al. (2014) found that an enhanced deuterium fractionation is found in high density hot cores or when there is a high depletion factor. However, as we only detect one transition of a deuterated species a further analysis is beyond the scope of this chapter. The rotation diagram for C_2H_3CN (Figure 6.20) indicates that v=0 and v=1 transitions may trace different temperature and density components in IRAS 17233–3606. Further detections of v=1 transitions are needed, however, to confirm multiple components in the rotation diagram.

In Table 6.27 we include the column densities derived for G31, G29, G19, G24A1, and G24A2 in Chapter 3, for molecules that have been detected in IRAS 17233–3606. IRAS 17233–3606 is the richest spectral source studied in this thesis. We find for some species,

such as HNCO, the column density is an order of magnitude higher in IRAS 17233–3606 than in G31. For other species, such as $HCOOCH_3$ and C_2H_3CN, column densities peak in G31. The 12 – 11 K ladders of CH_3CN and $CH_3{}^{13}CN$ were detected and analysed by Leurini et al. (2011) and Leurini et al. (2008), and found a column density of $4{\times}10^{16}$ cm^{-2} with an excitation temperature of 150 K, determined from modelling. This value is of the same order of magnitude as CH_3CN column densities found in G24A1 and an order of magnitude lower than those found in G31.

Table 6.26: Column densities (cm^{-2}) of the molecules identified in these observations in IRAS 17233–3606 calculated at their rotation temperatures, assuming LTE and optically thin emission. For DC_3N and $H_2{}^{13}CO$ the column density is computed at 300 K as only a single transition is detected. For HC_3N the column density is also computed at 300 K as the upper energy levels of the detected transitions are too close to derive a rotation temperature.

DC_3N†	C_2H_5CN	HNCO	$H_2{}^{13}CO$
4.37 (0.36)$\times10^{13}$	4.40 (0.35)$\times10^{16}$	3.45 (0.18)$\times10^{17}$	6.60 (0.23)$\times10^{17}$
HC_3N†	$HCOOCH_3$	CH_3COCH_3	CH_3NC
5.62 (0.25)$\times10^{14}$	5.86 (0.22)$\times10^{16}$	1.70 (0.22)$\times10^{18}$	3.65 (0.59)$\times10^{14}$
CH_3OH	C_2H_3CN		
5.82 (0.14)$\times10^{17}$	4.24 (0.15)$\times10^{16}$		

Using the rotation diagram method we are able to estimate rotation temperatures for species where we detect more than one transition; we assume the source fills the beam for all species. Table 6.28 shows the rotation temperatures for C_2H_5CN, HNCO, $HCOOCH_3$, CH_3COCH_3, CH_3NC, CH_3OH, and C_2H_3CN in IRAS 17233–3606. The rotation temperature we determine for C_2H_5CN is very low at 44 K, and hence indicates this molecule either traces a particularly cold subcondensation, or that the assumption of optically thin emission breaks down (Goldsmith & Langer 1999). HNCO and CH_3NC have far lower rotation temperatures compared to CH_3OH, $HCOOCH_3$, CH_3COCH_3, and C_2H_3CN. This suggests that either HNCO and CH_3NC trace a colder region or they represent a lower limit to the rotation temperature, and hence the column densities for these molecules would be a lower limit. We do note, however, that the error on the CH_3NC transition with an upper energy level of 240 K is very large, and if it were found to have a value at the upper end of its error range, the rotation temperature derived for CH_3NC would be comparable to the rotation temperatures for CH_3COCH_3.

Table 6.27: Column densities (cm^{-2}) of the organic molecules detected in Chapter 2, assuming LTE and optical thinness. The associated error for each column density is in brackets. For molecules where only a single transition has been detected the column densities listed are calculated at 300 K. For molecules where a rotation temperature is known, the column densities are computed at that temperature.

Object	C_2H_3CN	DCO_2H	HNCO	C_2H_5CN
		300 K		
G31	1.47 (0.61)×10^{18}	5.00 (0.46)×10^{16}	3.69 (0.39)×10^{16}	1.56 (0.42)×10^{16}
G29	...	1.61 (0.40)×10^{16}	1.80 (0.25)×10^{16}	2.25 (0.65)×10^{15}
G19	2.87 (0.60)×10^{17}	1.28 (0.41)×10^{16}	2.02 (0.22)×10^{16}	4.69 (0.36)×10^{15}
G24A1	2.90 (0.73)×10^{17}	...	1.43 (0.51)×10^{16}	5.26 (0.39)×10^{15}
G24A2	7.27 (0.44)×10^{17}	1.60 (0.71)×10^{16}	1.75 (0.43)×10^{16}	6.38 (0.43)×10^{15}
Object	CH_3CN[a]	$CH_2(OH)CHO$	$HCOOCH_3$	
G31	8×10^{16} (164 K)	1×10^{17}†† (300 K)	6.06 (0.03)×10^{17}††† (223 K)	
G29	1×10^{16} (158 K)	5.14 (0.66)×10^{15} (300 K)	1.62 (0.32)×10^{16} (300 K)	
G19	2×10^{16} (244 K)	4.59 (0.62)×10^{15} (300 K)	...	
G24A1	2×10^{16} (132 K)	3.95 (0.40)×10^{15} (300 K)	3.42 (0.48)×10^{16} (300 K)	
G24A2	2×10^{16} (132 K)	8.14 (0.49)×10^{15} (300 K)	3.80 (0.41)×10^{16} (300 K)	

[a] CH_3CN has been observed to be optically thick in all these objects so the column densities are those derived by (Beltrán et al. 2005, 2011) using observations of $CH_3{}^{13}CN$. Column density errors for this molecule are not given in these papers.
†† The column density of glycolaldehyde for G31 has been obtained by Beltrán et al. (2009) using the rotation diagram method, assuming a kinetic temperature of 300 K.
††† The column density for this object was determined using the rotation diagram method assuming a source size of 3.″5, see Section 3.1.

Table 6.28: Rotation temperatures derived for C_2H_5CN, HNCO, $HCOOCH_3$, CH_3COCH_3, CH_3NC, CH_3OH, and C_2H_3CN in IRAS 17233–3606.

Molecule	Rotation Temperature (K)
C_2H_5CN	44±5
HNCO	90±4
$HCOOCH_3$	179±25
CH_3COCH_3	199±6
CH_3NC	74±27
CH_3OH	163±9
C_2H_3CN	194±17

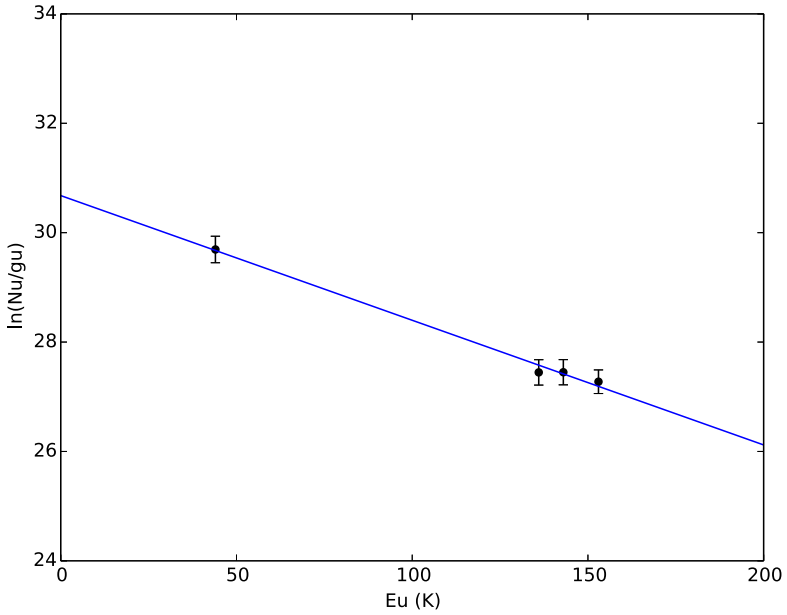

Figure 6.14: Rotation diagram for four transitions of C_2H_5CN detected in these observations.

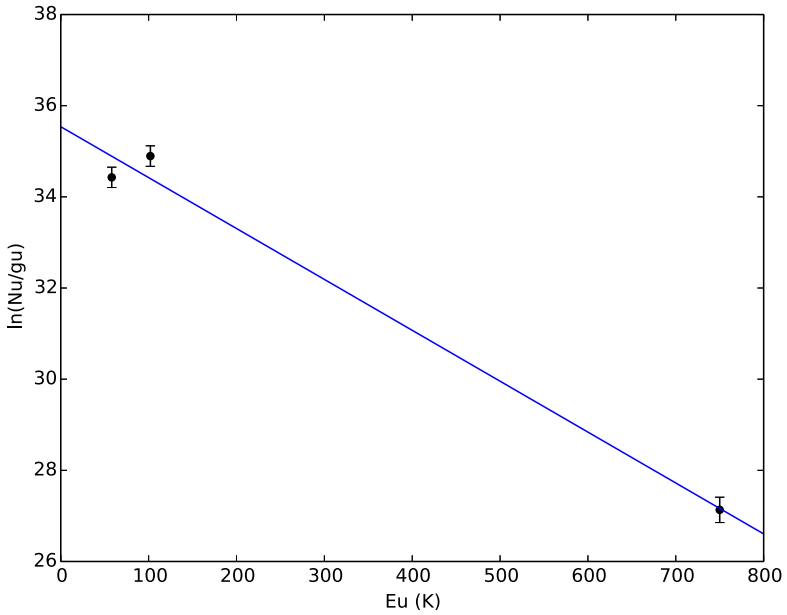

Figure 6.15: Rotation diagram for three transitions of HNCO detected in these observations. We omit the 10(3, 8, 11) – 9(3, 7, 10), 10(2, 9, 10) – 9(2, 8, 10) and 10(2, 8, 9) – 9(2, 7, 9) transitions from the diagram due to blending issues.

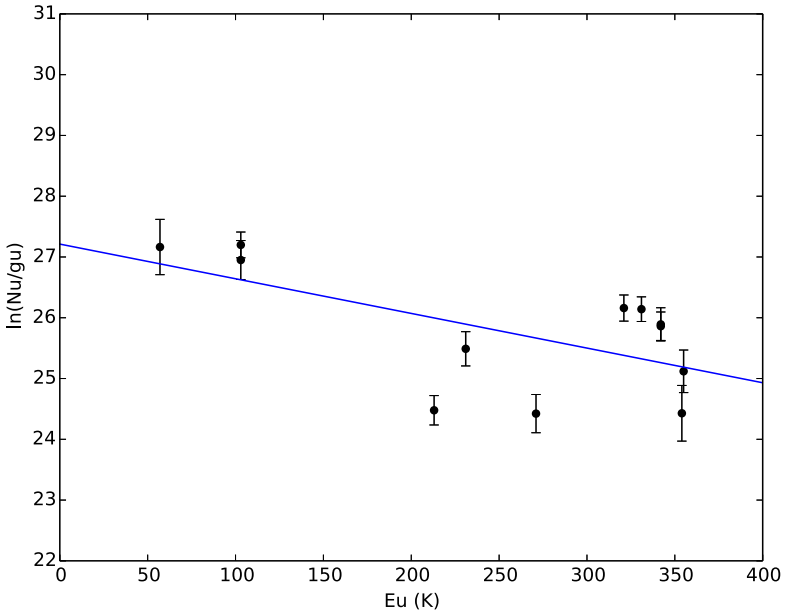

Figure 6.16: Rotation diagram for twelve transitions of $HCOOCH_3$ detected in these observations. We exclude the 18(14, 4, 0) – 17(14, 3, 0), 18(14, 5, 1) – 17(14, 4, 1) and 18(8, 11, 4) – 17(8, 10, 4) transitions from the diagram due to blending issues.

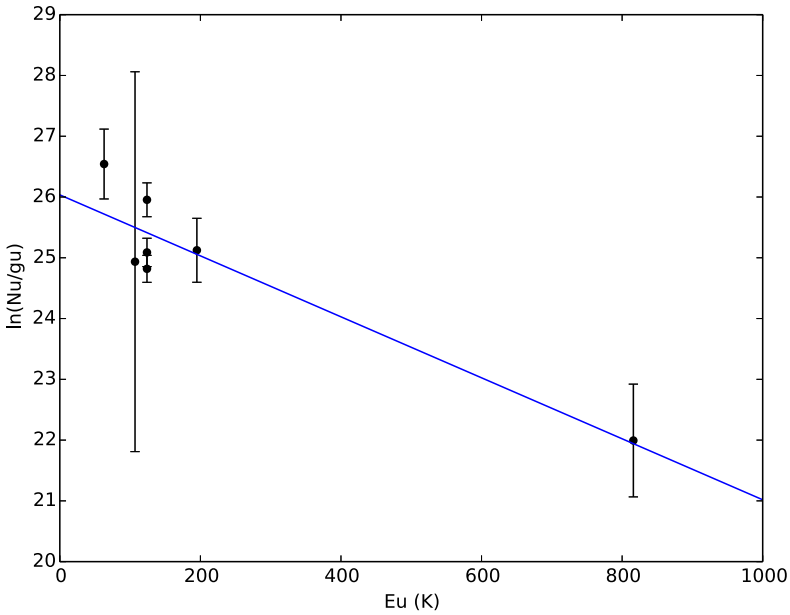

Figure 6.17: Rotation diagram for seven transitions of CH_3COCH_3 detected in these observations.

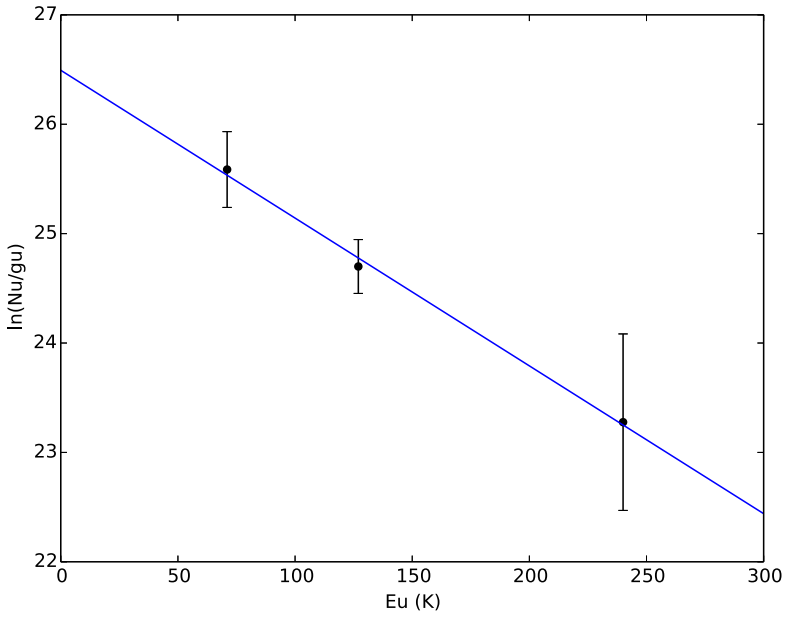

Figure 6.18: Rotation diagram for three transitions of CH_3NC detected in these observations.

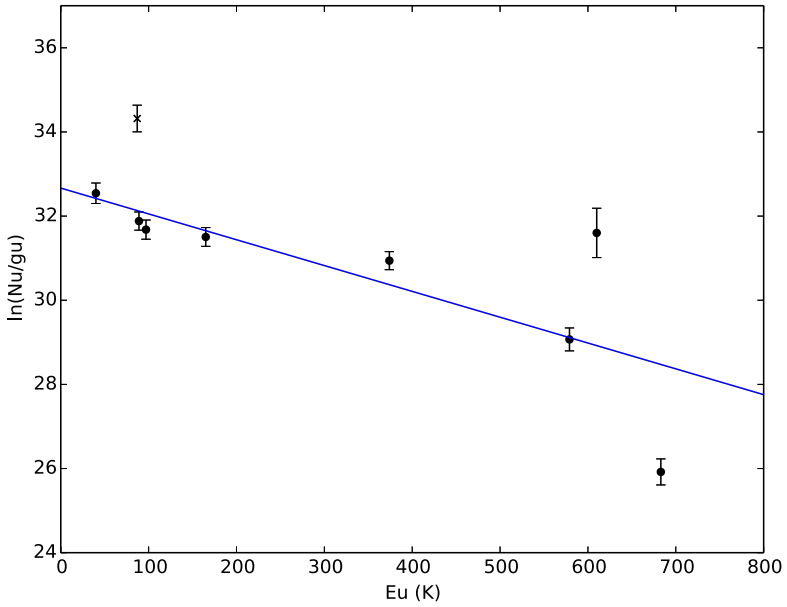

Figure 6.19: Rotation diagram for the eight transitions of CH_3OH and one transition of $^{13}CH_3OH$ detected in these observations.

Table 6.29: A comparison table between column densities (CD) and excitation temperatures derived through spectral modelling, and through the rotation diagram (RD) method at specific temperatures, for the molecules detected in Section 6.2.

Hot core	T_{ex} (K)	Spectral modelling CD (cm^{-2})	RD method CD
DC_3N	300	1.50×10^{14}	4.37×10^{13}
C_2H_5CN	300	1.30×10^{17}	4.40×10^{16}
HNCO	200	4.50×10^{16}	3.45×10^{17}
$H_2{}^{13}CO$	300	2.90×10^{16}	6.60×10^{17}
HC_3N	200	5.60×10^{16}	5.62×10^{14}
$HCOOCH_3$	179	1.00×10^{17}	5.86×10^{16}
CH_3COCH_3	100	4.20×10^{16}	1.70×10^{18}
CH_3NC	200	1.45×10^{15}	3.65×10^{14}
CH_3OH	170	1.00×10^{18}	5.82×10^{17}
C_2H_3CN	200	3.00×10^{16}	4.24×10^{16}

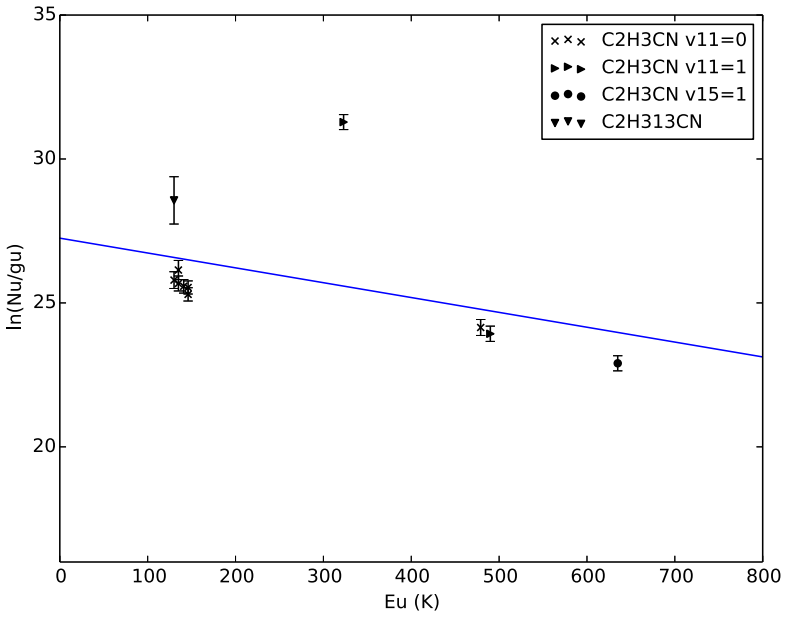

Figure 6.20: Rotation diagram for the v11=0, v11=1, and v15=1 transitions of C_2H_3CN detected in these observations.

6.4 Spectral modelling

There still remain many unidentified molecular transitions within our spectra, making an accurate spectral model difficult to produce. Despite this, we are able to determine column density estimates and rotation temperatures (Table 6.29) from the spectral modelling for each molecule we have discussed in the previous section. Normally, we would interpret the correct column density for a molecule as lying in the range between that determined through spectral modelling, and that determined using the rotation diagram

method. However, the spectral modelling column densities are calculated using transitions that are contaminated with an unknown amount of blending. In the rotation diagrams, we excluded such transitions to calculate the column densities, despite then often having very few transitions to determine an excitation temperature and column density. Considering the large differences between these two column densities (sometimes as high as two orders of magnitude), we believe that the values determined through the rotation diagram method are more accurate. With spectral modelling we have been able to determine the extent of the blending we see in the observations, highlighting the need to identify all of the emission in the source.

6.5 Conclusions

These observations of IRAS 17233–3606 highlight the difficulty of spectral identification in such a complex source. This work has vastly increased the number of species detected in this object, however, there still remains many spectral features that have not been unidentified. In this work we report the first detection of DC_3N, and $H_2{}^{13}CO$, however, further detections are required to confirm their presence in this object. We also report the first detection of seven transitions of CH_3COCH_3 and the first detection of five transitions of CH_3NC. We also detect new transitions of $HCOOCH_3$, C_2H_5CN, C_2H_3CN, HNCO, CH_3OH, and HC_3N. Despite the blending issues found in IRAS 17233–3606, column densities for the species identified in this work have been calculated using the rotation diagram method, to enable a quantitative comparison of the chemistry of IRAS 17233–3606 and other hot cores. Many more molecules are detected in IRAS 17233–3606 than in G31, making it the richest hot core discussed in this thesis. The differences observed in the column densities of the complex molecules between hot cores are indicative of the physical differences between the cores, whether these differences are due to evolutionary stage or mass, is however, unclear. Whilst column densities of C_2H_3CN are higher in G31 than in IRAS 17233–3606, suggesting that G31 is the older core, the G31 column densities are only derived from one transition making column densities less reliable, and this conclusion uncertain. It is possible that a ratio of complex molecule column densities, such as C_2H_3CN/C_2H_5CN, could be used as evolutionary indicator, this however, needs to be tested through chemical modelling and observations of a larger sample of hot cores.

Further work is needed to fully identify all of the emission in these observations of IRAS 17233–3606. It is likely that much of the emission is due to isotopologues of the species already identified in the spectra, which do not have full line catalogs.

Chapter 7

Conclusions

However beautiful the strategy, you should occasionally look at the results.

Winston Churchill

7.1 Summary of results

The aim of this thesis has been to explore how complex molecules can be used to trace the earliest stages of massive star formation. This has been undertaken by the study of several different hot cores through both observations, and chemical and spectral modelling.

In Chapter 2, interferometric data from the PdBI were analysed in the frequency range 220.20995 GHz to 220.75969 GHz towards six hot cores: G31, G29, G19, G10, G24A1, and G24A2. The aim was to identify seven lines that were unidentified by Beltrán et al. (2005) in G31, and look for their presence in the other five hot cores, as well as identify other complex molecules that were identified by Beltrán et al. (2005) in G31 and G24 but not in G29, G19 and G10. We have identified three new transitions of methyl formate ($HCOOCH_3$) in G31, two of which are vibrationally excited lines. We postulate that we have identified the $20_{2,18} - 19_{3,17}$ transition of glycolaldehyde in two more hot cores bringing the total number of detections in high mass star forming regions, outside the Galactic Centre, to five hot cores. We have mapped the spatial scale of methyl formate and glycolaldehyde,

and compare this to the spatial scale of CH_3CN. Comparatively methyl formate traces a region slightly more compact than that of methyl cyanide but glycolaldehyde emission still remains the most compact to date. At this stage we can not conclude whether the fact that methyl formate is more extended than glycolaldehyde is a question of excitation or chemistry. We do find, however, that in G29 methyl formate and glycolaldehyde are tracing a an emission region of 0.05 pc which is comparable to the compact emission of glycolaldehyde in G31 (0.08 pc). In G24 methyl formate and glycolaldehyde both trace a region comparable in size to the region traced by methyl formate in G31. We have also identified transitions of HNCO, C_2H_5CN, C_2H_3CN, and DCO_2H in G29, G19, G24A1, and G24A2, which were identified in G31 by Beltrán et al. (2005).

In Chapter 3, we performed a rotation diagram analysis of the methyl formate emission in G31 which yielded a column density of 6.06×10^{17} cm^{-2}. This is at least two orders of magnitude larger than the column densities in the other hot cores in our sample. We fit a single–temperature component of $\sim$223 K (using a source size of $3''.5$) to methyl formate emission in G31, however, the rotation diagram is very scattered, indicating non-LTE excitation or optically thick emission. Additionally, this may be due to multiple–temperature components being present in the data. The compact spatial extent of the vibrationally–excited transitions detected in G31 does indicate that it traces the dense, and hot parts of hot cores. In this chapter we also spectrally model the $20_{2,18}-19_{3,17}$ transition of glycolaldehyde to explore the possible contamination of this transition with the $46_{20,26}-46_{19,27}$ EE and $11_{11,1,1}-10_{10,0,1}$AE transitions of acetone. We find that any contribution of acetone emission to the line seen at 220.466 GHz is not significant. More observations are needed to confirm the presence of glycolaldehyde in G29, G19, G24A1, and G24A2. The other complex molecule detections in our sample highlight chemical homogeneity among G29, G19, G24A1 and G24A2, not only in terms of presence or absence of certain transitions but also when comparing column densities. G31 is the most chemically rich object in the sample studied here, and the significantly different column densities we find in this core, and the variety of transitions seen may suggest that it represents a different evolutionary stage to the other hot cores in our sample, or it may surround a star with a higher mass.

In Chapter 4, we have undertaken a comparison between observations and a chemical model, UCL_CHEM, to interpret the molecular inventory of the six cores and qualita-

tively characterise each core and its evolutionary stage. We note that of the species we are modelling, only methyl formate and methyl cyanide have been extensively studied in the laboratory (Modica & Palumbo 2010; Bennett & Kaiser 2007; Khlifi et al. 1996; Defrees et al. 1985; Huntress & Mitchell 1979). The other complex molecules are little–known and it is very likely that our models are missing routes of formation and destruction for these species. The uncertainties related to the size of the emission region and temperatures, together with the incompleteness of the chemical networks for COMs makes a more quantitative comparison with chemical modelling inappropriate. However, a qualitative comparison between our modelling and observations seem to consistently yield a higher density for G31 than the other objects in our sample, a result consistent with the fact that most lines are indeed the brightest in G31. We can also safely conclude that our sample only contains evolved hot cores, with an age of at least 20,000 years. We are unable to constrain the mass of each core; this information would have led to better constraints for the ages.

In Chapter 5, we followed on from the work in Chapters 2 – 4 by investigating the abundance ratio of acetic acid, glycolaldehyde, and methyl formate, in the same sample of hot cores. To do this we used the JCMT to detect new transitions of glycolaldehyde, thereby confirming its presence in G29, G19, and G24, and adding to the number of transitions that have been detected in G31. We also used these observations to detect new transitions of methyl formate in each of these cores, focusing on excited (v=1) transitions. As well as these detections, the observations were setup so they could simultaneously detect transitions of acetic acid for the first time in each of our hot cores. This work, highlighted the importance of single–dish telescopes in abundance studies of relatively strong molecules. It did, however, also highlight the difficulty of using these telescopes to detect weak molecules, such as acetic acid, and showed that it is essential that sidebands can be separated, owing to the very crowded spectra seen in star forming regions, in order to detect a large number of transitions. We were able to detect nine new transitions of methyl formate, including four excited (v=1) transitions, four new transitions of glycolaldehyde, and two new transitions of acetic acid.

Despite the new transitions of methyl formate that were detected, we were unable to chacterise the methyl formate emission further. A larger number of transitions are needed, with a focus on isotopologues of the transition already detected, in order to

determine optical depths. We also need to detect more transitions of acetic acid, to confirm its presence in our sample of hot cores, and derive more accurate column densities and rotation temperatures.

Our glycolaldehyde detections allowed us, for the first time, to determine rotation temperatures for G29, G19, and G24, which indicate that glycolaldehyde traces a hotter component than that traced by methyl formate. Unfortunately, the rotation temperature derived for G31 gave us a negative temperature, indicating that we either need to detect more transitions at a larger range of upper energy levels, or that glycolaldehyde emission is optically thick in these objects.

We determine the abundance ratio of acetic acid, glycolaldehyde, and methyl formate for the first time in several hot cores outside the Galactic Centre. The ratio determined in our hot core sample is similar in all cores except in G31, where a single column density could not be derived for glycolaldehyde, due to a lack of a rotation temperature. The abundace ratio is similar in all cores except G31, which suggests that G31 is physically different from the other cores. We found methyl formate to be the most abundant molecule in G31. Methyl formate is also found to be the most abundant molecule in the ratios derived in the Galactic Centre by Hollis et al. (2001) and Requena-Torres et al. (2006), however methyl formate is relatively more abundant in the Galactic Centre than in our hot core sample. These differences may represent a difference in the formation paths for these isomers in the Galactic Centre. In this work, we postulate that the abundance ratio of acetic acid, glycolaldehyde, and methyl formate could be used as a indicator of the age of a hot core, owing to the slow isomerization towards the most stable isomer (acetic acid), as has been suggested by some authors (Puletti et al. 2010; Lattelais et al. 2010). Applying this to our sample of hot cores would mean that G19 is the oldest hot core, followed by G29 and G24, and G31 is the youngest core.

In Chapter 6, we used the observations by Leurini et al. (2011) of the hot core in the star forming region IRAS 17233–3606, to investigate the chemical complexity of the object. Within the data, there were a large number of unidentified spectral feature. Through a combination of spectral modelling and line identification methods, we identify several of these spectral features, and identify some species for the first time in the object. We reported the first detection of DC_3N, and $H_2{}^{13}CO$, however further detections are required to confirm their presence in this object. We also reported the first detection of seven

transitions of CH_3COCH_3 and the first detection of five transitions of CH_3NC. We also detected new transitions of $HCOOCH_3$, C_2H_5CN, C_2H_3CN, HNCO, CH_3OH, and HC_3N. Despite the severe blending of many transitions, we were able to calculate column densities for these objects and compare them to the column densities for these species that had also been detected in G31, G29, G19, and G24. We also derived rotation temperatures through the rotation diagram method, and found that CH_3COCH_3 and C_2H_3CN trace the hottest components (199 K and 194 K respectively). Despite this work, there still remain several emission feature that were not identified, probably due to transitions of isopologues of many of the species we did identify, whose transitions are not present within our spectral line catalogues.

7.2 Overall conclusions

In Chapter 1, we stated the following key questions we wished to answer with this thesis:

- What are the best chemical tracers of the hottest, densest regions close to where the star is forming?

- Can molecules be used to trace the final mass of the star in a star forming region?

- What are the best tracers of the evolution of massive star formation?

- How does the chemistry of the local Galactic environment differ from that of Galactic Centre chemistry?

Through both observational and modelling studies of several hot cores we have found that complex molecules can be excellent tracers of the dense, hot regions close to where the star is forming. In particular, we found that to date, glycolaldehyde traces the most compact region in a hot core outside the Galactic Centre. We also found that its isomer, methyl formate, can trace a similarly compact region in some hot cores, and may offer the possibility of tracing multiple temperature components. This raises the question as to

what spatial extent does acetic acid, the third isomer in this trio, trace, as there have been no high spatial resolution observations of this molecule, in hot cores outside the Galactic Centre. Our studies on the abundance ratio of acetic acid, glycolaldehyde, and methyl formate also raise the possibility of determining the age of a hot core from this ratio alone. This work also suggests that the formation routes may be significantly affected by the different conditions found in the Galactic Centre, although without a larger sample of objects, this is difficult to definitively conclude. What is clear from this work, is that it is important to detect numerous transitions of a molecule, in order to derive accurate column densities and rotation temperatures. This is also important to confine the spectral models of hot core observations.

Our chemical modelling has shown that it is possible to constrain the age of hot cores, however, determining the exact age of a hot core compared to others that display similar evolved complex chemistry is difficult. The uncertainties in the chemical formation and destruction pathways for complex molecules mean that we cannot not use chemical modelling at this stage, to constrain the mass of hot cores.

7.3 Future Work

In this thesis we have detected several new molecules, but have not always been able to detect enough transitions to determine accurate column densities or rotation temperatures. Further observations are therefore needed, to probe the chemical and physical conditions in hot cores. In particular, higher–resolution observations are needed to probe the region traced by excited (v=1) methyl formate in G31, G29, G19, and G24. We propose that observations with ALMA of excited methyl formate transitions will enable the densest, hottest regions closest to where the star is forming to be traced. ALMA offers an enhanced spatial resolution compared to the PdBI, which our previous observations were performed with (see Chapter 2). The highest spatial resolution of the PdBI observations limited the spatial scale which we could explore to $\sim$2 pc. With ALMA observations, we would be able to explore scales as small as 0.007 pc for the most distant hot core in our sample (G31), allowing us to probe the potentially new component traced by vibrational excited states of methyl formate. These observations would also detect a wealth of complex molecules, such as acetone, glycolaldehyde, and acetic acid, which could be extensively mapped with

ALMA, providing further insight to the spatial variations of the chemistry in hot cores.

We can also further our work on acetic acid, with lower–resolution studies of G31, G29, G19, and G24. It is essential that further transitions of acetic acid are detected in these cores, to confirm its presence in several of them, and ensure accurate column densities are used to calculate the abundance ratio between acetic acid, glycolaldehyde, and methyl formate. This ratio must also be calculated in many more hot cores both in and outside the Galactic Centre, to determine whether it can be used as an evolutionary tracer of hot cores. These studies would be best achieved with an interferometer, such as the PdBI, which is less competitive than ALMA, whilst offering a higher spatial resolution than our JCMT observations.

In order to further the work on IRAS 17266–3606, a more detailed spectral model is needed to determine the identities of the remaining unidentified emission in the spectra. This will require the addition of more line catalogues to the spectral model, particular those containing isotopologues of common hot core molecules that are not currently in the JPL or CDMS catalogues used by CASSIS. Further to this, a comprehensive chemical modelling must be performed for the object, to really understand if the complex molecules that have been detected can be used as tracers of mass and age for this hot core.

Understanding the earliest stages of massive star formation with the observation of molecules provides many challenges that must be overcome. A large scale picture of massive star formation across the Galaxy, can only be achieved by taking a molecular inventory of all Galactic hot cores. This will catalogue the chemical and physical differences in hot cores, and provide a large enough sample to determine the best tracers of evolution, and mass in hot cores. This work will produce large quantities of spectral data, making the manual identification of molecular transitions a very time consuming process. It is therefore essential that more automated processes to identify spectral lines, and determine large scale patterns in the observations, are found. This techniques will need to be able to deal with the problems line contamination and line confusion often seen in the spectra of star forming regions.

In addition to this, the development of more advanced chemical modelling codes is

needed to analyse the observational results. These codes will combine chemical codes, with hydrodynamical simulations, to produce a complete physical and chemical model of massive star formation. The chemical networks used by these codes will need to contain a larger number of formation and destruction routes for the species identified. To achieve this a greater number of molecular laboratory studies of complex molecules will also be needed.

Appendix A

Appendix A

Here we present a derivation of the relation between the total column density, N_{tot}, and the integrated line intensity, W, which is determined from observations. We use the same notations as in Goldsmith & Langer (1999).

The antenna temperature T_a produced at a frequency ν by a source with brightness distribution $B_\nu(\theta, \phi)$ is given by:

$$T_a = (A_e/2k) \int_{4\pi} B_\nu(\theta, \phi) P_n(\theta, \phi) d\Omega \tag{A.1}$$

where $P_n(\theta, \phi)d\Omega$ is the normalised power pattern of the antenna, k is the boltzman constant, and A_e is the effective area.
For a source of uniform brightness:

$$T_a = (A_e/2k)(\delta\Omega_a) \left(\frac{\delta\Omega_s}{\delta\Omega_a} \right) B_\nu, \tag{A.2}$$

where Ω_a is the antenna solid angle, and Ω_s is the source solid angle.
The beam dilution factor is determined by:

$$\left(\frac{\delta\Omega_s}{\delta\Omega_a} \right) B_\nu \tag{A.3}$$

Using the antenna theorem Kraus et al. (1986)

$$A_e \delta\Omega_a = \lambda^2 \tag{A.4}$$

Using this, equation A.2 becomes

$$T_a = (\lambda^2/2k) \left(\frac{\delta\Omega_s}{\delta\Omega_a} \right) B_\nu \tag{A.5}$$

The brightness produced by a source at brightness temperature T with optical depth τ is

$$B_\nu = \frac{h\nu/k}{e^{h\nu/kT} - 1}(1 - e^{-\tau}) \tag{A.6}$$

The optical depth is determined by:

$$\tau = \frac{h}{\delta v} N_u B_{ul} (e^{h\nu/kT} - 1) \tag{A.7}$$

where N_u is the column density of the upper state, B_{ul} is the Einstein B-coefficient for the transition, and δv is the FWHM in units of velocity. Combining these equations we get:

$$T_a = \frac{hc^3 N_u A_{ul}}{8\pi k \nu^2 \delta v} \left(\frac{\delta\Omega_s}{\delta\Omega_a} \right) \left(\frac{1 - e^{-\tau}}{\tau} \right) \tag{A.8}$$

We want to be able to express the column density as a function of observed quantities such as frequency and the integrated line intensity: We can rewrite equation A.8 in terms of N_u.

$$N_u = \frac{8\pi k \nu^2 \int T_a dv}{hc^3 A_{ul}} \left(\frac{\delta\Omega_a}{\delta\Omega_s} \right) \left(\frac{\tau}{1 - e^{-\tau}} \right) \tag{A.9}$$

If the source fills the beam, and the emission is optically thin we get the equation for the relation for calculating the column density in the upper energy level from observational parameters:

$$N_u^{thin} = \frac{8\pi k \nu^2 \int T dv}{hc^3 A_{ul}} \tag{A.10}$$

This can be written in terms of g_u, the statistical weight of the level u:

$$N_u/g_u = \frac{8\pi k\nu^2 \int T dv}{hc^3 A g_u} \tag{A.11}$$

Bibliography

Andernach, H., 1999, in M. R. Kidger, I. Perez-Fournon & F. Sanchez (eds.), *Internet Resources for Professional Astronomy*, pp. 67–130

Argon, A. L., Reid, M. J. & Menten, K. M., 2000, *Astrophysical Journal Supplement*, **129**, 159

Awad, Z., Viti, S., Bayet, E. & Caselli, P., 2014, *Monthly Notices of the RAS*, **443**, 275

Beltrán, M. T., Cesaroni, R., Codella, C., Testi, L., Furuya, R. S. & Olmi, L., 2006, *Nature*, **443**, 427

Beltrán, M. T., Cesaroni, R., Moscadelli, L. & Codella, C., 2007, *Astronomy and Astrophysics*, **471**, L13

Beltrán, M. T., Cesaroni, R., Neri, R. & Codella, C., 2011, *Astronomy and Astrophysics*, **525**, A151

Beltrán, M. T., Cesaroni, R., Neri, R., Codella, C., Furuya, R. S., Testi, L. & Olmi, L., 2004, *Astrophysical Journal, Letters*, **601**, L187

Beltrán, M. T., Cesaroni, R., Neri, R., Codella, C., Furuya, R. S., Testi, L. & Olmi, L., 2005, *Astronomy and Astrophysics*, **435**, 901

Beltrán, M. T., Codella, C., Viti, S., Neri, R. & Cesaroni, R., 2009, *Astrophysical Journal Letters*, **690**, L93

Beltràn, M. T., Codella, C., Viti, S., Neri, R. & Cesaroni, R., 2010, *Highlights of Astronomy*, **15**, 701

Beltrán, M. T., Estalella, R., Anglada, G., Rodríguez, L. F. & Torrelles, J. M., 2001, *Astronomical Journal*, **121**, 1556

Benjamin, R. A., 2003, in M. Bailes, D. J. Nice & S. E. Thorsett (eds.), *Radio Pulsars*, volume 302 of *Astronomical Society of the Pacific Conference Series*, p. 271

Bennett, C. J. & Kaiser, R. I., 2007, *Astrophysical Journal*, **661**, 899

Bernasconi, P. A. & Maeder, A., 1996, *Astronomy and Astrophysics*, **307**, 829

Beuther, H., Zhang, Q., Bergin, E. A. & Sridharan, T. K., 2009, *Astronomical Journal*, **137**, 406

Beuther, H., Zhang, Q., Bergin, E. A., Sridharan, T. K., Hunter, T. R. & Leurini, S., 2007, *Astronomy and Astrophysics*, **468**, 1045

Biham, O., Furman, I., Pirronello, V. & Vidali, G., 2001, *Astrophysical Journal*, **553**, 595

Blum, R. D., Damineli, A. & Conti, P. S., 2001, *Astronomical Journal*, **121**, 3149

Bohlin, R. C., Savage, B. D. & Drake, J. F., 1978, *Astrophysical Journal*, **224**, 132

Bonnell, I. A., 2007, in N. St.-Louis & A. F. J. Moffat (eds.), *Massive Stars in Interactive Binaries*, volume 367 of *Astronomical Society of the Pacific Conference Series*, p. 303

Bonnell, I. A. & Bate, M. R., 2002, *Monthly Notices of the RAS*, **336**, 659

Bottinelli, S., Ceccarelli, C., Lefloch, B., Williams, J. P., Castets, A., Caux, E., Cazaux, S., Maret, S., Parise, B. & Tielens, A. G. G. M., 2004, *Astrophysical Journal*, **615**, 354

Buckle, J. V. & Fuller, G. A., 2003, *Astronomy and Astrophysics*, **399**, 567

Burke, D., Brown, W. A., Viti, S., Woods, P. M. & Slater, B., 2012, in *American Astronomical Society Meeting Abstracts*, volume 220 of *American Astronomical Society Meeting Abstracts*, p. 210.03

Calcutt, H., Viti, S., Codella, C., Beltrn, M. T., Fontani, F. & Woods, P. M., 2014, **443**(4), 3157

Carey, S. J., Noriega-Crespo, A., Mizuno, D. R., Shenoy, S., Paladini, R., Kraemer, K. E., Price, S. D., Flagey, N., Ryan, E., Ingalls, J. G., Kuchar, T. A., Pinheiro Gonçalves, D., Indebetouw, R., Billot, N., Marleau, F. R., Padgett, D. L., Rebull, L. M., Bressert, E., Ali, B., Molinari, S., Martin, P. G., Berriman, G. B., Boulanger, F., Latter, W. B., Miville-Deschenes, M. A., Shipman, R. & Testi, L., 2009, *Publications of the ASP*, **121**, 76

Cazaux, S., Tielens, A. G. G. M., Ceccarelli, C., Castets, A., Wakelam, V., Caux, E., Parise, B. & Teyssier, D., 2003, *Astrophysical Journal, Letters*, **593**, L51

Cesaroni, R., 2002, *Highlights of Astronomy*, **12**, 156

Cesaroni, R., Beltrán, M. T., Zhang, Q., Beuther, H. & Fallscheer, C., 2011, *Astronomy and Astrophysics*, **533**, A73

Cesaroni, R., Churchwell, E., Hofner, P., Walmsley, C. M. & Kurtz, S., 1994, *Astronomy and Astrophysics*, **288**, 903

Cesaroni, R., Codella, C., Furuya, R. S. & Testi, L., 2003, *Astronomy and Astrophysics*, **401**, 227

Cesaroni, R., Hofner, P., Araya, E. & Kurtz, S., 2010, *Astronomy and Astrophysics*, **509**, A50

Cesaroni, R., Hofner, P., Walmsley, C. M. & Churchwell, E., 1998, *Astronomy and Astrophysics*, **331**, 709

Cesaroni, R., Walmsley, C. M., Koempe, C. & Churchwell, E., 1991, *Astronomy and Astrophysics*, **252**, 278

Charnley, S. B., 1998, *Monthly Notices of the RAS*, **298**, L25

Charnley, S. B., 2001, *Astrophysical Journal Letters*, **562**, L99

Chengalur, J. N., 2003, *Single Dish Radio Telescopes*
URL: *http://www.ncra.tifr.res.in/ncra/gmrt/gmrt-users/observing-help-for-gmrt-users/low-frequency-radio-astronomy/ch3.pdf*

Churchwell, E., Wolfire, M. G. & Wood, D. O. S., 1990, *Astrophysical Journal*, **354**, 247

Codella, C., Beltrán, M. T., Cesaroni, R., Moscadelli, L., Neri, R., Vasta, M. & Zhang, Q., 2013, *Astronomy and Astrophysics*, **550**, A81

Codella, C., Testi, L. & Cesaroni, R., 1997, *Astronomy and Astrophysics*, **325**, 282

Collings, M. P., Anderson, M. A., Chen, R., Dever, J. W., Viti, S., Williams, D. A. & McCoustra, M. R. S., 2004, *Monthly Notices of the RAS*, **354**, 1133

Collings, M. P., Dever, J. W., Fraser, H. J. & McCoustra, M. R. S., 2003*a*, *Astrophysics and Space Science*, **285**, 633

Collings, M. P., Dever, J. W., Fraser, H. J., McCoustra, M. R. S. & Williams, D. A., 2003*b*, *Astrophysical Journal*, **583**, 1058

Cravens, T. E. & Dalgarno, A., 1978, *Astrophysical Journal*, **219**, 750

Creighan, S. C., Perry, J. S. A. & Price, S. D., 2006, *The Journal of Chemical Physics*, **124**(11), 1
URL: *http://scitation.aip.org/content/aip/journal/jcp/124/11/10.1063/1.2174878*

Cyganowski, C. J., Brogan, C. L., Hunter, T. R., Graninger, D., Öberg, K. I., Vasyunin, A., Zhang, Q., Friesen, R. & Schnee, S., 2014, *Astrophysical Journal Letters*, **796**, L2

Dalgarno, A. & van der Loo, M. P. J., 2006, *Astrophysical Journal Letters*, **646**, L91

Defrees, D. J., McLean, A. D. & Herbst, E., 1985, *Astrophysical Journal*, **293**, 236

Doty, S. D., van Dishoeck, E. F., van der Tak, F. F. S. & Boonman, A. M. S., 2002, *Astronomy and Astrophysics*, **389**, 446

Duley, W. W. & Williams, D. A., 1993, *Monthly Notices of the RAS*, **260**, 37

Esplugues, G. B., Cernicharo, J., Viti, S., Goicoechea, J. R., Tercero, B., Marcelino, N., Palau, A., Bell, T. A., Bergin, E. A., Crockett, N. R. & Wang, S., 2013, *Astronomy and Astrophysics*, **559**, A51

Faúndez, S., Bronfman, L., Garay, G., Chini, R., Nyman, L.-Å. & May, J., 2004, *Astronomy and Astrophysics*, **426**, 97

Favre, C., Despois, D., Brouillet, N., Baudry, A., Combes, F., Guélin, M., Wootten, A. & Wlodarczak, G., 2011, *Astronomy and Astrophysics*, **532**, A32

Fish, V. L., Reid, M. J. & Menten, K. M., 2005, *Astrophysical Journal*, **623**, 269

Fontani, F., Pascucci, I., Caselli, P., Wyrowski, F., Cesaroni, R. & Walmsley, C. M., 2007, *Astronomy and Astrophysics*, **470**, 639

Forster, J. R. & Caswell, J. L., 1989, *Astronomy and Astrophysics*, **213**, 339

Fortman, S. M., Medvedev, I. R., Neese, C. F. & De Lucia, F. C., 2010, *Astrophysical Journal*, **714**, 476

Fraser, H. J., Collings, M. P., McCoustra, M. R. S. & Williams, D. A., 2001, *Monthly Notices of the RAS*, **327**, 1165

Fuente, A., Cernicharo, J., Caselli, P., McCoey, C., Johnstone, D., Fich, M., van Kempen, T., Palau, A., Yıldız, U. A., Tercero, B. & López, A., 2014, *Astronomy and Astrophysics*, **568**, A65

Furuya, R. S., Cesaroni, R., Codella, C., Testi, L., Bachiller, R. & Tafalla, M., 2002, *Astronomy and Astrophysics*, **390**, L1

Furuya, R. S., Cesaroni, R. & Shinnaga, H., 2011, *Astronomy and Astrophysics*, **525**, A72

Furuya, R. S., Kitamura, Y., Wootten, A., Claussen, M. J. & Kawabe, R., 2005, *Astronomy and Astrophysics*, **438**, 571

Garay, G. & Lizano, S., 1999, *Publications of the ASP*, **111**, 1049

Garay, G., Moran, J. M., Rodriguez, L. F. & Reid, M. J., 1998, *Astrophysical Journal*, **492**, 635

Garay, G., Reid, M. J. & Moran, J. M., 1985, *Astrophysical Journal*, **289**, 681

Gaume, R. A. & Mutel, R. L., 1987, *Astrophysical Journal Supplement*, **65**, 193

Gibb, A. G., Wyrowski, F. & Mundy, L. G., 2004, *Astrophysical Journal*, **616**, 301

Gibb, E., Nummelin, A., Irvine, W. M., Whittet, D. C. B. & Bergman, P., 2000, *Astrophysical Journal*, **545**, 309

Goldsmith, P. F. & Langer, W. D., 1999, *Astrophysical Journal*, **517**, 209

Gredel, R., Lepp, S., Dalgarno, A. & Herbst, E., 1989, *Astrophysical Journal*, **347**, 289

Green, N. J. B., Toniazzo, T., Pilling, M. J., Ruffle, D. P., Bell, N. & Hartquist, T. W., 2001, *Astronomy and Astrophysics*, **375**, 1111

Halfen, D. T., Apponi, A. J., Woolf, N., Polt, R. & Ziurys, L. M., 2006, *Astrophysical Journal*, **639**, 237

Hasegawa, T. I., Herbst, E. & Leung, C. M., 1992, *Astrophysical Journal Supplement*, **82**, 167

Hatchell, J., Thompson, M. A., Millar, T. J. & MacDonald, G. H., 1998, *Astronomy and Astrophysics*, **338**, 713

Haykal, I., Motiyenko, R. A., Margules, L. & Huet, T. R., 2012, *VizieR Online Data Catalog*, **354**, 99096

Herbst, E. & Klemperer, W., 1973, *Astrophysical Journal*, **185**, 505

Herbst, E. & van Dishoeck, E. F., 2009, *Annual Review of Astron and Astrophys*, **47**, 427

Ho, P. T. P. & Haschick, A. D., 1986, *Astrophysical Journal*, **304**, 501

Hoffman, I. M., Goss, W. M., Palmer, P. & Richards, A. M. S., 2003, *Astrophysical Journal*, **598**, 1061

Hofner, P. & Churchwell, E., 1996, *Astronomy and Astrophysics, Supplement*, **120**, 283

Hollenbach, D. & Salpeter, E. E., 1970, *Journal of Chemical Physics*, **53**, 79

Hollenbach, D. & Salpeter, E. E., 1971, *Astrophysical Journal*, **163**, 155

Hollenbach, D. J., Werner, M. W. & Salpeter, E. E., 1971, *Astrophysical Journal*, **163**, 165

Hollis, J. M., Lovas, F. J. & Jewell, P. R., 2000, *Astrophysical Journal, Letters*, **540**, L107

Hollis, J. M., Vogel, S. N., Snyder, L. E., Jewell, P. R. & Lovas, F. J., 2001, *Astrophysical Journal Letters*, **554**, L81

Hughes, V. A. & MacLeod, G. C., 1993, *Astronomical Journal*, **105**, 1495

Huntress, Jr., W. T. & Mitchell, G. F., 1979, *Astrophysical Journal*, **231**, 456

Ikeda, M., Ohishi, M., Nummelin, A., Dickens, J. E., Bergman, P., Hjalmarson, Å. & Irvine, W. M., 2001, *Astrophysical Journal*, **560**, 792

Ilyushin, V., Kleiner, I. & Lovas, F. J., 2008, *Journal of Physical and Chemical Reference Data*, **37**(1)

Isokoski, K., Bottinelli, S. & van Dishoeck, E. F., 2013, *Astronomy and Astrophysics*, **554**, A100

Jørgensen, J. K., Favre, C., Bisschop, S. E., Bourke, T. L., van Dishoeck, E. F. & Schmalzl, M., 2012, *Astrophysical Journal, Letters*, **757**, L4

Keto, E., 2002, *Astrophysical Journal*, **568**, 754

Keto, E. & Wood, K., 2006, *Astrophysical Journal*, **637**, 850

Keto, E. R., Ho, P. T. P. & Haschick, A. D., 1988, *Astrophysical Journal*, **324**, 920

Keto, E. R., Ho, P. T. P. & Reid, M. J., 1987, *Astrophysical Journal Letters*, **323**, L117

Khlifi, M., Paillous, P., Bruston, P., Raulin, F. & Guillemin, J. C., 1996, *Icarus*, **124**, 318

Klaassen, P. D., Wilson, C. D., Keto, E. R. & Zhang, Q., 2009, *Astrophysical Journal*, **703**, 1308

Kolpak, M. A., Jackson, J. M., Bania, T. M., Clemens, D. P. & Dickey, J. M., 2003, *Astrophysical Journal*, **582**, 756

Kraus, J., Tiuri, M. & Räisänen, A., 1986, *Radio astronomy* (Cygnus-Quasar Books) **URL:** *http://books.google.co.uk/booksid=KtVFAQAAIAAJ*

Kraus, S., Hofmann, K.-H., Menten, K. M., Schertl, D., Weigelt, G., Wyrowski, F., Meilland, A., Perraut, K., Petrov, R., Robbe-Dubois, S., Schilke, P. & Testi, L., 2010, *Nature*, **466**, 339

Lattelais, M., Pauzat, F., Ellinger, Y. & Ceccarelli, C., 2009, *Astrophysical Journal Letters*, **696**, L133

Lattelais, M., Pauzat, F., Ellinger, Y. & Ceccarelli, C., 2010, *Astronomy and Astrophysics*, **519**, A30

Lehtinen, K., 1997, *Astronomy and Astrophysics*, **317**, L5

Leurini, S., Codella, C., Zapata, L., Beltrán, M. T., Schilke, P. & Cesaroni, R., 2011, *Astronomy and Astrophysics*, **530**, A12

Leurini, S., Codella, C., Zapata, L. A., Belloche, A., Stanke, T., Wyrowski, F., Schilke, P., Menten, K. M. & Güsten, R., 2009, *Astronomy and Astrophysics*, **507**, 1443

Leurini, S., Hieret, C., Thorwirth, S., Wyrowski, F., Schilke, P., Menten, K. M., Güsten, R. & Zapata, L., 2008, *Astronomy and Astrophysics*, **485**, 167

López-Sepulcre, A., Codella, C., Cesaroni, R., Marcelino, N. & Walmsley, C. M., 2009, *Astronomy and Astrophysics*, **499**, 811

Lovas, F. J., 2004, *Journal of Physical and Chemical Reference Data*, **33**(1)

Matthews, H. E., Leech, J. & Friberg, P., 2004, *JAC*

Maxia, C., Testi, L., Cesaroni, R. & Walmsley, C. M., 2001, *Astronomy and Astrophysics*, **371**, 287

McKee, C. F. & Tan, J. C., 2002, *Nature*, **416**, 59

McKee, C. F. & Tan, J. C., 2003, *Astrophysical Journal*, **585**, 850

Medvedev, I. R. & De Lucia, F. C., 2007, *Astrophysical Journal*, **656**, 621

Mehringer, D. M., Snyder, L. E., Miao, Y. & Lovas, F. J., 1997, *Astrophysical Journal Letters*, **480**, L71

Miettinen, O., Harju, J., Haikala, L. K. & Pomrén, C., 2006, *Astronomy and Astrophysics*, **460**, 721

Minier, V., Burton, M. G., Hill, T., Pestalozzi, M. R., Purcell, C. R., Garay, G., Walsh, A. J. & Longmore, S., 2005, *Astronomy and Astrophysics*, **429**, 945

Modica, P. & Palumbo, M. E., 2010, *Astronomy and Astrophysics*, **519**, A22

Molinari, S., Brand, J., Cesaroni, R. & Palla, F., 2000, *Astronomy and Astrophysics*, **355**, 617

Mookerjea, B., Casper, E., Mundy, L. G. & Looney, L. W., 2007, *Astrophysical Journal*, **659**, 447

Moscadelli, L., Goddi, C., Cesaroni, R., Beltrán, M. T. & Furuya, R. S., 2007, *Astronomy and Astrophysics*, **472**, 867

Müller, H. S. P., Schlöder, F., Stutzki, J. & Winnewisser, G., 2005, *Journal of Molecular Structure*, **742**, 215

Occhiogrosso, A., Viti, S., Modica, P. & Palumbo, M. E., 2011, *Monthly Notices of the RAS*, **418**, 1923

Ohishi, M., McGonagle, D., Irvine, W. M., Yamamoto, S. & Saito, S., 1994, *Astrophysical Journal, Letters*, **427**, L51

Olmi, L., Cesaroni, R., Hofner, P., Kurtz, S., Churchwell, E. & Walmsley, C. M., 2003, *Astronomy and Astrophysics*, **407**, 225

Palla, F. & Stahler, S. W., 1993, *Astrophysical Journal*, **418**, 414

Pickett, H. M., Poynter, R. L., Cohen, E. A., Delitsky, M. L., Pearson, J. C. & Müller, H. S. P., 1998, *Journal of Quantitiative Spectroscopy and Radiative Transfer*, **60**, 883

Pickles, J. B. & Williams, D. A., 1977, *Astrophysics and Space Science*, **52**, 443

Plume, R., Jaffe, D. T. & Evans, II, N. J., 1992, *Astrophysical Journal Supplement*, **78**, 505

Prasad, S. S. & Tarafdar, S. P., 1983, *Astrophysical Journal*, **267**, 603

Pratap, P., Megeath, S. T. & Bergin, E. A., 1999, *Astrophysical Journal*, **517**, 799

Puletti, F., Malloci, G., Mulas, G. & Cecchi-Pestellini, C., 2010, *Monthly Notices of the RAS*, **402**, 1667

Rawlings, J. M. C., Hartquist, T. W., Menten, K. M. & Williams, D. A., 1992, *Monthly Notices of the RAS*, **255**, 471

Remijan, A., Shiao, Y.-S., Friedel, D. N., Meier, D. S. & Snyder, L. E., 2004, *Astrophysical Journal*, **617**, 384

Remijan, A., Snyder, L. E., Friedel, D. N., Liu, S.-Y. & Shah, R. Y., 2003, *Astrophysical Journal*, **590**, 314

Remijan, A., Snyder, L. E., Liu, S.-Y., Mehringer, D. & Kuan, Y.-J., 2002, *Astrophysical Journal*, **576**, 264

Requena-Torres, M. A., Martín-Pintado, J., Martín, S. & Morris, M. R., 2008, *Astrophysical Journal*, **672**, 352

Requena-Torres, M. A., Martín-Pintado, J., Rodríguez-Franco, A., Martín, S., Rodríguez-Fernández, N. J. & de Vicente, P., 2006, *Astronomy and Astrophysics*, **455**, 971

Roberts, J. F., Rawlings, J. M. C., Viti, S. & Williams, D. A., 2007, *Monthly Notices of the RAS*, **382**, 733

Rosen, A. L., Krumholz, M. R. & Ramirez-Ruiz, E., 2012, *Astrophysical Journal*, **748**, 97

Ruffle, D. P. & Herbst, E., 2001, *Monthly Notices of the RAS*, **324**, 1054

Sakai, N., Sakai, T. & Yamamoto, S., 2007, *Astrophysical Journal*, **660**, 363

Shiao, Y.-S. J., Looney, L. W., Remijan, A. J., Snyder, L. E. & Friedel, D. N., 2010, *Astrophysical Journal*, **716**, 286

Shu, F. H., Adams, F. C. & Lizano, S., 1987, *Annual Review of Astron and Astrophys*, **25**, 23

Snyder, L. E., Lovas, F. J., Hollis, J. M., Friedel, D. N., Jewell, P. R., Remijan, A., Ilyushin, V. V., Alekseev, E. A. & Dyubko, S. F., 2005, *Astrophysical Journal*, **619**, 914

Sofia, U. J. & Meyer, D. M., 2001, *Astrophysical Journal Letters*, **554**, L221

Sollins, P. K. & Ho, P. T. P., 2005, *Astrophysical Journal*, **630**, 987

Stantcheva, T., Shematovich, V. I. & Herbst, E., 2002, *Astronomy and Astrophysics*, **391**, 1069

Tan, J. C., Beltrán, M. T., Caselli, P., Fontani, F., Fuente, A., Krumholz, M. R., McKee, C. F. & Stolte, A., 2014, *Protostars and Planets VI*, 149

Tanaka, K. E. I. & Nakamoto, T., 2010, *Astrophysical Journal*, **714**, 309

Tielens, A. G. G. M. & Hagen, W., 1982, *Astronomy and Astrophysics*, **114**, 245

Townes, C. H. & Schawlow, A. L., 1955, *Microwave Spectroscopy* (New York: McGraw-Hill)

Turner, B. E. & Apponi, A. J., 2001, *Astrophysical Journal, Letters*, **561**, L207

van Dishoeck, E. F. & Blake, G. A., 1998, *Annual Review of Astron and Astrophys*, **36**, 317

Vastel, C., 2014, *Formalism for the CASSIS software*
URL: *http://cassis.irap.omp.eu/docs/RadiativeTransfer.pdf*

Vig, S., Cesaroni, R., Testi, L., Beltrán, M. T. & Codella, C., 2008, *Astronomy and Astrophysics*, **488**, 605

Viti, S., Caselli, P., Hartquist, T. W. & Williams, D. A., 2001, *Astronomy and Astrophysics*, **370**, 1017

Viti, S., Collings, M. P., Dever, J. W., McCoustra, M. R. S. & Williams, D. A., 2004, *Monthly Notices of the RAS*, **354**, 1141

Viti, S. & Williams, D. A., 1999, *Monthly Notices of the RAS*, **305**, 755

Wakelam, V., Caselli, P., Ceccarelli, C., Herbst, E. & Castets, A., 2004, *Astronomy and Astrophysics*, **422**, 159

Wakelam, V., Cuppen, H. M. & Herbst, E., 2013, *ArXiv e-print:1309.7792*

Wakelam, V., Loison, J.-C., Herbst, E., Talbi, D., Quan, D. & Caralp, F., 2009, *Astronomy and Astrophysics*, **495**, 513

Walsh, A. J., Burton, M. G., Hyland, A. R. & Robinson, G., 1998, *Monthly Notices of the RAS*, **301**, 640

Wang, P., Li, Z.-Y., Abel, T. & Nakamura, F., 2010, *Astrophysical Journal*, **709**, 27

Watson, W. D., 1973, *Astrophysical Journal Letters*, **183**, L17

Watson, W. D. & Salpeter, E. E., 1972, *Astrophysical Journal*, **174**, 321

Williams, D. & Viti, S., 2013, *Observational Molecular Astronomy: Exploring the Universe Using Molecular Line Emissions*, Cambridge Observing Handbooks for Research Astronomers (Cambridge University Press)

Wilson, T. L. & Rood, R., 1994, *Annual Review of Astron and Astrophys*, **32**, 191

Winters, J. & Neri, R., 2011, *An Introduction to the IRAM Plateau de Bure Interferometer*
URL: *https://www.iram.fr/IRAMFR/GILDAS/doc/html/pdbi-intro-html/pdbi-intro.html*

Wirström, E. S., Bergman, P., Hjalmarson, Å. & Nummelin, A., 2007, *Astronomy and Astrophysics*, **473**, 177

Wolfire, M. G. & Cassinelli, J. P., 1987, *Astrophysical Journal*, **319**, 850

Wood, D. O. S. & Churchwell, E., 1989, *Astrophysical Journal Supplement*, **69**, 831

Woodall, J., Agúndez, M., Markwick-Kemper, A. J. & Millar, T. J., 2007, *Astronomy and Astrophysics*, **466**, 1197

Woods, P. M., Kelly, G., Viti, S., Slater, B., Brown, W. A., Puletti, F., Burke, D. J. & Raza, Z., 2012, *Astrophysical Journal*, **750**, 19

Wright, A., 2004, *Single-dish Radio Astronomy*
URL: *http://www.allrite.net/science/docs/SingleDishTelescopes.pdf*

Wu, Y., Qin, S.-L., Guan, X., Xue, R., Ren, Z., Liu, T., Huang, M. & Chen, S., 2009, *Astrophysical Journal Letters*, **697**, L116

Xu, L.-H., Fisher, J., Lees, R. M., Shi, H. Y., Hougen, J. T., Pearson, J. C., Drouin, B. J., Blake, G. A. & Braakman, R., 2008, *Journal of Molecular Spectroscopy*, **251**, 305

Zapata, L. A., Leurini, S., Menten, K. M., Schilke, P., Rolffs, R. & Hieret, C., 2008, *Astronomical Journal*, **136**, 1455

Zhu, L.-b., Yang, J. & Wang, M., 2007, *Chinese Astronomy and Astrophysics*, **31**, 387

"The time is gone, the song is over,
Thought I'd something more to say."

Time, Pink Floyd